Doctoral Dissertation
博士論文

Torsion Pendulum with Interferometric Readout for Low-Frequency Gravity Gradient Observation

(低周波重力勾配観測のための高感度ねじれ振り子の開発)

A Dissertation Submitted for the Degree of Doctor of Philosophy
December 2024
令和 6 年 12 月 博士 (理学) 申請

Department of Physics, Graduate School of Science,
The University of Tokyo
東京大学 大学院理学系研究科 物理学専攻

Yuka Oshima
大島 由佳

Abstract

Gravity gradient fluctuations are important targets for precisely measuring the movement of masses. In particular, low-frequency gravity gradient fluctuations in the range of 0.1 Hz to 10 Hz can lead to significant scientific outcomes, such as detecting gravitational waves from intermediate-mass black hole binary mergers, direct observation of Newtonian noise caused by ground and atmospheric disturbances, and providing early earthquake warning by utilizing gravity gradients caused by fault ruptures.

Gravitational waves are ripples in spacetime that propagate through the universe at the speed of light. Recently, they have gained attention as an important observational target in astronomy. Since the first detection of gravitational waves by Advanced LIGO (Laser Interferometer Gravitational-Wave Observatory) in 2015, approximately 90 events of gravitational waves from compact binary mergers have been observed as of 2023. Current gravitational wave detectors are designed to achieve high sensitivity in the frequency band in 10 Hz–1 kHz. Extending the observation band to lower frequencies is expected to enable the detection of gravitational waves from intermediate-mass black hole binary mergers, contributing to the understanding of the formation of supermassive black holes.

Newtonian noise refers to fluctuations in the gravitational field caused by ground and atmospheric disturbances. It perturbs the test masses of gravitational wave detectors, making it fundamentally indistinguishable from gravitational wave signals. As a result, Newtonian noise is predicted to become a significant noise source for future third-generation ground-based gravitational wave detectors. The amplitude of Newtonian noise is theoretically expected to increase at lower frequencies. However, direct detection is necessary for modeling and establishing mitigation techniques.

Recently, gravity gradient observations for earthquake early warning have been proposed. Compared to current methods that observe seismic waves, gravity-gradient-based earthquake early warning is expected to enable faster detection and more accurate estimation of earthquake magnitudes. For its realization, high-sensitivity detection of gravity gradients around 0.1 Hz, generated by fault ruptures during earthquakes, is required.

To observe these targets, a low-frequency gravity gradiometer called TOBA (Torsion-Bar Antenna) has been proposed. TOBA measures the rotational motion of torsion pendulums induced by gravity gradients. By using torsion pendulums with low resonant frequencies, TOBA can observe gravity gradients in the low-frequency band (0.1 Hz to 10 Hz), even on the ground, where the detector is bound by the strong gravitational field. The ultimate goal is a 10 m-scale detector called Final TOBA, with a target sensitivity

of 1×10^{-19} $/\sqrt{\text{Hz}}$ at 0.1 Hz. To achieve Final TOBA, a smaller prototype, Phase-III TOBA, with a 35 cm-scale detector, is currently under development. The target sensitivity of Phase-III TOBA is set to 1×10^{-15} $/\sqrt{\text{Hz}}$ at 0.1 Hz. Achieving this sensitivity requires reducing quantum noise, seismic noise, and thermal noise. Quantum noise reduction requires a highly sensitive optical system for torsional rotation measurement. Seismic noise reduction requires a suspension system with excellent vibration isolation performance. Thermal noise reduction requires cooling the torsion pendulum.

Previous research has established the basics for the cooling of torsion pendulums. Additionally, the development of elements for the optical system and suspension system has been conducted. It has been shown that vertical vibration isolation is necessary to reduce seismic noise, and that reducing the vibration of the optical bench is essential. However, a combined configuration of the optical system for torsional rotation measurement and the suspension system including the torsion pendulum has not yet been established and requires design and development. Therefore, this work designed and developed the optical and suspension systems for TOBA.

The optical system was designed to include a differential Fabry-Pérot cavity for highly sensitive measurements. This is the first configuration to install a differential Fabry-Pérot cavity into TOBA's torsional rotation measurement. Optical levers were also included as auxiliary sensors.

In the suspension system, this study was conducted with the foresight of using silicon test masses with good properties at low temperatures as the base material for the torsion pendulum in the future. The design was made such that the silicon would not crack when cooled. Additionally, to reduce translational seismic noise, a configuration was proposed where the vibrations of the optical bench do not contribute to the noise. For the first time in TOBA, the introduction of a geometric anti-spring (GAS) filter for passive vertical vibration isolation was implemented, along with the suspension of damping magnets.

We successfully constructed and evaluated the device that combines the optical and suspension systems. The measured values were: cavity finesse of 300, torsional resonant frequency of 117 mHz, Q factor of 50, tilt of the test mass of 2×10^{-3} rad, and resonant frequency of GAS filter from 3 Hz to 4.5 Hz. Using optical levers, the rotational motion of the torsion pendulums was measured, and the common-mode rejection between the two torsion pendulums was analyzed, achieving a sensitivity of 1.1×10^{-7} rad$/\sqrt{\text{Hz}}$ at 0.4 Hz. This established the fundamental configuration for Phase-III TOBA's optical and suspension systems. Furthermore, the sensitivity estimated by assuming the parameters obtained from the setup and rotational detection with the differential Fabry-Pérot cavity is 1×10^{-9} rad$/\sqrt{\text{Hz}}$ in the range of 0.1 Hz to 1 Hz, making it the world's best sensitivity for a torsion pendulum-type gravity gradiometer.

This established the fundamental configuration for TOBA's optical and suspension systems. The results of this study paved the way toward achieving the target sensitivity of TOBA. This dissertation reports the details of these achievements.

Thesis Supervisor: Masaki Ando (Professor)
Thesis Title: Torsion Pendulum with Interferometric Readout for Low-Frequency Gravity Gradient Observation

要旨

重力勾配の変動は、質量の動きを精密に計測できる重要な観測量である。特に、0.1 Hz から 10 Hz の低周波帯における重力勾配変動は、中間質量ブラックホール連星合体からの重力波の観測、地面や大気の擾乱によって生じるニュートニアン雑音の直接検出、地震の断層破壊で生じる重力場変動を利用した地震速報といった重要な科学的成果をもたらす。

重力波は、時空の歪みが宇宙を光速で伝播して伝わる現象であり、近年、天文学において重要な観測対象として注目されている。2015 年に重力波望遠鏡 Advanced LIGO（Laser Interferometer Gravitational-Wave Observatory) により初めて重力波の観測が達成されて以来、2023 年時点で約 90 イベントのコンパクト連星合体からの重力波が観測された。現在稼働中の重力波望遠鏡は 10 Hz から 1 kHz の周波数帯で高感度を実現するよう設計されている。観測周波数帯を低周波数まで拡大することによって、中間質量ブラックホール連星合体からの重力波を観測し、超巨大ブラックホール生成過程の解明に寄与することが期待されている。

ニュートニアン雑音は、地面や大気の擾乱によって生じる重力場変動である。重力波望遠鏡の試験マスを揺らし、原理的に重力波信号と区別することができないため、将来的に第 3 世代の地上の重力波望遠鏡の主要な雑音源になると予想されている。ニュートニアン雑音の振幅は低周波数帯で大きくなると理論的に予測されているが、直接検出によるモデル化や低減手法の確立が必要である。

また、近年、重力勾配観測を利用した地震速報も提案されている。重力勾配を利用した地震速報は、地震波を観測する現在の手法に比べて地震発生からの検出時間が早く、地震の規模の推定もより正確に行えることが期待されている。実現に向けて、地震の断層破壊で発生する 0.1 Hz 付近の重力場変動を高感度に検出することが求められている。

これらの対象の観測を目指し、ねじれ振り子型低周波重力勾配計 TOBA（Torsion-Bar Antenna）が提案されている。TOBA は重力勾配が及ぼすねじれ振り子の回転を測定する検出器である。共振周波数が低いねじれ振り子を用いることで、重力による束縛の強い地上においても 0.1 Hz から 10 Hz の低周波数帯での重力勾配変動の観測が可能になる。Final TOBA と呼ばれる 10 m スケールの検出器が最終目標であり、目標感度は 0.1 Hz において $1 \times 10^{-19}\ /\sqrt{\mathrm{Hz}}$ に設定されている。Final TOBA の実現に向けて、現在、35 cm スケールの小型検出器 Phase-III TOBA を開発中である。Phase-III TOBA の目標感度は、0.1 Hz において $1 \times 10^{-15}\ /\sqrt{\mathrm{Hz}}$ である。目標感度を達成するためには、量子雑音、地面振動雑音、熱雑音を低減する必要がある。量子雑音の低減には、ねじれ回転測定に感度の良い光学系が必要であり、地面振動雑音の低減には防振性能の良い懸架系が必要である。熱雑音の低減には、ねじれ振り子を冷却する必要がある。

これまでに行われた研究により、ねじれ振り子の低温化の基礎は確立されている。ま

た、光学系や懸架系の要素開発も行われ、地面振動雑音の低減のために、鉛直地面振動雑音低減のための縦防振が必要であること、光学ベンチの振動低減が必要であることが明らかになった。一方で、ねじれ回転測定のための光学系と、ねじれ振り子を含む懸架系を組み合わせた構成は確立されておらず、設計・開発が必要である。そこで、本研究ではTOBA の光学系と懸架系を組み合わせた設計・開発を行った。

光学系には、感度の良い差動 Fabry-Pérot 共振器を組み込んで設計を行った。TOBA のねじれ振り子回転測定に差動 Fabry-Pérot 共振器を導入したのは初めてである。補助センサとして、光てこも組み込んで設計した。

懸架系においては、本研究では、ねじれ振り子の基材として将来的に低温で特性の良いシリコン製のテストマスを使用することを見据え、シリコンが冷却時で割れない設計を行った。また、並進方向の地面振動雑音を低減するために、光学ベンチの振動が雑音にならない構成を提案し、TOBA 初となる縦防振のための geometric anti-spring (GAS) フィルタの導入、ダンピングマグネットの懸架も行った。

これらの光学系と懸架系を組み合わせた装置を製作した。動作に成功して性能評価を行った。共振器のフィネス 300、ねじれの共振周波数 117 mHz、ねじれの Q 値 50、テストマスの傾き 2×10^{-3} rad、GAS フィルタの共振周波数 3 Hz–4.5 Hz の測定値を得た。光てこを用いてねじれ振り子の回転を計測し、2 本のねじれ振り子間で同相雑音除去の解析を行って、0.4 Hz において 1.1×10^{-7} rad/$\sqrt{\text{Hz}}$ の感度を達成した。また、性能評価によって得られた測定値と差動 Fabry-Pérot 共振器での回転検出から推定される感度は 0.1 Hz から 1 Hz において 1×10^{-9} rad/$\sqrt{\text{Hz}}$ 程度となり、ねじれ振り子型重力勾配計として世界最高感度となる。

本研究の成果により、TOBA の光学系と懸架系の基本的な構成を確立し、TOBA の目標感度実現に向けた道を拓いた。本論文ではこれらの結果の詳細について報告する。

指導教員: 安東正樹 (教授)
論文題目: 低周波重力勾配観測のための高感度ねじれ振り子の開発

Contents

List of Figures

List of Tables

Glossary

Symbols

c	speed of light $c = 299\,792\,458\,\mathrm{m/s}$
e	elementary charge $e = 1.602 \times 10^{-19}\,\mathrm{C}$
g	gravitational acceleration $g = 9.806\,65\,\mathrm{m/s^2}$
G	gravitational constant $G = 6.674 \times 10^{-11}\,\mathrm{m^3/kg/s^2}$
$\hbar$	Dirac's constant $\hbar = 1.055 \times 10^{-34}\,\mathrm{J\,s}$
i	imaginary unit $i = \sqrt{-1}$
k_B	Boltzmann constant $k_\mathrm{B} = 1.381 \times 10^{-23}\,\mathrm{J/K}$
$M_\odot$	solar mass $M_\odot = 1.988 \times 10^{30}\,\mathrm{kg}$
μ_0	magnetic susceptibility of vacuum $\mu_0 = 1.257 \times 10^{-6}\,\mathrm{m\,kg\,s^{-2}\,A^{-2}}$
$d, \varnothing$	diameter
E	Young's modulus
f	Fourier frequency
f_0, f_m	mechanical resonant frequency
$\mathcal{F}$	cavity finesse
h	gravity strain, or strain of gravitational wave
h_0	Hubble constant in units of $100\,\mathrm{km/s/Mpc}$
H	transfer function
I	moment of inertia
l	length of cavity, length of bar, or length of wire
m, M	mass
M_w	magnitude
P	laser power, or pressure
Q	Q factor ($Q = 1/\phi$)
S	power spectral density
t	time
T	temperature
λ	laser wavelength
ν	laser frequency ($\nu = c/\lambda$), Poisson's ratio, or velocity
ϕ	loss angle, or tilt angle
ω	Fourier angular frequency
Ω_GW	energy per unit logarithmic interval frequency of stochastic gravitational wave

Acronyms

AC	alternating current
aLIGO	Advanced LIGO
AR	anti-reflection
ASD	amplitude spectral density
BS	beam splitter
CAD	computer-aided design
CMRR	common-mode rejection ratio
DC	direct current
DECIGO	DECi-hertz Interferometer Gravitational Wave Observatory
DoF	degree of freedom
EEW	earthquake early warning
EOM	electro-optic modulator
FSR	free spectral range
FWHM	full width at half maximum
GAS	geometric anti-spring (filter)
GRACE	Gravity Recovery and Climate Experiment
GW	gravitational wave
HR	high-reflection
HWP	half-wave plate
IM	intermediate mass
IMBH	intermediate-mass black hole
ISCO	innermost stable circular orbit
LIGO	Laser Interferometer Gravitational-Wave Observatory
LISA	Laser Interferometer Space Antenna
LPF	LISA Pathfinder
MIGA	Matter-wave laser Interferometric Gravitation Antenna
ND	neutral density (filter)
NN	Newtonian noise
OB	optical bench
oplev	optical lever
PD	photodiode
PDH	Pound-Drever-Hall (method)
PZT	piezoelectric transducer
QPD	quadrant photodiode
QWP	quarter-wave plate
RAM	residual amplitude modulation
RF	radio frequency
RoC	radius of curvature
SGWB	stochastic gravitational wave background

SMBH	supermassive black hole
SNR	signal-to-noise ratio
SOGRO	Superconducting Omni-directional Gravitational Radiation Observatory
SQUID	superconducting quantum interference device
SWIM$\mu\nu$	SpaceWire Interface demonstration Module $\mu\nu$
TM	test mass
TT	transverse traceless
TOBA	Torsion-Bar Antenna
TorPeDO	Torsion Pendulum Dual Oscillator
UGF	unity gain frequency
ZAIGA	Zhaoshan long-baseline Atom Interferometer Gravitation Antenna

Definition of coordinates for torsion pendulum

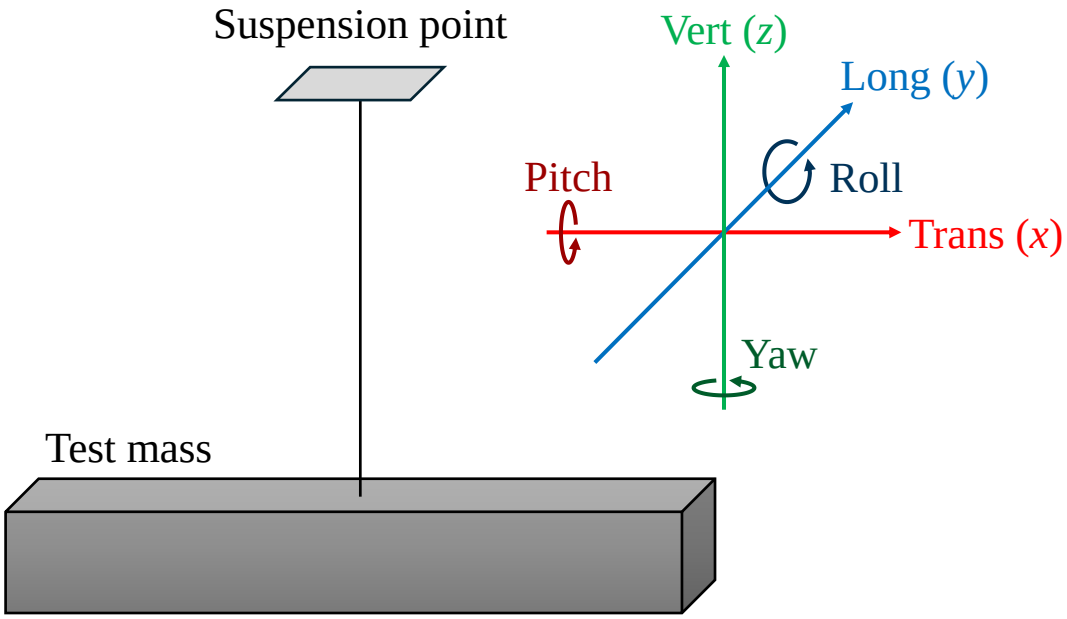

Figure 1: Model of a torsion pendulum and definition of coordinates.

1 Introduction

Observations of gravity gradients in the low-frequency band between 0.1 Hz and 10 Hz offer significant scientific opportunities, including:

- Astronomical observations through the detection of gravitational waves (GWs),
- Modeling Newtonian noise (NN) via direct detection,
- Earthquake early warning (EEW) based on gravity gradients.

First, we define the gravity gradient tensor and gravity strain in Section 1.1. Three observational targets are then introduced in Section 1.2, Section 1.3, and Section 1.4. Next, proposed detectors for observing low-frequency gravity gradients are summarized in Section 1.5. Finally, the purpose and outline of this thesis are described in Section 1.6.

1.1 Definition of gravity gradient tensor and gravity strain

A gravity gradient tensor $\boldsymbol{G}(\boldsymbol{x}, t)$ is defined as

$$\boldsymbol{G}(\boldsymbol{x}, t) = -\boldsymbol{\nabla} \otimes \boldsymbol{\nabla} \phi_{\mathrm{g}}(\boldsymbol{x}, t), \tag{1.1}$$

where $\phi_{\mathrm{g}}(\boldsymbol{x}, t)$ represents the gravitational potential. The relative gravitational acceleration between two nearby points $\boldsymbol{x}$ and $\boldsymbol{x} + \boldsymbol{\xi}$ is expressed as

$$\ddot{\boldsymbol{\xi}} = \boldsymbol{G}(\boldsymbol{x}, t) \cdot \boldsymbol{\xi}, \tag{1.2}$$

where $\dot{}$ denotes the derivative with respect to time t. Thus, each component of the gravity gradient tensor corresponds to the tidal force acting on masses.

In the following sections, the dimensionless gravity strain is also used. The gravity strain tensor $\boldsymbol{h}(\boldsymbol{x}, t)$ is related to the gravity gradient tensor by [1]

$$\boldsymbol{h}(\boldsymbol{x}, t) \equiv \frac{1}{2} \int_0^t \mathrm{d}t' \int_0^{t'} \mathrm{d}t'' \boldsymbol{G}(\boldsymbol{x}, t'') = \begin{pmatrix} h_{xx} & h_{xy} & h_{xz} \\ h_{yx} & h_{yy} & h_{yz} \\ h_{zx} & h_{zy} & h_{zz} \end{pmatrix}. \tag{1.3}$$

[1] The factor of 1/2 is necessary to correspond with the GW strain calculated in Section 1.2.1.

Since G_{ij} represents relative acceleration, its second time integral, h_{ij}, corresponds to the relative displacement between two free masses. Due to the apparent symmetry $G_{ij} = G_{ji}$ $(i, j = x, y, z)$ and the Poisson equation $\Delta\phi_{\mathrm{g}}(\boldsymbol{x}, t) = 0$, both $\boldsymbol{G}(\boldsymbol{x}, t)$ and $\boldsymbol{h}(\boldsymbol{x}, t)$ have only five independent components.

1.2 Gravitational waves at low frequencies

Gravitational waves (GWs) are ripples in spacetime that propagate at the speed of light, first predicted by Einstein in 1916 within the framework of general relativity [1, 2]. In recent years, GWs have become an increasingly important observational target in astronomy, as their detection enables the study of astrophysical and cosmological phenomena that cannot be observed through electromagnetic waves.

Since the first detection achieved by Advanced LIGO (Laser Interferometer Gravitational-Wave Observatory) in 2015 [3, 4], approximately 90 GW events from compact binary mergers have been detected as of 2023 [5]. These detections have enabled the exploration of black hole populations [6], the identification of the origin of short gamma-ray bursts [7], and the testing of general relativity under strong gravitational fields [8, 9]. For the binary neutron star coalescence detected in 2017 [10], its electromagnetic counterpart was identified and follow-up observations were carried out by many telescopes, from radio wave to gamma ray [7, 11]. Those observations contributed to identifying the physical scenario of short gamma-ray bursts [7]. Thus, GWs have opened a new era of multi-messenger astronomy.

The observational frequency band of current ground-based GW detectors is, however, limited to between 10 Hz and 1 kHz. Similar to electromagnetic wave astronomy, expanding the observational band is essential, as it enables the detection of a broader range of GW sources. Observing low-frequency GWs would allow us to detect events such as mergers of intermediate-mass black holes [12] and the stochastic GW background from the early universe [13, 14].

This section provides an overview of GW observation below 10 Hz. First, GWs are derived by linearizing the Einstein's equation, and their effects on masses are described. Subsequently, the main observational targets in this frequency band are introduced.

1.2.1 Theory of gravitational waves

Derivation of gravitational waves

In general relativity, the distance between two points x^μ and $x^\mu + \mathrm{d}x^\mu$ in four-dimensional spacetime is given by [2] [3]

$$\mathrm{d}s^2 = g_{\mu\nu}\mathrm{d}x^\mu \mathrm{d}x^\nu. \tag{1.4}$$

$g_{\mu\nu}$ is called the metric tensor. In general relativity, the metric tensor $g_{\mu\nu}$ completely characterizes the geometric properties of spacetime, that is, gravity.

For example, in flat spacetime (Minkowski spacetime) where no gravitational field is present,

$$g_{\mu\nu} = \eta_{\mu\nu} \equiv \begin{pmatrix} -1 & 0 & 0 & 0 \\ 0 & 1 & 0 & 0 \\ 0 & 0 & 1 & 0 \\ 0 & 0 & 0 & 1 \end{pmatrix}. \tag{1.5}$$

Since the metric tensor $g_{\mu\nu}$ determines the geometric properties of spacetime, the motion of a free particle can be derived. The trajectory traced by a particle is called a geodesic, and it is determined by the following geodesic equation:

$$\frac{\mathrm{d}^2 x^\lambda}{\mathrm{d}\tau^2} + \Gamma^\lambda{}_{\mu\nu}(x)\frac{\mathrm{d}x^\mu}{\mathrm{d}\tau}\frac{\mathrm{d}x^\nu}{\mathrm{d}\tau} = 0 \tag{1.6}$$

where τ is the proper time of the particle. $\Gamma^\gamma{}_{\alpha\beta}$ is called the connection coefficient or Christoffel symbol, and it is defined as follows:

$$\Gamma^\gamma{}_{\alpha\beta} \equiv \frac{1}{2}g^{\gamma\delta}\left(\frac{\partial}{\partial x^\alpha}g_{\beta\delta} + \frac{\partial}{\partial x^\beta}g_{\alpha\delta} - \frac{\partial}{\partial x^\delta}g_{\alpha\beta}\right). \tag{1.7}$$

The metric tensor $g_{\mu\nu}$ follows the Einstein's equation below:

$$R_{\mu\nu} - \frac{1}{2}g_{\mu\nu}R = \frac{8\pi G}{c^4}T_{\mu\nu}. \tag{1.8}$$

Here, R is called the Ricci scalar, and it is defined as follows:

$$R \equiv R_\mu{}^\mu = g^{\mu\nu}R_{\mu\nu}, \tag{1.9}$$

$$R_{\mu\nu} \equiv R^\alpha{}_{\mu\alpha\nu}, \tag{1.10}$$

$$R^\alpha{}_{\beta\gamma\delta} \equiv \frac{\partial}{\partial x^\gamma}\Gamma^\alpha{}_{\beta\delta} - \frac{\partial}{\partial x^\delta}\Gamma^\alpha{}_{\beta\gamma} + \Gamma^\alpha{}_{\gamma\mu}\Gamma^\mu{}_{\beta\delta} - \Gamma^\alpha{}_{\delta\mu}\Gamma^\mu{}_{\beta\gamma}. \tag{1.11}$$

[2] The Greek indices are assumed to take values from 0 to 3. That is, $x^\mu = (x^0, x^1, x^2, x^3) = (ct, x, y, z)$.

[3] Einstein's summation convention is adopted. That is, for indices that appear both as superscripts and subscripts, summation is implicitly performed, and the summation symbol is omitted:

$$\mathrm{d}s^2 = \sum_{\mu=0}^{3}\sum_{\nu=0}^{3} g_{\mu\nu}\mathrm{d}x^\mu \mathrm{d}x^\nu \equiv g_{\mu\nu}\mathrm{d}x^\mu \mathrm{d}x^\nu.$$

$R_{\mu\nu}$ is called the Ricci tensor, $R^{\alpha}{}_{\beta\gamma\delta}$ is called the Riemann tensor. Also, in Eq. (1.8), $T_{\mu\nu}$ is the energy-momentum tensor.

To derive the GW solution from Eq. (1.8), we assume that the gravitational field is sufficiently weak and perform a linear approximation for the metric tensor $g_{\mu\nu}$. Specifically, we consider the spacetime with a small perturbation added to Minkowski spacetime. In this case, the metric tensor $g_{\mu\nu}$ can be written using the small perturbation component $h_{\mu\nu}$ ($|h_{\mu\nu}| \ll 1$) as

$$g_{\mu\nu} = \eta_{\mu\nu} + h_{\mu\nu}. \tag{1.12}$$

Substitute this into equation Eq. (1.8) and consider terms up to the first order in $h_{\mu\nu}$.

At this point, the Christoffel symbols become, substituting Eq. (1.12) into Eq. (1.7),

$$\begin{aligned}\Gamma^{\gamma}{}_{\alpha\beta} &\simeq \frac{1}{2}\eta^{\gamma\delta}\left(\frac{\partial}{\partial x^{\alpha}}h_{\beta\delta} + \frac{\partial}{\partial x^{\beta}}h_{\alpha\delta} - \frac{\partial}{\partial x^{\delta}}h_{\alpha\beta}\right) \\ &= \frac{1}{2}\left(\frac{\partial}{\partial x^{\alpha}}h_{\beta}{}^{\gamma} + \frac{\partial}{\partial x^{\beta}}h_{\alpha}{}^{\gamma} - \frac{\partial}{\partial x_{\gamma}}h_{\alpha\beta}\right).\end{aligned} \tag{1.13}$$

By substituting this into Eq. (1.11), Eq. (1.10), and Eq. (1.9), the Riemann tensor, Ricci tensor, and Ricci scalar are respectively obtained as follows:

$$\begin{aligned}R^{\alpha}{}_{\beta\gamma\delta} &\simeq \frac{\partial}{\partial x^{\gamma}}\Gamma^{\alpha}{}_{\beta\delta} - \frac{\partial}{\partial x^{\delta}}\Gamma^{\alpha}{}_{\beta\gamma} \qquad (\because \Gamma\Gamma = \mathcal{O}(h^2)) \\ &= \frac{1}{2}\left(\frac{\partial^2 h^{\alpha}{}_{\delta}}{\partial x^{\beta}\partial x^{\gamma}} - \frac{\partial^2 h^{\alpha}{}_{\gamma}}{\partial x^{\beta}\partial x^{\delta}} + \frac{\partial^2 h_{\beta\gamma}}{\partial x_{\alpha}\partial x^{\delta}} - \frac{\partial^2 h_{\beta\delta}}{\partial x_{\alpha}\partial x^{\gamma}}\right),\end{aligned} \tag{1.14}$$

$$R_{\mu\nu} \simeq \frac{1}{2}\left(\frac{\partial^2 h^{\alpha}{}_{\nu}}{\partial x^{\mu}\partial x^{\alpha}} + \frac{\partial^2 h_{\mu\alpha}}{\partial x_{\alpha}\partial x^{\nu}} - \frac{\partial^2 h_{\mu\nu}}{\partial x^{\alpha}\partial x_{\alpha}} - \frac{\partial^2 h}{\partial x^{\mu}\partial x^{\nu}}\right), \tag{1.15}$$

$$R \simeq \frac{\partial^2 h_{\mu\nu}}{\partial x^{\mu}\partial x^{\nu}} - \Box h. \tag{1.16}$$

Here $h \equiv h_{\alpha}{}^{\alpha}$ and

$$\Box \equiv \frac{\partial^2}{\partial x^{\alpha}\partial x_{\alpha}} \tag{1.17}$$

is d'Alembertian. By substituting these into Eq. (1.8), the following equation can be obtained:

$$\frac{\partial^2 h_{\mu\alpha}}{\partial x^{\alpha}\partial x_{\nu}} + \frac{\partial^2 h^{\alpha}{}_{\nu}}{\partial x_{\alpha}\partial x^{\mu}} + \eta_{\mu\nu}\Box h - \Box h_{\mu\nu} - \frac{\partial^2 h}{\partial x^{\mu}\partial x^{\nu}} - \eta_{\mu\nu}\frac{\partial^2 h_{\alpha\beta}}{\partial x^{\alpha}\partial x^{\beta}} = \frac{16\pi G}{c^4}T_{\mu\nu}. \tag{1.18}$$

To simplify the expression of Eq. (1.18), the following quantity is introduced:

$$\bar{h}_{\mu\nu} \equiv h_{\mu\nu} - \frac{1}{2}\eta_{\mu\nu}h. \tag{1.19}$$

Substituting this into Eq. (1.18), we get:

$$\frac{\partial^2 \bar{h}_{\mu\alpha}}{\partial x_{\alpha}\partial x^{\nu}} + \frac{\partial^2 \bar{h}_{\nu\alpha}}{\partial x_{\alpha}\partial x^{\mu}} - \Box\bar{h}_{\mu\nu} - \eta_{\mu\nu}\frac{\partial^2 \bar{h}_{\alpha\beta}}{\partial x^{\alpha}\partial x^{\beta}} = \frac{16\pi G}{c^4}T_{\mu\nu}. \tag{1.20}$$

Furthermore, there is still degree of freedom (DoF) for the coordinate transformation in h, but we impose the following Lorentz gauge condition:

$$\frac{\partial}{\partial x^\nu}\bar{h}^{\mu\nu} = 0. \tag{1.21}$$

As a result, Eq. (1.20) can be linearized to the wave equation:

$$\Box\bar{h}_{\mu\nu} = -\frac{16\pi G}{c^4}T_{\mu\nu}. \tag{1.22}$$

We call Eq. (1.22) the linearized Einstein's equation.

Propagation of gravitational waves

The propagation of GWs in a vacuum can be obtained by considering the equation where $T_{\mu\nu} = 0$ in Eq. (1.22). In this case, Eq. (1.22) becomes:

$$\Box\bar{h}_{\mu\nu} = 0. \tag{1.23}$$

The solution is clearly a plane wave:

$$\bar{h}_{\mu\nu} = a_{\mu\nu}\exp(ik_\alpha x^\alpha). \tag{1.24}$$

From the properties of $\bar{h}_{\mu\nu}$, the amplitude $a_{\mu\nu}$ and the wave vector $k_\alpha = (\omega, k_x, k_y, k_z)$ satisfy the following conditions:

$$a_{\mu\nu} = a_{\nu\mu}, \tag{1.25}$$
$$a^{\mu\alpha}k_\alpha = 0, \tag{1.26}$$
$$k_\alpha k^\alpha = 0. \tag{1.27}$$

Eq. (1.26) represents that GWs are transverse waves, while equation Eq. (1.27) indicates that GWs propagate at the speed of light. Furthermore, to eliminate the remaining arbitrariness in the coordinate transformation, we impose the transverse traceless (TT) gauge conditions [4]:

$$h_{0\alpha} = 0, \tag{1.28}$$
$$h^j{}_j = 0, \tag{1.29}$$
$$\frac{\partial h^{jk}}{\partial x^j} = 0. \tag{1.30}$$

In the TT gauge, since $\eta^{\alpha\beta}h_{\alpha\beta} = 0$, we have $h_{\alpha\beta} = \bar{h}_{\alpha\beta}$ [5]. When GWs propagate in the z-direction, since $k_\alpha = (\omega, 0, 0, \omega/c)$, $a_{\mu\nu}$ can be expressed using the two independent functions h_+ and $h_\times$ as follows:

$$a_{\mu\nu} = \begin{pmatrix} 0 & 0 & 0 & 0 \\ 0 & h_+ & h_\times & 0 \\ 0 & h_\times & -h_+ & 0 \\ 0 & 0 & 0 & 0 \end{pmatrix}. \tag{1.31}$$

[4] The Latin indices are assumed to take values from 1 to 3. That is, $x^j = (x^1, x^2, x^3) = (x, y, z)$.

[5] From this point on, we do not distinguish between h and $\bar{h}$ in the TT gauge.

The modes corresponding to h_+ and $h_\times$ are called the plus (+) mode and cross (×) mode, respectively. From the above, it is clear that GWs in general relativity propagate at the speed of light and have two independent modes.

Effects of gravitational waves

The TT gauge considered in the previous sections is a coordinate system where the forces acting on particles cancel out as the coordinates change. However, the laboratory frame is not a coordinate system as in the TT gauge. Therefore, we consider only a sufficiently small region around a coordinate x.

The geodesic equation at a point x and at a nearby point $x+\xi$, separated by a small distance ξ, is given by:

$$\frac{\mathrm{d}^2 x^\mu}{\mathrm{d}\tau^2} + \Gamma^\mu{}_{\alpha\beta}(x)\frac{\mathrm{d}x^\alpha}{\mathrm{d}\tau}\frac{\mathrm{d}x^\beta}{\mathrm{d}\tau} = 0, \tag{1.32}$$

$$\frac{\mathrm{d}^2 (x^\mu+\xi^\mu)}{\mathrm{d}\tau^2} + \Gamma^\mu{}_{\alpha\beta}(x+\xi)\frac{\mathrm{d}(x^\alpha+\xi^\alpha)}{\mathrm{d}\tau}\frac{\mathrm{d}(x^\beta+\xi^\beta)}{\mathrm{d}\tau} = 0. \tag{1.33}$$

Taking the difference between these two equations and keeping terms up to the first order in ξ^μ, we obtain:

$$\frac{\mathrm{d}^2 x^\mu}{\mathrm{d}\tau^2} = -\xi^\sigma \frac{\partial \Gamma^\mu{}_{\alpha\beta}(x)}{\partial x^\sigma}\frac{\mathrm{d}x^\alpha}{\mathrm{d}\tau}\frac{\mathrm{d}x^\beta}{\mathrm{d}\tau}. \tag{1.34}$$

Here, we approximate $g_{\mu\nu} \simeq \eta_{\mu\nu}$ since we are considering small distances, and we use the fact that $\Gamma^\mu{}_{\alpha\beta} = 0$ because the derivatives of $g_{\mu\nu}$ vanish. If we assume that the laboratory frame moves slowly enough, we can write:

$$\frac{\mathrm{d}x^i}{\mathrm{d}\tau} \ll \frac{\mathrm{d}x^0}{\mathrm{d}\tau} = c. \tag{1.35}$$

In this case, for the α and β components in Eq. (1.34), we only need to consider the zero-component, and we can express the equation as:

$$\frac{\mathrm{d}^2 x^\mu}{\mathrm{d}\tau^2} = -c^2 \xi^\sigma \frac{\partial \Gamma^\mu{}_{00}(x)}{\partial x^\sigma}. \tag{1.36}$$

Furthermore, by setting $(\alpha,\beta,\gamma,\delta) = (\mu,0,\sigma,0)$ in Eq. (1.11), we get

$$\begin{aligned} R^\mu{}_{0\sigma0} &= \frac{\partial \Gamma^\mu{}_{00}}{\partial x^\sigma} - \frac{\partial \Gamma^\alpha{}_{0\sigma}}{\partial x^0} + \Gamma^\mu{}_{\alpha\sigma}\Gamma^\alpha{}_{00} - \Gamma^\mu{}_{\beta0}\Gamma^\beta{}_{0\sigma} \\ &= \frac{\partial \Gamma^\mu{}_{00}}{\partial x^\sigma} - \frac{\partial \Gamma^\alpha{}_{0\sigma}}{\partial x^0} \\ &= \frac{\partial \Gamma^\mu{}_{00}}{\partial x^\sigma}. \end{aligned} \tag{1.37}$$

Thus, Eq. (1.36) can be rewritten as:

$$\frac{\mathrm{d}^2 \xi^\mu}{\mathrm{d}\tau^2} = -c^2 \xi^\sigma R^\mu{}_{0\sigma0}. \tag{1.38}$$

The relationship between the Riemann tensor and GWs is given by Eq. (1.14) as

$$R^{\mu}{}_{0\sigma 0} = -\frac{1}{2c^2}\frac{\partial^2 h^{\mu}{}_{\sigma}}{\partial t^2}. \tag{1.39}$$

Since the Riemann tensor is gauge invariant, the GW amplitude h_{ij} can use the same form as in the TT gauge. Therefore, the geodesic equation in the laboratory frame is given by

$$\ddot{\xi}^i = \frac{1}{2}\ddot{h}^i{}_j \xi^j, \tag{1.40}$$

where $\dot{}$ denotes the derivative with respect to time t. The right hand term in Eq. (1.40) shows the tidal force from GWs in the laboratory frame. Note that compared to Eq. (1.2), the spatial component $\ddot{h}^i{}_j$ in Eq. (1.40) corresponds to the gravity gradient tensor defined in Eq. (1.2).

We consider how the position of a free mass changes due to GWs. By seeking a solution to Eq. (1.40) that does not diverge as $t \to \infty$, we obtain the following result:

$$\delta\xi^i = \frac{1}{2}h^i{}_j \xi^j. \tag{1.41}$$

Therefore, the change in ξ^i when GWs with angular frequency ω arrive from the z-axis direction can be derived from Eq. (1.24) and Eq. (1.31) as follows:

$$\begin{aligned}\begin{pmatrix}\delta x\\ \delta y\end{pmatrix} &= \frac{1}{2}\begin{pmatrix}h_+ & h_\times\\ h_\times & -h_+\end{pmatrix}\begin{pmatrix}x\\ y\end{pmatrix}\exp\left[i\omega\left(t-\frac{z}{c}\right)\right]\\ &= \frac{1}{2}h_+\begin{pmatrix}x\\ -y\end{pmatrix}\exp\left[i\omega\left(t-\frac{z}{c}\right)\right] + \frac{1}{2}h_\times\begin{pmatrix}y\\ x\end{pmatrix}\exp\left[i\omega\left(t-\frac{z}{c}\right)\right].\end{aligned} \tag{1.42}$$

The first and second terms represent the plus (+) mode and cross (×) mode polarizations of GWs, respectively. The plus (+) mode act as

$$\delta x = \frac{1}{2}h_+ x\cos(\omega t - k_z z), \tag{1.43}$$

$$\delta y = \frac{1}{2}h_+ y\cos(\omega t - k_z z), \tag{1.44}$$

where $k_z = \omega/c$ is the wave number, and the real part of Eq. (1.42) is used above. The plus (+) mode expands the masses in x-direction and compresses them in y-direction, and vice versa. The effects of the cross (×) mode are

$$\delta x + \delta y = \frac{1}{2}h_\times (x+y)\cos(\omega t - k_z z), \tag{1.45}$$

$$\delta x - \delta y = -\frac{1}{2}h_\times (x-y)\cos(\omega t - k_z z). \tag{1.46}$$

The cross (×) mode expands the masses in $(x+y)$-direction and compresses them in $(x-y)$-direction, and vice versa. The motion of the free masses due to these modes is illustrated in Fig. 1.1.

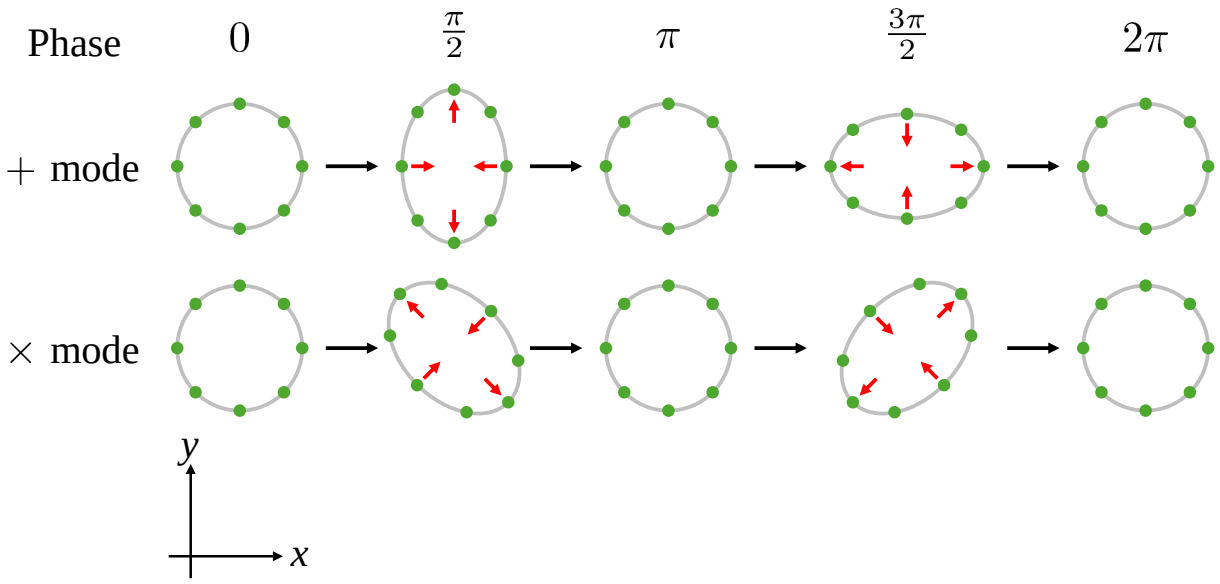

Figure 1.1: Time variation of free masses due to plus (+) mode and cross (×) mode polarizations of GWs. It is assumed that GWs are incident along z-axis.

Emission of gravitational waves

The emission of GWs from sources is considered. By formally solving Eq. (1.22), the amplitude of GWs is expressed as:

$$\bar{h}_{\mu\nu}(t,\boldsymbol{x}) = \frac{4G}{c^4}\int \frac{T_{\mu\nu}(t-|\boldsymbol{x}-\boldsymbol{x'}|/c,\boldsymbol{x'})}{|\boldsymbol{x}-\boldsymbol{x'}|}\mathrm{d}^3\boldsymbol{x'}. \tag{1.47}$$

Specifically, when the source's velocity is much smaller than the speed of light and we observe from a distance much greater than the GW's wavelength, Eq. (1.47) can be approximated as follows:

$$\bar{h}_{\mu\nu}(t,\boldsymbol{x}) \simeq \frac{4G}{c^4 r}\int T_{\mu\nu}(t-r/c,\boldsymbol{x'})\mathrm{d}^3\boldsymbol{x'}. \tag{1.48}$$

Here $r \equiv |\boldsymbol{x}-\boldsymbol{x'}|$ represents the distance from the observation point to the source of GWs. From the Lorentz gauge condition, which implies $\partial T_{\mu\nu}/\partial x_\mu = 0$, we derive the quadrupole formula:

$$\bar{h}_{ij}(t,\boldsymbol{x}) \simeq \frac{2G}{c^4 r}\ddot{Q}_{ij}(t-r/c), \tag{1.49}$$

Here, Q_{ij} is a quadrupole moment of the source, which is defined as

$$Q_{ij}(t) = \int x_i x_j \rho(t,\boldsymbol{x})\mathrm{d}^3\boldsymbol{x}. \tag{1.50}$$

$\rho(t,\boldsymbol{x}) \equiv T_{00}(t,\boldsymbol{x})$ represents the energy density of the GW source. It follows that GWs are generated by quadrupole radiation, unlike electromagnetic waves, which can include monopole or dipole components. As a result, GWs are emitted by the non-axisymmetric motion of the source.

1.2.2 Sources of gravitational waves at low frequencies

Two representative sources of GWs are introduced. Although there are many kind of sources, here we focus only on the targets for observation below 10 Hz.

Binary mergers of intermediate mass black holes

As shown in Eq. (1.49), GWs are radiated from time-varying quadruple moment of mass. One of promising sources in the universe is a compact binary coalescence. The orbit of a binary system shrinks due to the energy loss via GW radiation, and the angular frequency of the orbital motion gets higher [6]. As two objects get closer, the amplitude of the GW also increases since the gravitational interaction gets stronger. Such a waveform is called a chirp signal, characterized by a gradually increasing frequency and amplitude.

Consider a binary system of m_1 and m_2. The evolution of GW frequency $f_{\rm GW}(t)$ is given by

$$f_{\rm GW}(t) = \frac{1}{\pi}\left(\frac{5}{256}\right)^{\frac{3}{8}}\left(\frac{G\mathcal{M}_c}{c^3}\right)^{-\frac{5}{8}}(t_c - t)^{-\frac{3}{8}}, \tag{1.51}$$

where $\mathcal{M}_c \equiv (m_1 m_2)^{3/5}/(m_1+m_2)^{1/5}$ is the chirp mass of the binary, and t_c is the time of coalescence. Although $f_{\rm GW}$ goes to ∞ at $t \to t_c$, the actual frequency evolution stops when two stars merge into a single star. The period before the coalescence is called an inspiral phase. The later phase during the coalescence is called a merger phase, in which the waveform is available only by numerical calculations. In the ringdown phase after the merger phase, the merged star loses angular momentum via GWs. The overall waveform of a compact binary coalescence is given by these three phases. The frequency at the innermost stable circular orbit (ISCO), $f_{\rm ISCO}$, gives a characteristic frequency of the transition from the inspiral phase to the merger phase. The frequency is

$$f_{\rm ISCO} = \frac{c^3}{12\sqrt{6}\pi G M}. \tag{1.52}$$

Since $f_{\rm ISCO}$ is inversely proportional to the total mass $M \equiv m_1 + m_2$, binaries of heavy black holes are observed at low frequencies. The numerical value is

$$f_{\rm ISCO} \sim 0.1\,{\rm Hz} \times \left(\frac{2\times 10^4 M_\odot}{M}\right). \tag{1.53}$$

Therefore, observation of GWs around 0.1 Hz is sensitive to $10^4 M_\odot$–$10^5 M_\odot$ black holes. Such black holes cannot be observed with the current ground-based detectors, which is sensitive only above 10 Hz.

Fig. 1.2 shows expected gravitational radiation amplitude from merging binary black holes with masses of $10^3 M_\odot$–$10^6 M_\odot$ at the distance 4 Gpc. The frequency range of these GWs is from 1×10^{-4} Hz to 10 Hz, with amplitudes ranging from 10^{-22} to 10^{-18}. That is suitable for the observational frequency bands and target sensitivities of LISA and DECIGO, which will be introduced in Section 1.5, as well as Final TOBA, which will be explained in detail in Chapter 2.

[6] This was confirmed by Hulse and Taylor [15] as the first observational proof of GWs.

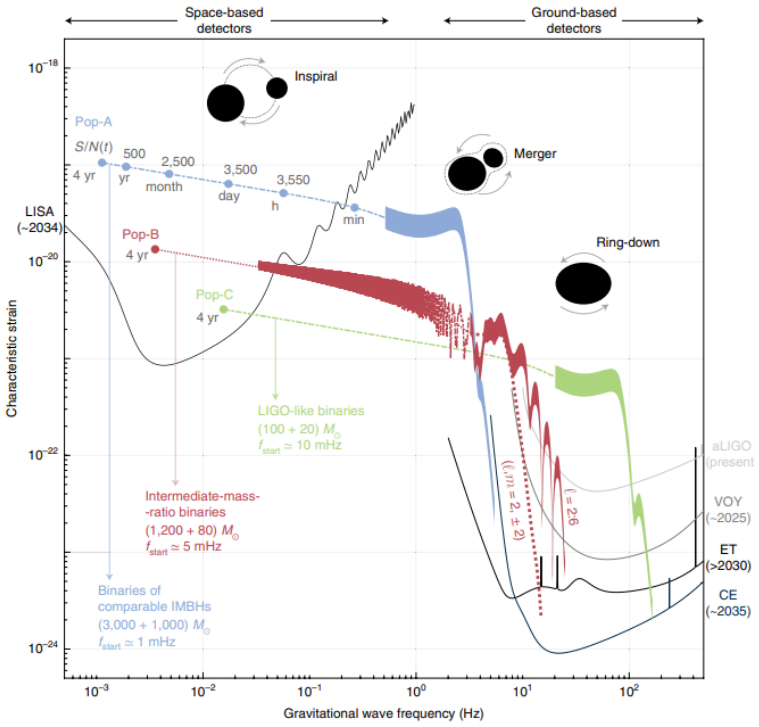

Figure 1.2: Expected GW amplitudes from merging binary black holes with masses of $(1200 + 80)M_\odot$ (red line) and $(3000 + 1000)M_\odot$ (blue line) at redshift $= 0.5$. This figure is taken from [16].

Black holes with the mass of $10^2 M_\odot$–$10^5 M_\odot$ are called intermediate-mass black holes (IMBHs) [17, 18]. They falls between stellar-mass black holes with the mass of $< 10^2 M_\odot$ and supermassive black holes (SMBHs) with the mass of $10^6 M_\odot$–$10^{10} M_\odot$. It is meaningful to observe coalescences of IMBH binaries since they are one of the candidate formation scenario of SMBHs at the center of galaxies [12, 18–20]. There have been several reports of possible IMBHs: $142 M_\odot$ formed from the merger event GW190521, with black holes of $85 M_\odot$ and $66 M_\odot$ [21, 22], $400 M_\odot$ in the galaxy M82 [23], $2.2 \times 10^3 M_\odot$ in the globular cluster 47 Tucanae [24], $3.2 \times 10^3 M_\odot$ in the central region of our Galaxy [25], and so on. Though the existence of IMBHs have come to be confirmed, the statistical properties are not unclear and also binary systems of IMBHs have not been found yet. Observation of low-frequency GWs would provide us valuable information about the merger rate of binary IMBHs and be useful to identify the formation scenario of SMBHs.

Stochastic gravitational wave background from the early universe

The other important source is the stochastic gravitational wave background (SGWB) from the entire sky. It is a superposition of GWs originating from spacetime fluctuations in the early universe and GWs from unresolved astronomical phenomena, such as mergers of white dwarf binaries. In particular, GWs from the early universe hold great significance. Electromagnetic waves cannot avoid interacting with the radiation field and, as a

result, lose information about the era before recombination. In contrast, due to the weak interaction of gravity with matter, GWs can pass through the radiation field, allowing us to observe the universe as it was before 0.38 million years after the Big Bang. This is one of the ultimate goals of GW observation.

The power spectral density of GWs from the early universe is characterized with its energy per unit logarithmic interval of frequency,

$$\Omega_{\mathrm{GW}}(f) = \frac{1}{\rho_c}\frac{\mathrm{d}\rho_{\mathrm{GW}}}{\mathrm{d}(\log f)}, \tag{1.54}$$

where ρ_{GW} is the energy density carried by SGWB, and ρ_c is the critical energy density of the universe,

$$\rho_c = \frac{3c^2H_0^2}{8\pi G}. \tag{1.55}$$

Here $H_0 \sim 68\,\mathrm{km/s/Mpc}$ is the present value of the Hubble constant. Using Ω_{GW}, the power spectral density of SGWB is given by

$$\sqrt{S_h(f)} = \sqrt{\frac{3H_0^2}{4\pi^2}\frac{\Omega_{\mathrm{GW}}(f)}{f^3}}. \tag{1.56}$$

Eq. (1.56) indicates that low frequency observation has an advantage for searching SGWB because $\sqrt{S_h(f)}$ is proportional to $f^{-3/2}$. According to a calculation based on an inflation model, Ω_{GW} is estimated to be $\sim 10^{-15}$. Substituting this and other values to Eq. (1.56), we get

$$\sqrt{S_h(f)} \sim 6\times10^{-25}\ /\sqrt{\mathrm{Hz}} \times \left(\frac{\Omega_{\mathrm{GW}}}{1\times10^{-15}}\right)^{\frac{1}{2}}\left(\frac{f}{0.1\,\mathrm{Hz}}\right)^{-\frac{3}{2}}. \tag{1.57}$$

Note that, because the waveform is stochastic, a single detector cannot distinguish the waveform from random detector noise. Correlating the signals from multiple detectors is necessary to extract the waveform of such background GWs.

1.3 Newtonian noise

In Section 1.2, we show that the effects on GWs can be interpreted as tidal forces acting on free-falling particles. However, tidal forces are also induced by the local gravity gradient. In principle, this local gravity gradient cannot be distinguished from GWs. In the context of GW detectors, this local gravitational gradient is called Newtonian noise (NN) [26].

1.3.1 Relationship between Newtonian noise and gravitational waves

Here, we examine the relationship between GWs and the local gravity gradient by considering the geodesic equation in the Newtonian limit.

Suppose there is a mass density distribution, ρ, and the velocity of the source, ν, is nonrelativistic, that is, $\nu \ll c$. If the gravitational field generated by the source is weak, we can decompose the metric tensor as $g_{\mu\nu} = \eta_{\mu\nu} + h_{\mu\nu}$ with $|h_{\mu\nu}| \ll 1$ as shown in Eq. (1.12). Additionally, since the source velocity is sufficiently small compared to c, the time derivatives of the metric induced by this source are given by

$$\frac{\partial}{\partial t} = O(\nu)\frac{\partial}{\partial x^i}. \tag{1.58}$$

With this approximation, we get the energy-momentum tensor $T^{\mu\nu}$, up to the lowest order,

$$T^{\mu\nu} = \begin{pmatrix} c^2\rho & 0 & 0 & 0 \\ 0 & 0 & 0 & 0 \\ 0 & 0 & 0 & 0 \\ 0 & 0 & 0 & 0 \end{pmatrix} + O\left(\frac{\nu}{c}\right). \tag{1.59}$$

To the lowest order the d'Alembertian is reduced to the Laplacian,

$$\Box = -\frac{1}{c^2}\frac{\partial^2}{\partial t^2} + \nabla^2 = \left(1 + O\left(\frac{\nu}{c}\right)^2\right)\nabla^2. \tag{1.60}$$

Therefore, the wave equation Eq. (1.47) is, to the lowest order, approximated to Poisson equations,

$$\nabla^2 \bar{h}_{\mu\nu} = -\frac{16\pi G}{c^4} T^{\mu\nu}. \tag{1.61}$$

Plugging Eq. (1.59) into Eq. (1.61), we get

$$\bar{h}_{00} = \frac{4G}{c^2}\int \frac{\rho(t, \boldsymbol{x'})}{|\boldsymbol{x} - \boldsymbol{x'}|}\mathrm{d}^3\boldsymbol{x'}, \tag{1.62}$$

$$\bar{h}_{0j} = \bar{h}_{ij} = 0. \tag{1.63}$$

Next, we replace $\bar{h}_{\mu\nu}$ with $h_{\mu\nu}$ as defined in Eq. (1.19).

$$h_{\mu\nu} = \bar{h}_{\mu\nu} - \frac{1}{2}\eta_{\mu\nu}\bar{h}, \tag{1.64}$$

$$\bar{h} = \eta^{\mu\nu}\bar{h}_{\mu\nu}. \tag{1.65}$$

Plugging Eq. (1.62) and Eq. (1.63) into them, we get

$$h_{00} = \frac{2G}{c^2}\int \frac{\rho(t, \boldsymbol{x'})}{|\boldsymbol{x} - \boldsymbol{x'}|}\mathrm{d}^3\boldsymbol{x'}, \tag{1.66}$$

$$h_{ij} = \delta_{ij}h_{00}, \tag{1.67}$$

$$h_{i0} = 0. \tag{1.68}$$

Now consider the geodesic equation in Newtonian limit. We can approximate $\tau \simeq t$ and $\mathrm{d}x^\mu/\mathrm{d}\tau \simeq (c, 0, 0, 0)$. Then we get

$$\frac{\mathrm{d}^2x^i}{\mathrm{d}\tau^2} = -\Gamma^i{}_{\mu\nu}\frac{\mathrm{d}x^\mu}{\mathrm{d}\tau}\frac{\mathrm{d}x^\nu}{\mathrm{d}\tau}. \tag{1.69}$$

From Eq. (1.62) and Eq. (1.63), the only non-zero term, in the leading order, of $h_{\mu\nu}$ is h_{00}. Therefore, we get

$$\frac{\mathrm{d}^2 x^i}{\mathrm{d}\tau^2} \simeq -c^2 \Gamma^i_{00} = c^2 \left(\frac{1}{2} \frac{\partial h_{00}}{\partial x^i} - \frac{\partial h^i{}_0}{\partial t} \right). \tag{1.70}$$

Comparing Eq. (1.70) to the Newtonian equation of motion, we get

$$h_{00}(\boldsymbol{x}) = -\frac{2}{c^2} \phi_{\mathrm{g}}(\boldsymbol{x}), \tag{1.71}$$

$$h_{ij}(\boldsymbol{x}) = -\frac{2}{c^2} \delta_{ij} \phi_{\mathrm{g}}(\boldsymbol{x}), \tag{1.72}$$

$$\mathrm{d}s^2 = -c^2 \left(1 + \frac{2\phi}{c^2} \right) dt^2 + \left(1 - \frac{2\phi}{c^2} \right) \delta_{ij} dx^i dx^j, \tag{1.73}$$

where $\phi_{\mathrm{g}}(\boldsymbol{x})$ the Newtonian gravitational potential used in Eq. (1.1). With these relations, we recover the Newtonian gravitational low,

$$\frac{\mathrm{d}^2 x^i}{\mathrm{d}t^2} = -\nabla \phi_{\mathrm{g}}(x). \tag{1.74}$$

Now consider the geodesic deviation between two points x^μ and $x^\mu + \xi^\mu$. Just like in the case of GWs, the geodesic deviation is given by

$$\frac{\mathrm{d}^2 \xi^i}{\mathrm{d}t^2} = -c^2 R^i{}_{0j0} \xi^i. \tag{1.75}$$

The Riemann tensor $R^i{}_{0j0}$ is given by Eq. (1.14). Substituting Eq. (1.71) and Eq. (1.72), we get

$$R^i{}_{0j0} = -\frac{1}{2} \left(\frac{\partial^2 h_{ij}}{\partial t^2} + \frac{\partial^2 h_{00}}{\partial x_i \partial x_j} \right). \tag{1.76}$$

From Eq. (1.58), we can estimate the order of $\partial^2 h_{ij} / \partial t^2$ as

$$\frac{\partial^2 h_{ij}}{\partial t^2} = O\left(\frac{\nu}{c} \right), \tag{1.77}$$

then we get, to the lowest order,

$$R^i{}_{0j0} = -\frac{1}{2} \frac{\partial^2 h_{00}}{\partial x_i \partial x_j} = \frac{1}{c^2} \phi_{\mathrm{g}}. \tag{1.78}$$

Substituting this into Eq. (1.38), we get

$$\frac{\mathrm{d}^2 \xi^i}{\mathrm{d}t^2} = \frac{\partial^2 \phi_{\mathrm{g}}}{\partial x_i \partial x_j} \equiv G_{ij} \xi^j, \tag{1.79}$$

where G_{ij} is the gravity gradient tensor defined in Eq. (1.1). Substituting Eq. (1.3) into Eq. (1.79), we get

$$\ddot{\xi}^i = \frac{1}{2} \ddot{h}^i{}_j \xi^j. \tag{1.80}$$

Comparing Eq. (1.80) with Eq. (1.40), we find that gravity strain corresponds to strain induced by GWs.

This indicates that we cannot distinguish the effect on free-falling particles, whether it is due to GWs or the local Newtonian gravity gradient. For this reason, every gravity gradient sensor, or gravity gradiometer, potentially works as a GW detector, and vice versa. From the perspective of GW detection, the local Newtonian gravity gradient is one of the fundamental noises that can limit the sensitivity of GW detection.

1.3.2 Estimated amplitude of Newtonian noise

There are several models about the mechanism of generation of NN, such as from seismic waves [27, 28], atmospheric fluctuation [29, 30], and moving objects like cryogenic coolers [31]. However, NN has so far only been theoretically predicted and has never been directly observed. The first things to do are to measure NN directly and to investigate the nature of the noise. Fig. 1.3 shows the estimated amplitude spectral density of NN. They are in the order of 10^{-15} $/\sqrt{\mathrm{Hz}}$ around 0.1 Hz. As detailed in Section 2.6, this is equivalent to the target sensitivity of Phase-III TOBA, making it possible to expect the first direct detection once Phase-III TOBA is completed.

Although NN does not exhibit wave-like behavior like GWs, it physically perturbs the test masses, making it fundamentally indistinguishable from GW signals [26, 27]. When highly sensitive, third-generation ground-based GW detectors such as Einstein Telescope [32] or Cosmic Explorer [33, 34] are built in the future, NN is expected to become a significant noise source [35, 36]. To address this, research has been proposed to monitor fluctuations in the surrounding Newtonian gravitational field and cancel out NN through feedforward techniques [37, 38], or to remove the mass around the detector [39]. If Phase-III TOBA successfully detects NN, it will contribute to enhancing the sensitivity of future ground-based GW detectors.

1.4 Earthquake early warning using gravity gradient

Earthquakes are caused by dynamic ruptures on faults. The released energy propagates outward as seismic waves and shakes the ground surface when the waves arrive. During this process, the density of crustal rocks is perturbed due to the compression and dilation of the medium induced by seismic waves. These density redistributions result in detectable gravity fluctuations around the epicenter. A schematic of earthquake early warning (EEW) is shown in Fig. 1.4.

A permanent change in gravitational acceleration was first detected by a superconducting gravimeter during the 2003 Tokachi-oki earthquake (moment magnitude $M_w = 8.0$) [41]. After that, two-dimensional distributions of gravity changes were observed by GRACE (Gravity Recovery and Climate Experiment) satellite for the 2004 Sumatra-Andaman earthquake ($M_w = 9.0$–9.3) [42], the 2010 Central Chile earthquake ($M_w = 8.8$) [43], and the 2011 Tohoku-oki earthquake ($M_w = 9.0$) [44]. These observations confirmed the static change in gravity by comparing the gravitational field before

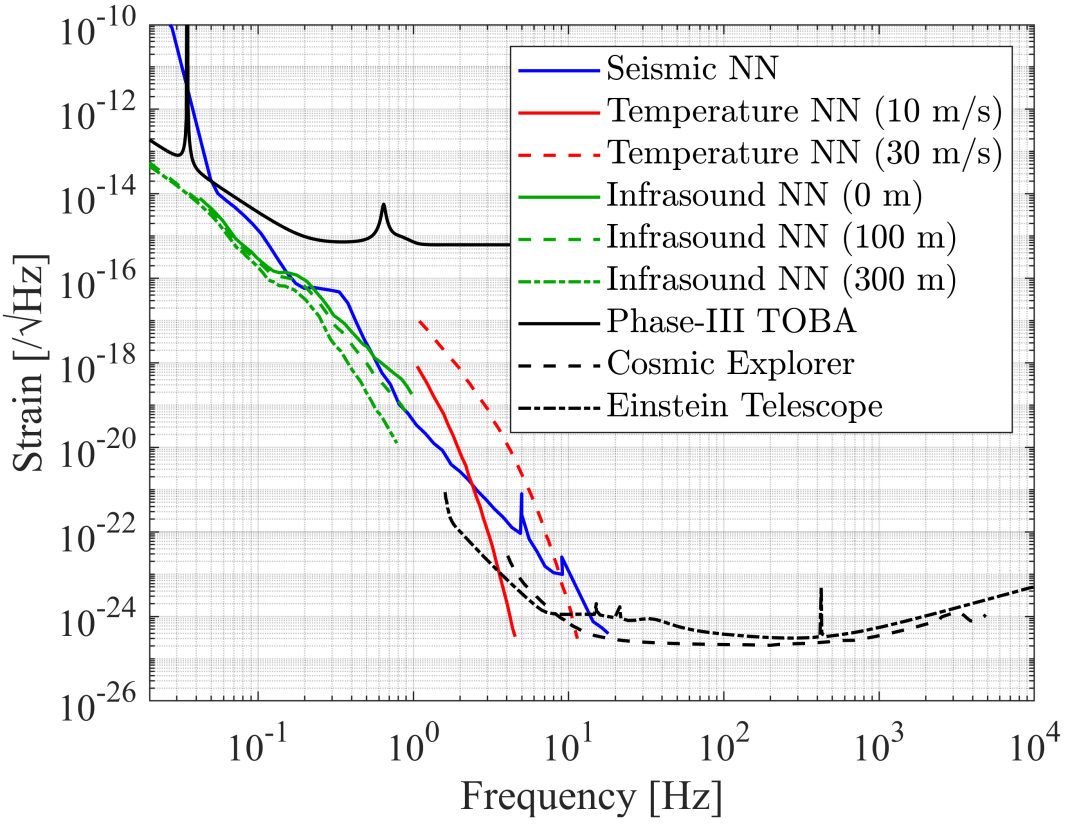

Figure 1.3: Estimated NN spectrum. Seismic NN at the KAGRA site [28] (blue). Atmospheric temperature NN at the Advanced Virgo site for different wind velocities [40]: 10 m/s (red solid line) and 30 m/s (red dashed line). Atmospheric infrasound NN for Phase-III TOBA for different depths [30]: 0 m (green solid line), 100 m (green dashed line), and 300 m (green dash-dotted line). For reference, the design sensitivities of Phase-III TOBA (calculated in Section 2.6.2), Cosmic Explorer [34], and Einstein Telescope [32] are shown as a black solid line, black dashed line, and black dash-dotted line, respectively.

and after the earthquakes.

Recently, it was proposed that transient changes in the gravitational field associated with large earthquakes can be detected by sensitive gravimeters or gravity gradiometers [45]. This focuses on gravity changes over a short timescale ($\sim$ 10 sec–100 sec), which are caused by propagating seismic waves. Since gravity changes propagate at the speed of light, detecting such changes can provide a faster earthquake warning signal than the current system using seismic P-waves. Additionally, the amplitude of the gravity signal is well correlated with the magnitude of the earthquake, making it a good early estimator of magnitude. The transient signal was observed during the 2011 Tohoku-oki earthquake by superconducting gravimeters and broadband seismometers around Japan. The first detection was reported in [46], with detailed analysis from several stations presented in [47–49]. The signals agreed well with simulations that included both gravity variations and induced ground acceleration due to the gravity change as shown in Fig. 1.5. Additional

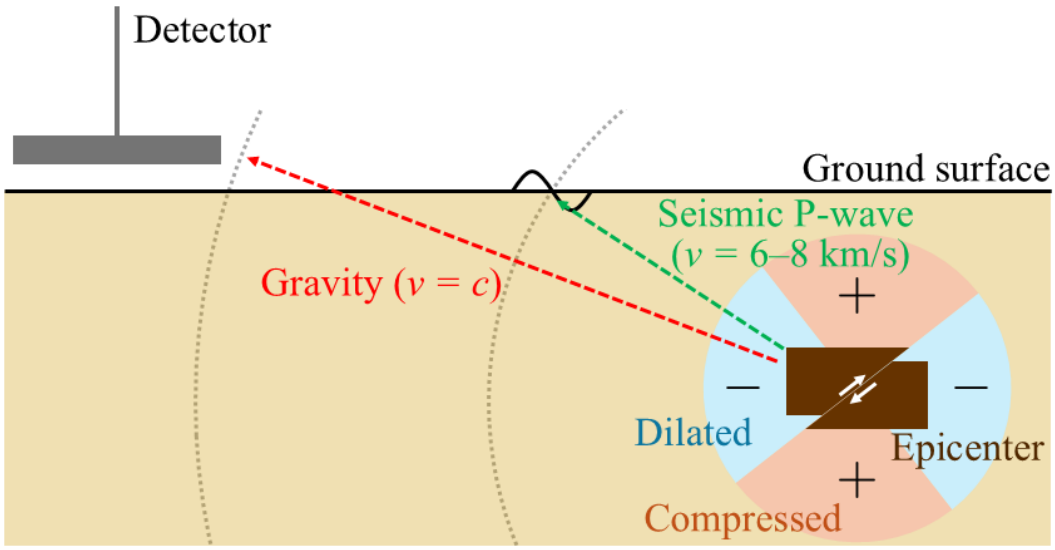

Figure 1.4: Overview of EEW using gravity gradient. A gravity gradient signal perturbs a detector prior to the arrival of a seismic P-wave.

detections for five other earthquakes were recently reported [50].

The existence of pre-P gravity signals is now widely accepted, but gravimetry is deemed ineffective for early earthquake detection due to decreased sensitivity caused by instrument acceleration [51, 52]. Since a gravimeter or a seismometer measures the relative acceleration between a free mass and a frame fixed to the ground, the gravitational acceleration on the free mass cannot be separated from the acceleration of the frame due to the equivalence principle. Thus, detections of small earthquakes ($M_w \lesssim 8$) are affected by background seismic noise. Additionally, a large fraction of the gravity change in the initial few tens of seconds is canceled out by the acceleration of the ground induced by the gravity change, as mentioned in [47]. This cancellation reduces the detectability of earthquakes in the early phases or from close distances. These issues can be addressed by measuring the gravity gradient, or the difference in gravitational force between two closely spaced points. Since the local acceleration of the ground is common to both points, gravity gradient signals can be distinguished from it. Therefore, gravity gradiometers are more suitable for an actual EEW system.

The detectability of earthquakes with gravity gradiometers is discussed in [53, 54]. It is shown that roughly $10^{-15}\ /\sqrt{\mathrm{Hz}}$ (in units of dimensionless strain h) of sensitivity at 0.1 Hz is required to realize meaningful detections. The target frequency of 0.1 Hz corresponds to the timescale of earthquakes and the required warning time. With such sensitivity, the detectable range of $M_w = 7$ earthquakes within 10 seconds is about 100 km. At further distances, up to 1000 km, the gravity signal can be detected preceding the arrival of seismic P-waves.

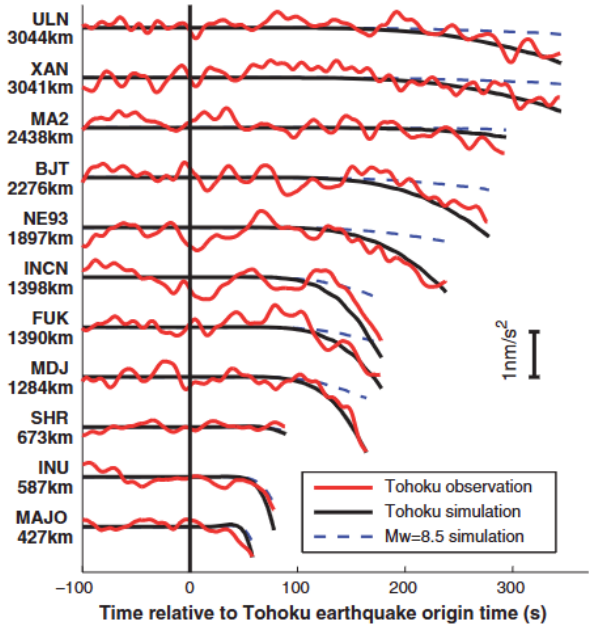

Figure 1.5: Observed gravitational signals from the Tohoku-oki earthquake revealed through post-event analysis. This figure is taken from [47].

1.4.1 Advantages of gravity-based earthquake early warning

Since gravity-based earthquake detection is based on a completely new principle, it provides independent observational information on earthquakes. It will enable us to explore unprecedented aspects of earthquakes. In terms of warning, such an independent detection will improve the reliability of early warnings. There are also practical advantages compared to the current warning system using seismic P-waves. The first advantage is shorter detection time, and the second advantage is better estimation accuracy of magnitude.

Detection time

In contrast to seismic P-wave detection, the detection time with gravitational signals strongly depends on the detector's sensitivity because the gravitational signal gradually increases as shown in Fig. 1.5. With the proposed gravity gradiometer sensitivity of $10^{-15}\ /\sqrt{\text{Hz}}$ at 0.1 Hz, the gravity gradient perturbation from earthquakes can be detected at around $h \sim 10^{-13}$ of the amplitude. In this case, gravity gradient observation provides an advantage of approximately 4 seconds at a 100 km epicentral distance compared to using P-waves.

In terms of warning time, the gravity-based warning system offers a significant advantage for events occurring in areas where seismometers have not been placed or are difficult to deploy. One example is offshore events, as networks of ocean-bottom seismometers are costly to install and maintain. This is because, even though a gravity gradiometer can achieve earlier detection than a seismometer at the same location, another seismometer near the epicenter may detect the event earlier than the gravity gradiometer in regions

where a dense network of seismometers already exists. In any case, the detection of gravity gradient perturbations can provide independent evidence of earthquake occurrence, improving the reliability and accuracy of the warning system.

Magnitude estimation

A fast magnitude estimation of an earthquake is also important. Magnitude estimations based on seismic waves are known to be uncertain for large earthquakes ($M_w \gtrsim 8.5$) because the seismic wave amplitude saturates for such events. In fact, the magnitude of the 2011 Tohoku-oki earthquake was initially underestimated, which led to an underestimation of tsunami amplitudes. In contrast, the signal amplitude of gravity perturbation is directly related to the energy of the earthquake. Therefore, it is expected to provide a more accurate early estimation of the magnitude, which also enables accurate tsunami warning. The estimation accuracy using a network of gravity gradiometers is simulated in [53]. The simulation shows that gravity gradient measurements can successfully provide real-time magnitude estimation starting from approximately 15 seconds after the onset of fault rupture.

1.5 Proposed detectors to observe low-frequency gravity gradient

As we have seen in the previous sections, both GWs and Newtonian gravity gradient act as tidal force on masses. Therefore they can be measured with the same detector configuration in principle. Actually, some of gravity gradiometers introduced here are originally proposed as GW detectors.

The current ground-based GW detectors, Advanced LIGO (Laser Interferometer Gravitational-Wave Observatory) [4], Advanced Virgo [55], GEO 600 [56], and KAGRA [28], are well-suited for observing GWs in the frequency range between 10 Hz and 1 kHz, but they exhibit low sensitivity at lower frequencies as shown in Fig. 1.6. The test masses are suspended using multi-stage pendulums to isolate vibrations from the ground and allow them to behave as free-falling masses. Constructing a suspension system that provides sufficient passive vibration isolation below the resonant frequency of ~ 1 Hz is challenging. This limitation is the reason why the observation band is restricted to frequencies above 10 Hz.

Therefore it is necessary to lower the resonant frequency of the system to observe gravity gradient below 10 Hz. The following detectors are proposed to observe low-frequency gravity gradient by using sophisticated systems or going into space. The design and achieved sensitivities of various proposed detectors are plotted in Fig. 1.6.

1.5.1 Torsion pendulums

Torsion pendulums can be used as low-frequency gravity gradiometers. They detect tidal forces induced by local gravity gradient fluctuations through the horizontal rotation of

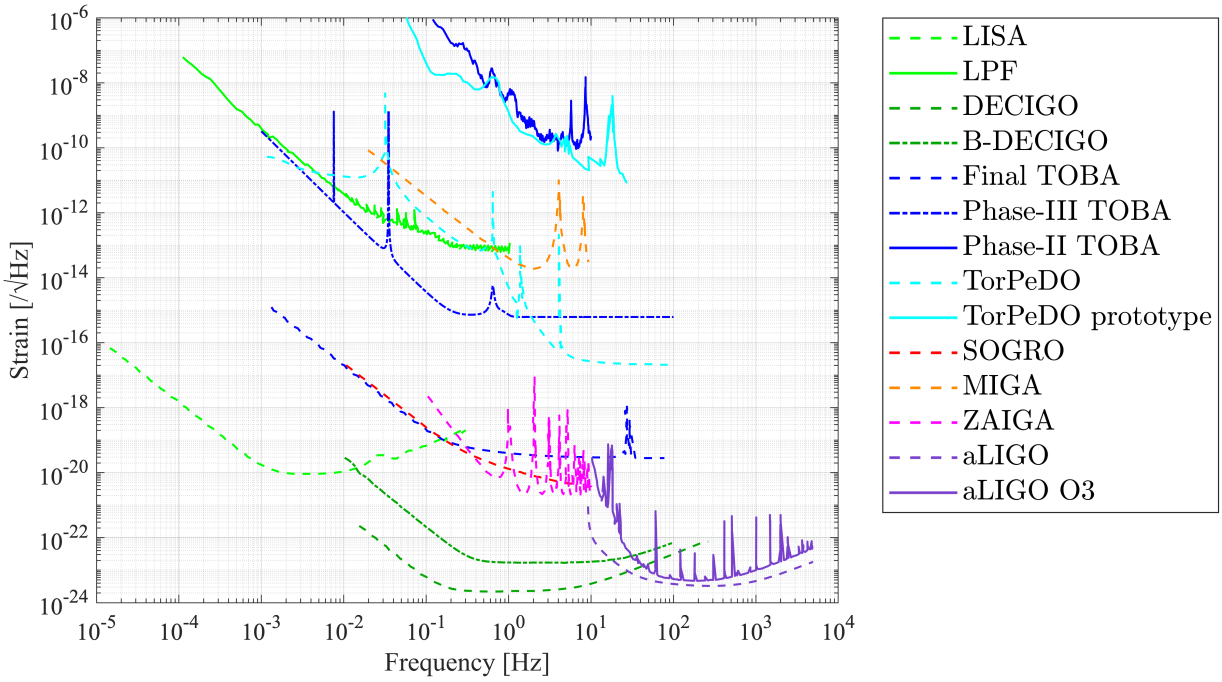

Figure 1.6: Sensitivity curves of various proposed detectors for observing low-frequency gravitational gradients. The dashed and dash-dotted lines represent design sensitivities, while the solid lines represent achieved sensitivities. The light green dashed line represents the design sensitivity of LISA [57] (data are taken from [58]). The light green solid line represents the achieved sensitivity of LPF (LISA Pathfinder) [59]. The LPF strain sensitivity is calibrated using the displacement sensitivity and the interferometer arm length of 376 mm. The green dashed line represents the design sensitivity of DECIGO [58], and the green dash-dotted line represents the design sensitivity of B-DECIGO [60]. The blue dashed line indicates the design sensitivity of Final TOBA [61] (detailed in Section 2.3), the blue solid line shows the achieved sensitivity of Phase-II TOBA [62] (detailed in Section 2.5), and the blue dash-dotted line represents the design sensitivity of Phase-III TOBA (calculated in Section 2.6.2). The cyan dashed line represents the design sensitivity of TorPeDO [63], and the cyan solid line shows the achieved sensitivity of TorPeDO prototype [64]. The red, orange, and magenta dashed lines correspond to the design sensitivities of SOGRO [65], MIGA [66], and ZAIGA [67], respectively. For reference, the design sensitivity of Advanced LIGO (aLIGO) [4] and the achieved sensitivity during O3 (Third Observing Run, from April 1, 2019, to April 21, 2020) [68] are also shown with purple dashed and solid lines, respectively.

suspended bars. Since torsion pendulums can achieve resonant frequencies on the order of millihertz, the horizontal rotational mode of the suspended bar behaves like a free-falling mass down to the millihertz band. This allows for a strong response to gravity gradients and effective passive isolation from rotational seismic noise. The bar's rotation is measured using laser interferometric sensors. The principle is quite similar to that of current GW detectors, which also measure the motion of test mirrors with laser interferometry. This similarity provides the advantage that techniques developed to improve the sensitivity of GW detectors can also be applied to torsion pendulum-type detectors. The technology for torsion pendulum detectors has already been demonstrated, and its sensitivity is theoretically determined by thermal noise and laser shot noise. Compared to superconducting gravity gradiometers, it has the advantage of being operable even at room temperature. Similar to the superconducting gravity gradiometers, offline noise removal is also possible. Here, two projects, TOBA and TorPeDO, are briefly introduced.

TOBA

TOBA (Torsion-Bar Antenna) has been proposed as a low-frequency GW detector in 2010 [61]. Several prototypes have been developed so far to demonstrate the system and characterized noise sources [62, 69–71]. Although the principle is the same as TorPeDO, the configuration for rotation readout and vibration isolation differs from that of TorPeDO. TOBA operates at cryogenic temperatures, employs fewer laser sources and optical cavities, and features a suspended optical bench. TOBA aligns the heights of the two torsion pendulums, uses a single suspension wire, and improves the flatness of the mirrors to reduce seismic noise. Further details are provided in Chapter 2.

TorPeDO

A detector using torsion pendulums, named TorPeDO (Torsion Pendulum Dual Oscillator), is also under development at Australian National University [63, 64, 72, 73]. It focuses on terrestrial targets such as NN detection and EEW [74].

Fig. 1.7 illustrates the configuration of TorPeDO. Unlike TOBA, each torsion pendulum in TorPeDO is suspended by two wires. Mirrors are mounted diagonally at the ends of the two torsion pendulums, forming four optical cavities (Cavities A, B, C, and D). This redundant configuration of four cavities facilitates seismic noise reduction through offline analysis of cavity length variations. The torsion pendulums lack actuators, and cavity control is achieved via feedback to the laser frequency, requiring four laser sources. Additionally, a reference laser is employed, bringing the total number of laser sources to five. Other differences from TOBA include the optical bench being fixed to an optical table rather than suspended, and the pendulum system comprising three stages.

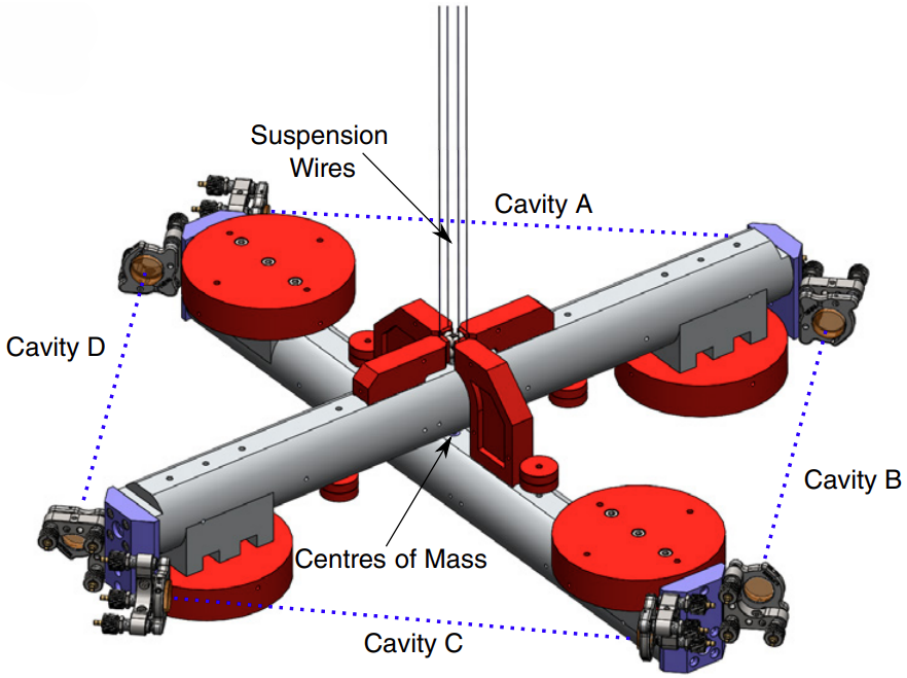

Figure 1.7: Configuration of TorPeDO. This figure is taken from [72].

1.5.2 Superconducting gravity gradiometers

Superconducting gravimeters have been used for geophysical observations. They use superconducting masses levitated by the Meissner effect, and these masses act as free-falling masses in at least one DoF. The free-falling DoFs are sensitive to low-frequency gravity fluctuations. By combining several levitated masses or by using the rotational mode of the masses, gravity gradients can also be measured. The motion of the superconducting mass induces a current in the superconducting circuit loop due to the Meissner effect, and the induced current is measured using a SQUID (Superconducting Quantum Interference Device). The principle is explained in [75]. Similar to torsion pendulums, the technology has already been demonstrated, and its sensitivity is determined by shot noise of SQUID and thermal noise. Compared to the torsion pendulums, it offers advantages such as higher reproducibility and easier offline noise reduction.

Recently, superconducting gravity gradiometers sensitive in all six DoFs have been proposed, and experimental results have been reported [76]. One such configuration, SOGRO (Superconducting Omni-directional Gravitational Radiation Observatory) [65, 77], is aimed at observing GWs below 10 Hz.

1.5.3 Atom interferometers

Atom interferometers use the interference of matter waves from free-falling atoms instead of electromagnetic waves. After the first experimental demonstration in 1991 [78], atom interferometers have been used for precise measurements, such as gravity acceleration

measurement [79], gyroscope applications [80], and gravity gradient measurement [81].

In atom interferometers, cold atoms interact with a sequence of three laser pulses as follows, working as a Mach-Zehnder interferometer. The first pulse (beam-splitter pulse) excites half of the atoms to an excited state. Excited atoms and atoms remaining in the ground state separate in space because the excited atoms gain velocity. Next, the second pulse (mirror pulse) is applied to reverse the two states. Finally, the third pulse (beam-splitter pulse) is applied again to interfere the states of the atoms. The effects of the gravitational field along the paths of the atoms are measured as the resulting interference pattern. The sensitivity is determined by shot noise from the number of atoms, and the technology is currently under demonstration. A notable feature is that the detector scale is on the order of several kilometers, which is larger compared to torsion pendulum and superconducting levitation types.

Recently, a hybrid of laser and atom interferometers was proposed to achieve higher sensitivities [82]. Unlike current GW detectors with mirrors suspended by pendulums, atom interferometers use free-falling atoms and are highly sensitive even in frequency bands below 10 Hz. MIGA (Matter-wave Laser Interferometric Gravitational Antenna) [66] and ZAIGA (Zhaoshan Long-baseline Atom Interferometer Gravitational Antenna) [67] are GW detectors using such a configuration. Atom interferometers along the vertical axis are located apart from the kilometer-scale arm, and they are linked by laser interferometers. Atom interferometers measure the phase shift of the laser induced by GWs during travel along the arm. Hence, these detectors are sensitive to GWs coming from the vertical direction.

1.5.4 Spaceborne gravitational wave detectors

There are several proposals for spaceborne GW detectors. Their primary advantages include the absence of seismic noise and the system's very low or zero resonant frequency. For these reasons, the proposed sensitivities for GWs are much better than those of terrestrial detectors as shown in Fig. 1.6. On the other hand, of course satellites are insensitive to earthquakes and NN because they are far away from terrestrial sources. The high costs associated with spacecraft development and the difficulty of performing maintenance during operation remain significant challenges. Here, two projects, LISA and DECIGO, are briefly introduced.

LISA

LISA (Laser Interferometer Space Antenna) [57] is a spaceborne detector developed in Europe. Its sensitive frequency band is between 1×10^{-4} Hz and 0.1 Hz, making it primarily suited for detecting GWs from the coalescence of SMBHs.

LISA features a baseline length of 2.5×10^9 m and consists of three spacecraft forming a triangular configuration. Each spacecraft is drag-free controlled with respect to the free-falling test masses inside it. The spacecraft follow an earth-like orbit around the sun. The relative displacement between the spacecraft is measured using an optical transponder.

The performance of acceleration noise for the test masses was successfully demonstrated by LISA Pathfinder (LPF), launched in 2015 [59].

DECIGO

DECIGO (DECi-hertz Interferometer Gravitational Wave Observatory) [58, 83] is a space mission developed in Japan. Its sensitive frequency band ranges from 0.1 Hz to 10 Hz, which bridges the frequency range between LISA and ground-based detectors. It aims to observe the stochastic GW background from the early universe, as well as the coalescence of intermediate-mass black holes.

DECIGO consists of three spacecraft and has a baseline length of 1×10^6 m. Displacement between the spacecraft is measured using Fabry-Pérot cavities along the baselines. The mirrors of the cavities are free-falling inside the spacecraft and are used as reference masses for drag-free control of the spacecraft.

Currently, the precursor mission B-DECIGO [60, 84] is planned to demonstrate the techniques for DECIGO and to achieve scientific observations.

1.6 Purpose and outline of this dissertation

This work focus on the development of the optical and suspension systems for the prototype TOBA, named Phase-III TOBA. With future cryogenic operation in mind, we designed the system with a potential sensitivity of 6.9×10^{-11} rad/$\sqrt{\text{Hz}}$ at 0.1 Hz, and succeeded in operating the optical and suspension systems, obtaining a sensitivity of 1.2×10^{-7} rad/$\sqrt{\text{Hz}}$ at 0.4 Hz. This thesis reports the details of these results.

This thesis paper consists of the following chapters. Chapter 2 summarizes the principles and design of TOBA and the prototype TOBA developed so far. Chapter 3 presents the purpose of the experiment, design sensitivity, and experimental setup. In Chapter 4, experimental results are reported and discussed. Finally Chapter 5 concludes the paper. Appendix A explain the details of the development of GAS filter. Appendix B summarizes the lists of devices used in the experiment.

2 Torsion-Bar Antenna

TOBA (Torsion-Bar Antenna) is a gravity gradiometer using a torsion pendulum targeting the frequency band of 0.1 Hz–10 Hz [61].

This chapter discusses its principles in Section 2.1, scientific targets in Section 2.2, design sensitivity in Section 2.3 and noise sources in Section 2.4. After that, the configurations and achieved sensitivities of the prototype TOBAs are described in Section 2.5. Finally, we introduce Phase-III TOBA currently under development and summarize the remaining challenges for Phase-III TOBA in Section 2.6.

2.1 Principle

In this section, the principle of a gravity gradiometer using torsion pendulums is explained. First, by analyzing the equations of motion under tidal forces caused by gravity gradients, it is shown that the test masses (TMs) experience rotational torque. Next, we describe that torsion pendulums exhibit a constant rotational response in frequency ranges above the resonance frequency of the torsional mode.

Fig. 2.1 shows a basic configuration of TOBA. Two torsion pendulums with TM bars suspended by wires are arranged orthogonally. The torsion pendulums rotate in response to tidal forces caused by gravity gradients. This rotational motion is detected using a laser interferometric sensor.

In the following discussions, the horizontal rotational plane of the suspended bars as the xy-plane. We focus on the rotation motion of a bar around z-axis, θ (see also Fig. 1).

2.1.1 Torque from gravity gradient

When a bar-shaped TM is suspended, it has the gravitational potential energy U as:

$$U = \int_V \mathrm{d}V \rho \phi_{\mathrm{g}}(\boldsymbol{r}), \tag{2.1}$$

where $\mathrm{d}V, \rho, \phi_{\mathrm{g}}(\boldsymbol{r})$ represents a small volume, density of the bar, and gravitational potential, respectively. The derivation of U with respect to rotational angle θ gives the

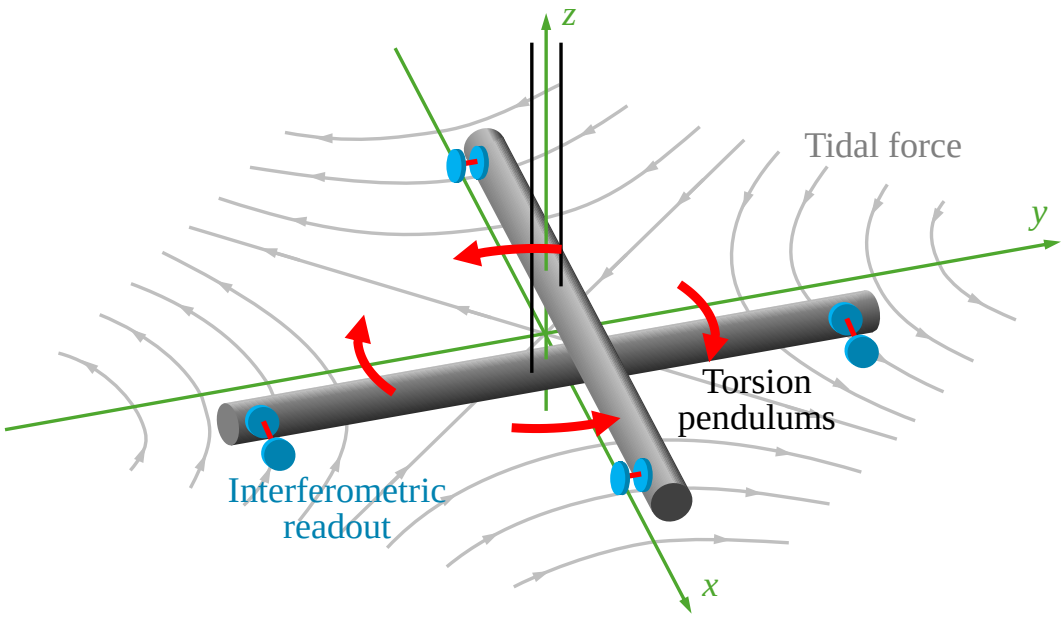

Figure 2.1: Schematic of TOBA.

gravitational torque on the bar:

$$N = -\frac{\partial U}{\partial \theta}. \tag{2.2}$$

Displacement of a point on the bar at $\boldsymbol{r}$ associated with the rotation θ is expressed as

$$\mathrm{d}\boldsymbol{r} = \boldsymbol{w}(\boldsymbol{r})\mathrm{d}\theta, \tag{2.3}$$

$$\boldsymbol{w}(\boldsymbol{r}) = (-y, x, 0), \tag{2.4}$$

where $\boldsymbol{w}(\boldsymbol{r})$ is called the mode function for the horizontal rotation. Then the derivation is

$$N = -\int_V \mathrm{d}V \rho \boldsymbol{w}(\boldsymbol{r}) \cdot \boldsymbol{\nabla}\phi_{\mathrm{g}}(\boldsymbol{r}). \tag{2.5}$$

Assuming that the gravity gradient $\boldsymbol{G}(\boldsymbol{r}) = -\boldsymbol{\nabla} \otimes \boldsymbol{\nabla}\phi_{\mathrm{g}}(\boldsymbol{r})$ (from Eq. (1.1)) is uniform within the size of the detector,

$$\partial_i \phi_{\mathrm{g}}(\boldsymbol{r}) = -G_{ij}x^j, \tag{2.6}$$

then

$$\begin{aligned} N &= G_{ij}\int_V \mathrm{d}V \rho w^i(\boldsymbol{r})x^j, \\ &= -\frac{G_{xx} - G_{yy}}{2}\int_V \mathrm{d}V\rho(2xy) + G_{xy}\int_V \mathrm{d}V\rho(x^2 - y^2). \end{aligned} \tag{2.7}$$

The two integrals are the quadruple moments of the bar, and here we define

$$q_+ \equiv -\int_V \mathrm{d}V\rho(2xy), \tag{2.8}$$

$$q_\times \equiv \int_V \mathrm{d}V\rho(x^2 - y^2). \tag{2.9}$$

N can be rewritten as follows:

$$N = \frac{G_{xx} - G_{yy}}{2} q_+ + G_{xy} q_\times. \tag{2.10}$$

In terms of gravity strain tensor defined in Eq. (1.3),

$$N = \frac{\ddot{h}_{xx} - \ddot{h}_{yy}}{4} q_+ + \frac{\ddot{h}_{xy}}{2} q_\times. \tag{2.11}$$

Eq. (2.10) and Eq. (2.11) tell that the horizontal rotation is sensitive to only three components of the gravity gradient tensor. According to the correspondence between the metric tensor of GWs and the gravity gradient tensor discussed in Section 1.2.1, the torque from GWs is given by

$$N = \frac{\ddot{h}_+}{2} q_+ + \frac{\ddot{h}_\times}{2} q_\times. \tag{2.12}$$

2.1.2 Mechanical response of torsion pendulums

The equation of motion for horizontal rotation around the z-axis is expressed as:

$$I\ddot{\theta}(t) + \kappa\theta(t) = N(t). \tag{2.13}$$

Here I is the moment of inertia around the rotational axis (that is, z-axis here), and κ is the torsional spring constant of the suspension wire. Taking the Fourier transform of both sides gives

$$\tilde{\theta}(f) = \frac{\tilde{N}(f)}{\kappa(1 + i\phi) - I(2\pi f)^2} = \frac{\tilde{N}(f)}{4\pi^2 I(f_0^2(1 + i\phi) - f^2)}, \tag{2.14}$$

where

$$f_0 = \frac{1}{2\pi}\sqrt{\frac{\kappa}{I}} \tag{2.15}$$

is the resonant frequency of the torsion pendulum. Here the loss angle ϕ is introduced as the imaginary part of the spring constant κ based on the structure damping model. ϕ indicates the amount of energy loss of the pendulum, and the Q factor of the pendulum is defined as $Q \equiv 1/\phi$. For a cylindrical wire with a diameter of d and length of l, κ is given by

$$\kappa = \frac{\pi E d^4}{64(1 + \nu)l}, \tag{2.16}$$

where E and ν are the Young's modulus and the Poisson's ratio of the suspension wire, respectively. The following mechanical response function is obtained from Eq. (2.14):

$$\chi(f) \equiv \frac{\tilde{\theta}(f)}{\tilde{N}(f)} = \frac{1}{4\pi^2} \frac{1}{f_0^2(1 + i\phi) - f^2}. \tag{2.17}$$

Plugging Eq. (2.11) into Eq. (2.14), we get induced rotation of the TM bars:

$$\tilde{\theta}(f) = \left(\frac{q_+}{4I}(\tilde{h}_{xx}(f) - \tilde{h}_{yy}(f)) + \frac{q_\times}{2I}\tilde{h}_{xy}(f)\right)\frac{f^2}{f_0^2(1+i\phi) - f^2}. \tag{2.18}$$

Next, consider the relation between the moment of inertia I and the quadrupole moment q_+ and $q_\times$. If the bar shape is a rectangular cuboid, with mass M and length along each axis l_x and l_y, we can write I, q_+, and $q_\times$ as

$$I = \int_V \rho(x^2 + y^2)\mathrm{d}V = \frac{1}{12}M(l_x^2 + l_y^2), \tag{2.19}$$

$$q_+ = \int_V \rho(-2xy)\mathrm{d}V = 0, \tag{2.20}$$

$$q_\times = \int_V \rho(x^2 - y^2)\mathrm{d}V = \frac{1}{12}M(l_x^2 - l_y^2). \tag{2.21}$$

$$\tag{2.22}$$

If the bar is along x-axis and the aspect ratio is enough large $l_x \gg l_y$, we can approximate $q_\times/I \simeq 1$, and we can rewrite Eq. (2.18) as

$$\tilde{\theta}(f) = \frac{\tilde{h}_{xy}(f)}{2}\frac{f^2}{f_0^2(1+i\phi) - f^2} \equiv H(f)\tilde{h}_{xy}(f). \tag{2.23}$$

Fig. 2.2 shows the response $H(f) = \tilde{\theta}(f)/\tilde{h}_{xy}(f)$ with different resonant frequencies and Q factors. Above the resonant frequency, the pendulum has flat response to the gravity strain, while it decreases below the resonant frequency. Therefore the lower resonant frequency provides wider observational frequency band. That is one of the reasons why torsion pendulums are suitable for low-frequency observation.

If the bar is along the y-axis and $l_y \gg l_x$, $|q_\times| \simeq 2I$ as well but the sign is flipped. That is, two bars along x-axis and along y-axis rotate in the opposite direction as shown in Fig. 2.1 [1]. Thus, we can reduce common noise of the bars by taking difference of rotation of each bars, $\theta_1 - \theta_2$.

2.2 Scientific targets

The scientific targets of TOBA are as follows:

- GWs from IMBH binaries (details in Section 1.2.2),
- SGWB (details in Section 1.2.2),
- NN detection and test of its models (details in Section 1.3),
- EEW using gravity gradients (details in Section 1.4).

[1] This is a similar situation as ground-based GW detectors, Two arm lengths change in the opposite way due to GWs.

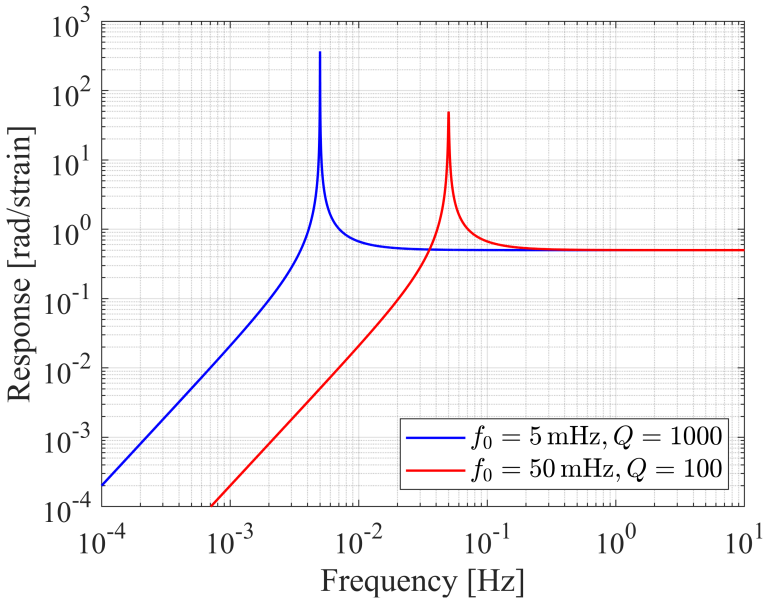

Figure 2.2: Frequency response of TOBA to gravity strain. Parameters with $f_0 = 5\,\mathrm{mHz}$ and $Q = 1000$ ($f_0 = 50\,\mathrm{mHz}$ and $Q = 100$) are assumed for the blue (red) line.

Table 2.1 summarizes the expected performance values for Final TOBA and Phase-III TOBA. The target sensitivities of Final TOBA and Phase-III TOBA are $1 \times 10^{-19}\ /\sqrt{\mathrm{Hz}}$ and $1 \times 10^{-15}\ /\sqrt{\mathrm{Hz}}$ at 0.1 Hz, respectively. The details are described in Section 2.3 and Section 2.6 below.

Table 2.1: Expected performance of Final TOBA and Phase-III TOBA for various scientific targets.

Target	Final TOBA	Phase-III TOBA
IMBHs	Distance within 10 Gpc (as shown in Fig. 2.3)	Distance within 1 Mpc
SGWB	Limit on $\Omega_{\mathrm{GW}} < 10^{-7}$ at $f \sim 0.1$ Hz [61]	Limit on $\Omega_{\mathrm{GW}} < 10$ at $f \sim 0.1$ Hz [69]
NN	Detection with SNR of 10^4–10^5 [85][2]	First direct detection [28, 30]
EEW	Detection for earthquakes with $M_w = 6.0$ and located 1000 km from the epicenter [85]	Detection within 10 s of the rupture onset for earthquakes with $M_w = 7.0$ and located 120 km from the epicenter [53, 54]

[2]As discussed in Section 1.3, NN is the noise in terms of observing other targets, and it is necessary to subtract it.

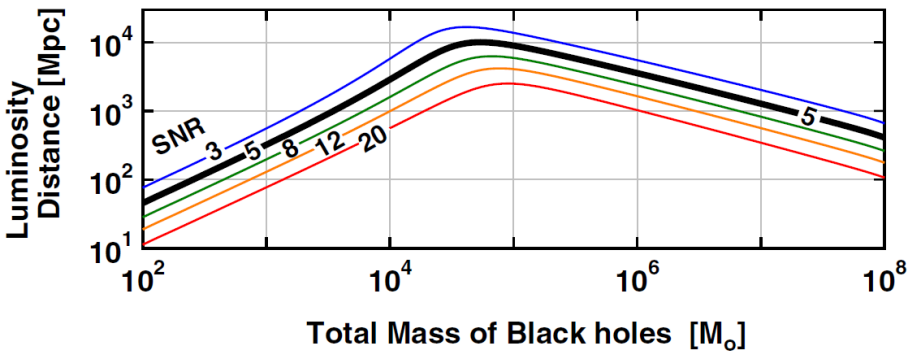

Figure 2.3: Luminosity distance of IMBH binary mergers observable with Final TOBA. This figure is taken from [61].

2.3 Design sensitivity of Final TOBA

The target sensitivity of the final stage TOBA (Final TOBA) is 1×10^{-19} $/\sqrt{\text{Hz}}$ from 0.1 Hz to 10 Hz as shown in Fig. 2.4. The sensitivity is limited by radiation pressure noise below 0.1 Hz and by shot noise above 0.1 Hz. Between 0.1 Hz and 1 Hz, bar thermal noise is dominant. The design parameters of Final TOBA required to achieve the target sensitivity are summarized in Table 2.2.

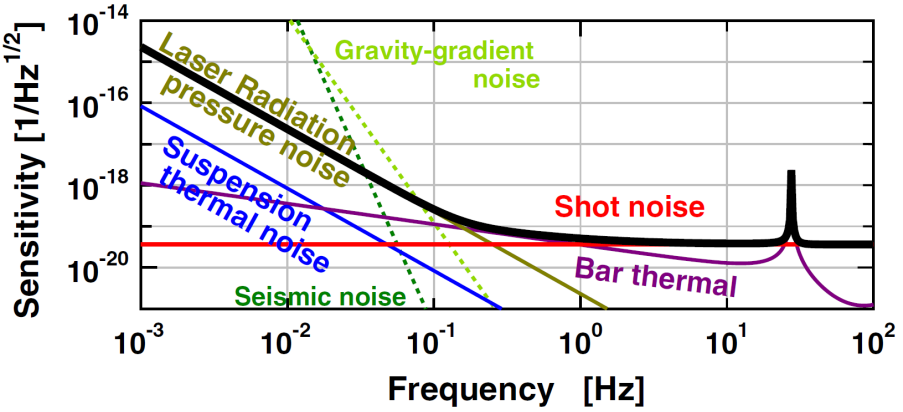

Figure 2.4: Design sensitivity of Final TOBA. The black thick line shows the target sensitivity, while solid lines in other colors indicate contributions from fundamental noise sources. The green dotted lines represent seismic noise and NN. This figure is taken from [61].

Table 2.2: Design parameters of Final TOBA [61].

Parameter	Value
Material of TM	Aluminum
Length of TM	10 m
Diameter of TM	0.6 m
Mass of TM	7600 kg
Moment of inertia of TM	6.4×10^4 kg m^2
Loss angle of TM	10^{-7}
Resonant frequency of torsion pendulum	1 mHz
Damping factor of torsion pendulum [3]	1×10^{-10} Hz
Wavelength of laser	1064 nm
Power of laser	10 W
Finesse of Fabry-Pérot cavity	100
Temperature	4 K

2.4 Noise sources

2.4.1 Thermal noise

Thermal noise is one of the fundamental noise sources in TOBA. Each DoF of the detector is excited by the thermal bath, causing random fluctuations over time, a phenomenon known as Brownian motion. According to the fluctuation-dissipation theorem, thermal noise is generally expressed as:

$$\sqrt{S_{\rm th}(f)} \propto \sqrt{T\phi}, \tag{2.24}$$

where T is the temperature, and ϕ is the loss angle associated with each DoF. Therefore, a common approach to reducing thermal noise is to cool down the system and use materials with low mechanical loss for each component. The way thermal noise couples to the rotational measurement varies depending on the specific DoF in the system. Below, we introduce three types of thermal noise: suspension thermal noise, bar thermal noise, and mirror thermal noise.

Suspension thermal noise

Energy loss via the suspension wire determines the torque noise of the wire. Thermal noise in mechanical suspension systems were investigated in [86]. In terms of the horizontal

[3] In Ref. [61], the unit is given as N m s, but the correct unit is Hz.

rotation of the bar, the amplitude spectral density (ASD) is given by:

$$\sqrt{S_{\mathrm{th,sus}}(f)} = \sqrt{-\frac{4k_{\mathrm{B}}T}{2\pi f}\mathrm{Im}\left[\frac{\tilde{\theta}(f)}{\tilde{N}(f)}\right]}$$
$$= \sqrt{\frac{k_{\mathrm{B}}T}{2\pi^3 I f}\frac{\phi f_0^2}{\left(f^2-f_0^2\right)^2+\phi^2 f_0^2}} \qquad (\because \text{Eq.(2.17)}) \tag{2.25}$$

where T is the system temperature, I is the moment of inertia in the rotational direction, ϕ is the loss factor (the inverse of the Q factor), and f_0 is the resonance frequency of the rotation. For frequencies much larger than the resonance frequency ($f \gg f_0$), we have:

$$\sqrt{S_{\mathrm{th,sus}}(f)} \simeq \sqrt{\frac{k_{\mathrm{B}}T\phi f_0^2}{2\pi^3 I f^5}} = \sqrt{\frac{k_{\mathrm{B}}T\phi\kappa}{8\pi^5 I^2 f^5}} \qquad (\because \text{Eq.(2.15)}), \tag{2.26}$$

where κ is the torsional spring constant of the suspension wire. Therefore, small κ and large I can reduce the thermal noise. Note that κ and I are not completely independent in an actual suspension system because the thickness of the wire is related to the mass to be suspended. When the size of the detector is fixed, mass should be concentrated at the outer ends (like a dumbbell) to increase I while keeping κ small.

Using low loss wire is also essential to reduce the suspension thermal noise. In general, energy loss of the wire ϕ has several origins such as energy loss on the surface and loss inside the bulk.

Bar thermal noise

The second type of thermal noise is bar thermal noise. This refers to the Brownian motion of one of the internal modes of the bar. Since TOBA measures the rotational motion of the bar, only the internal modes that move in opposite directions at the two ends of the bar contribute to the sensitivity.

In the following calculations, the bar is aligned to x-axis and we consider the modes in xy-plane. The lowest order odd functional mode of a rectangular bar with length along each axis $l_{\mathrm{bar}} \equiv l_x$, l_y and l_z ($l_{\mathrm{bar}} \gg l_y, l_z$) is given by

$$y_2(x) = \sqrt{\frac{2}{\cosh^2\alpha_2+\cos^2\alpha_2}}\left(\cos\alpha_2\cdot\sinh\frac{2\alpha_2 x}{l_{\mathrm{bar}}}+\cosh\alpha_2\cdot\sin\frac{2\alpha_2 x}{l_{\mathrm{bar}}}\right), \tag{2.27}$$
$$\alpha_2 \simeq 3.9266, \tag{2.28}$$

where α_2 is the second lowest root of the following equation:

$$\tan\alpha_2 = \pm\tanh\alpha_2. \tag{2.29}$$

The eigenfrequency ω_2 is

$$\omega_2 = \sqrt{\frac{4El_y^3 l_z}{Ml_{\mathrm{bar}}^2}}\alpha_2^2. \tag{2.30}$$

Here, M and E represent the mass and Young's modulus of the bar, respectively. The eigenmode can be analyzed in the same manner as the rotational mode of the suspension thermal noise. Note that the conversion to angular fluctuation depends on the method used to measure the rotation. For simplicity, the angular fluctuation at the center of the bar is calculated below. The ASD of the thermal fluctuation is

$$\sqrt{S_{\mathrm{th,bar}}(f)} \simeq \frac{5.3962}{l_{\mathrm{bar}}} \sqrt{\frac{4k_{\mathrm{B}}T}{\omega} \frac{\omega_2^2 \phi}{M|\omega_2^2(1+i\phi) - \omega^2|^2}}. \tag{2.31}$$

Here ϕ is the loss angle of the bar.

The frequency band of interest (below 1 Hz) is typically lower than the bar's eigenfrequency. In this case, a higher value of ω_2 results in reduced thermal noise. Therefore, the bar should be designed to resist bending to minimize the noise.

Mirror thermal noise

Each mirror has a coating layer on its substrate surface to control reflectivity. Both the substrate and the coating contribute to the thermal noise. The displacement thermal noise for an infinite substrate measured with a Gaussian laser beam was calculated in [87] , and later, the authors of Ref. [88] included the contribution of the coating layer. Based on their calculations, the angular thermal noise, when the rotation is measured using two Gaussian laser beams at two points separated by D, is given as:

$$\sqrt{S_{\mathrm{th,mir}}(f)} = \frac{\sqrt{2}}{D} \sqrt{\frac{4k_{\mathrm{B}}T}{\omega} \frac{1-\nu_{\mathrm{s}}^2}{\sqrt{\pi}E_{\mathrm{s}}} \frac{\phi_{\mathrm{mir}}}{w}}, \tag{2.32}$$

$$\phi_{\mathrm{mir}} \equiv \phi_{\mathrm{s}} + \frac{d_{\mathrm{c}}}{\sqrt{\pi}w} \left(\frac{E_{\mathrm{c}}}{E_{\mathrm{s}}} \frac{(1+\nu_{\mathrm{s}})(1-2\nu_{\mathrm{s}})^2}{(1-\nu_{\mathrm{s}})(1-\nu_{\mathrm{c}}^2)} + \frac{E_{\mathrm{s}}}{E_{\mathrm{c}}} \frac{(1+\nu_{\mathrm{c}})(1-2\nu_{\mathrm{c}})}{(1-\nu_{\mathrm{s}}^2)(1-\nu_{\mathrm{c}})} \right) \phi_{\mathrm{c}}. \tag{2.33}$$

The parameter w represents the radius of the laser beam (where the intensity drops to $1/e^2$ of its maximum), and d_{c} is the thickness of the coating layer. The terms E_{s}, ν_{s} and ϕ_{s} correspond to the Young's modulus, Poisson's ratio, and loss angle of the mirror substrate, respectively. Similarly, E_{c}, ν_{c} and ϕ_{c} represent the same properties for the coating layer. Here, ϕ_{c} is assumed to be isotropic.

Although the separation of the measurement points, D, should be as large as possible, it cannot exceed the length of the bar, l_{bar}. Using a larger laser beam radius is more effective in reducing the mirror thermal noise.

2.4.2 Quantum noise

Another fundamental noise source is quantum noise, originating from the quantum fluctuations of laser light. According to [89], the quantum noise in displacement measurement by an interferometer is generally expressed as:

$$\sqrt{S_{\mathrm{QN}}(f)} = \frac{\theta_{\mathrm{SQL}}(f)}{\sqrt{2}} \sqrt{\frac{1}{|\mathcal{K}(f)|} + |\mathcal{K}(f)|}, \tag{2.34}$$

$$\theta_{\mathrm{SQL}} = \sqrt{2\hbar|\chi(f)|}. \tag{2.35}$$

Here, $\mathcal{K}(f)$ is called the Kimble factor, which depends on the configuration of the interferometer. θ_{SQL} is the standard quantum limit and $\chi(f)$ given by Eq. (2.17). The second term in Eq. (2.34) corresponds to the phase fluctuation of photons, commonly known as shot noise. The first term in Eq. (2.34) represents the back-action of the measurement, called radiation pressure noise. For a Fabry-Pérot Michelson interferometer, $\mathcal{K}(f)$ is given by

$$\mathcal{K}(f) = \frac{16 l_{\mathrm{bar}}^2 \mathcal{F}^2}{|1 + if/f_{\mathrm{c}}|^2} \frac{P_0}{\pi c \lambda} \chi(f) \tag{2.36}$$

and the quantum noise is given by

$$\sqrt{S_{\mathrm{QN}}(f)} = \sqrt{S_{\mathrm{shot}}(f) + S_{\mathrm{RP}}(f)}, \tag{2.37}$$

$$\sqrt{S_{\mathrm{shot}}(f)} = \frac{\theta_{\mathrm{SQL}}(f)}{\sqrt{2}} \frac{1}{\sqrt{\mathcal{K}(f)}} = \frac{1}{4 l_{\mathrm{bar}} \mathcal{F}} \sqrt{\frac{\pi c \hbar \lambda}{P_0}} \left| 1 + i \frac{f}{f_{\mathrm{c}}} \right|, \tag{2.38}$$

$$\sqrt{S_{\mathrm{RP}}(f)} = \frac{\theta_{\mathrm{SQL}}(f)}{\sqrt{2}} \sqrt{\mathcal{K}(f)} = \frac{4 l_{\mathrm{bar}} \mathcal{F}}{|1 + if/f_{\mathrm{c}}|} \sqrt{\frac{\hbar P_0}{\pi c \lambda}} |\chi(f)|, \tag{2.39}$$

$$\tag{2.40}$$

where λ is the wavelength of the laser, P_0 is the incident power of the laser, $\mathcal{F}$ is the finesses of Fabry-Pérot cavities, f_{c} is the cavity pole, and l_{bar} is the length of the bar (or the distance of the measurement points). These two noise contributions cannot be reduced simultaneously, and their lower bound is expressed as:

$$\sqrt{S_{\mathrm{QN}}(f)} \geq \theta_{\mathrm{SQL}}. \tag{2.41}$$

2.4.3 Seismic noise

The vibration of the ground, or the suspension point of the pendulum, can be transferred to the rotation of the suspended bar through the suspension wires. There are two approaches to reducing seismic noise: passive and active. The passive approach involves reducing the coupling or transfer function of the vibration by suspending the mass. The active approach reduces the vibration directly using feedback control. In TOBA, seismic noise can couple to the rotational motion of the torsion pendulum in several ways. Below, we briefly introduce each type of coupling, and the methods used to suppress them.

Rotational seismic noise

Rotational seismic noise can be reduced passively by using multiple suspension stages. The transfer function from rotational seismic noise to the rotation of a single suspended torsion pendulum is given by

$$H_{\mathrm{rot}}(f) = \frac{\tilde{\theta}(f)}{\tilde{\theta}_{\mathrm{g}}(f)} = \frac{f_0^2}{f_0^2(1 + i\phi) - f^2}, \tag{2.42}$$

where f_0 is the resonant frequency of the torsion pendulum and ϕ is the loss angle of the rotational spring constant. The seismic noise is isolated above the resonant frequency in proportion to f^{-2}. Further isolation can be achieved by increasing the number of stages in the suspension. In general, an n-stage torsion pendulum can isolate the seismic noise above the resonant frequency in proportion to f^{-2n}. This technique is similar to the method used in ground-based GW detectors for isolating translational seismic noise.

If the two pendulums are suspended in the same way and their locations are sufficiently close to each other, they will experience the same vibration from the seismic noise. Therefore, when the bar orientation is crossed, further noise reduction can be achieved by taking the differential motion of the two pendulums, because the response of each bar to gravity gradients is sign-flipped as mentioned in Section 2.1.2, while the seismic noise is common. This technique for reducing common noise is called the common-mode rejection technique, and the extent to which the common-mode noise is reduced is expressed by the common-mode rejection ratio (CMRR) C_{CMRR} (a smaller value is better).

By utilizing these two techniques, the seismic noise from the rotational seismic noise is given by

$$\sqrt{S_{\mathrm{seis,rot}}(f)} = C_{\mathrm{CMRR}}|H_{\mathrm{rot}}(f)|\sqrt{S_{\mathrm{g,rot}}(f)}, \tag{2.43}$$

where $\sqrt{S_{\mathrm{g,rot}}(f)}$ is the ASD of the rotational seismic noise.

Translational seismic cross-coupling noise

Translational seismic noise is ideally not transferred to the horizontal rotation of the bar. However, asymmetries in the system can create routes for such cross-coupling transfers. This noise tends to be more significant than rotational seismic noise. Many of the cross-coupling routes were identified in [90]. According to [90], most of these sources are caused by tilts in the system, such as the tilt of the bar and the non-parallel alignment of the two mirrors attached at both ends of the bar. The important cross-coupling routes are shown in Fig. 2.5.

The noise spectra for these routes are expressed in the following form:

$$\sqrt{S_{\mathrm{seis,trans}}(f)} = \left(\phi_{\mathrm{R}}|H_{\mathrm{P}}(f)| + \phi_{\mathrm{P}}|H_{\mathrm{R}}(f)| + \frac{\phi_{\mathrm{mir}}}{D_{\mathrm{mir}}}C_{\mathrm{CMRR}}|H_{\mathrm{mir}}(f)|\right)\sqrt{S_{\mathrm{g,trans}}(f)}, \tag{2.44}$$

where ϕ_{R} and ϕ_{P} represent the tilt of the bar in the Roll and Pitch directions, as illustrated in Fig. 2.5 (a) and (b), respectively. Pitch, Roll and Yaw correspond to the rotations around the x-, y- and z-axes, respectively (as defined in Fig. 1). ϕ_{mir} is the tilt of the two mirrors, and D_{mir} is the distance between the two mirrors, as shown in Fig. 2.5 (c). C_{CMRR} is the CMRR for the translational mode. $H_{\mathrm{P}}(f)$, $H_{\mathrm{R}}(f)$, and $H_{\mathrm{mir}}(f)$ denote the transfer functions from the translational seismic noise, and $\sqrt{S_{\mathrm{g,trans}}(f)}$ is the ASD of the

translational seismic noise. $H_{\mathrm{P}}(f)$, $H_{\mathrm{R}}(f)$, and $H_{\mathrm{mir}}(f)$ are expressed as follows:

$$H_{\mathrm{P}}(f) = \left(\frac{I_{\mathrm{P}}}{I_{\mathrm{Y}}}\frac{\delta x}{\delta z} - \phi_{\mathrm{R}}\right)\left(\frac{4\pi^2 f^4}{g f_{\mathrm{Y}}^2}\right)\left(1-\frac{f^2}{f_{\mathrm{Y}}^2}\right)^{-1}\left(1-\frac{f^2}{f_{\mathrm{T}}^2}\right)^{-1}\left(1-\frac{f^2}{f_{\mathrm{P}}^2}\right)^{-1}, \tag{2.45}$$

$$H_{\mathrm{R}}(f) = \left(\frac{I_{\mathrm{R}}}{I_{\mathrm{Y}}}\frac{\delta y}{\delta z} - \phi_{\mathrm{P}}\right)\left(\frac{4\pi^2 f^4}{g f_{\mathrm{Y}}^2}\right)\left(1-\frac{f^2}{f_{\mathrm{Y}}^2}\right)^{-1}\left(1-\frac{f^2}{f_{\mathrm{T}}^2}\right)^{-1}\left(1-\frac{f^2}{f_{\mathrm{R}}^2}\right)^{-1}, \tag{2.46}$$

$$H_{\mathrm{mir}}(f) = \left(1-\frac{l+\delta z}{g}(2\pi f)^2\right)^{-1}, \tag{2.47}$$

where $I_{\mathrm{P(R,Y)}}$ denotes the moment of inertia of the TM in Pitch, Roll, and Yaw, respectively, $f_{\mathrm{P(R,Y,T)}}$ represents the resonant frequencies in Pitch, Roll, Yaw, and translational modes, respectively, $\delta x, \delta y, \delta z$ are the displacements between the suspension point and the center of mass, and l is the length of the wire.

Regarding Eq. (2.45) and Eq. (2.46), generally $\phi_{\mathrm{R}} \simeq \delta x/\delta z$ and $\phi_{\mathrm{P}} \simeq \delta y/\delta z$ hold true. However, even if the suspension point is successfully aligned directly above the center of mass, setting δx and δy to zero, it should be noted that ϕ_{R} and ϕ_{P} may not become zero if the mass distribution of the TM is not uniform. Due to the high symmetry of the TM around the x-axis ($I_{\mathrm{R}} \simeq I_{\mathrm{Y}}$), H_{R} is generally orders of magnitude smaller than H_{P}. In addition to suppressing translational seismic noise, reducing the system's tilt is an effective way to mitigate the noise. The tilt can be adjusted using balance weights, actuators, and similar mechanisms. Furthermore, when detecting the differential rotation between the two TMs, as the rotational resonant frequencies of the two bars become closer, the shapes of the transfer function become more similar, improving common-mode rejection, which leads to reduce cross-coupling noise.

For the third route in Eq. (2.44), reducing noise can be effectively achieved by polishing the surface of the TM and applying a direct coating to improve parallelism, instead of attaching two separate mirrors. Additionally, improving the CMRR in the translational direction of the two TMs is also effective. To achieve this, it is sufficient to align the heights of the centers of mass of the two TMs.

Nonlinear coupling

Recently, it has been found that translational seismic noise can be transferred to the rotational motion of the pendulum nonlinearly, and their contribution is not negligible for TOBA [91]. Following [91], the nonlinear term of the Fourier spectrum of the rotational motion $\tilde{\theta}_{\mathrm{Y}}(f)$ is given by

$$\begin{aligned}\tilde{\theta}_{\mathrm{Y}}(f) = |\chi(f)|\Big[&(I_{\mathrm{R}}-I_{\mathrm{Y}})\tilde{\theta}_{\mathrm{P}}(f) * \Big(\omega^2\tilde{\theta}_{\mathrm{R}}(f)\Big) + (I_{\mathrm{Y}}-I_{\mathrm{P}})\Big(\omega^2\tilde{\theta}_{\mathrm{P}}(f)\Big) * \tilde{\theta}_{\mathrm{R}}(f)\\ &- (I_{\mathrm{P}}-I_{\mathrm{R}})(\omega\tilde{\theta}_{\mathrm{P}}(f)) * (\omega\tilde{\theta}_{\mathrm{R}}(f))\\ &+Mh\Big\{\Big(\omega^2\tilde{x}(f)\Big) * \tilde{\theta}_{\mathrm{P}}(f) + \Big(\omega^2\tilde{y}(f)\Big) * \tilde{\theta}_{\mathrm{R}}(f)\Big\}\Big].\end{aligned} \tag{2.48}$$

Here, $\tilde{x}(f)$, $\tilde{y}(f)$, $\tilde{\theta}_{\mathrm{P}}(f)$, and $\tilde{\theta}_{\mathrm{R}}(f)$ represent the Fourier spectra of the motion in the x, y, Pitch, and Roll directions, respectively. h is the vertical distance between the center of

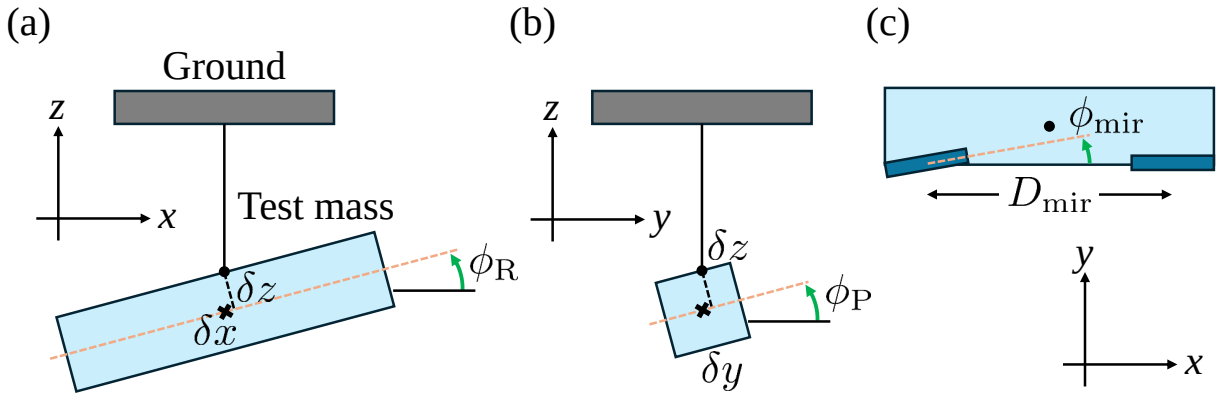

Figure 2.5: Routes of translational seismic cross-coupling noise caused by: (a) the bar's tilt in the Roll direction, (b) the bar's tilt in the Pitch direction, and (c) the non-parallel alignment of the two mirrors.

mass of the pendulum and its suspension point, M is the mass of the bar, and $\omega_x = 2\pi f_x$, $\omega_y = 2\pi f_y$ are the resonant frequencies in the x and y directions, respectively.

Suppose that the resonant frequencies in the x and y directions are around 1 Hz and are very close to each other. Then, according to Eq. (2.48), it can be approximated as

$$\sqrt{S_{\mathrm{seis,nonlin}}(f)} \simeq (2\pi \times 1\,\mathrm{Hz})^4 S_{\mathrm{g,trans}}(1\,\mathrm{Hz})|\chi(f)|\frac{Mh}{g} \times \sqrt{\frac{\pi Q f_{\mathrm{ave}}^5}{(f-|f_x-f_y|)^2}\left(\frac{1}{(f-2f_{\mathrm{ave}})^2}+\frac{1}{(f+2f_{\mathrm{ave}})^2}\right)}. \tag{2.49}$$

where $f_{\mathrm{ave}} = (f_x + f_y)/2$ is the average of f_x and f_y. Here, we assume that $f_x, f_y \simeq 1\,\mathrm{Hz}$. Eq. (2.49) implies that the ASD of the nonlinear seismic noise depends on the square of the translational seismic noise around $f_{\mathrm{ave}} \sim 1\,\mathrm{Hz}$.

Therefore, one of the most effective ways to reduce the nonlinear seismic noise is to suppress translational seismic noise around 1 Hz by passive isolation or active feedback. Damping the resonant modes and decreasing their Q factors is also effective for reducing the nonlinear noise, as the dominant contribution to the noise comes from the convolution around the resonant frequencies of each DoF.

2.4.4 Residual gas noise

Residual gas molecules in the vacuum move randomly and sometimes strike the bar, causing damping or excitation of the bar's oscillation. The distribution of the gas states can be predicted using the kinetic theory of gases. The noise contribution from residual gas to a rectangular cuboid bar with surface area A is given by

$$\sqrt{S_{\mathrm{gas}}(f)} = \sqrt{\frac{P_{\mathrm{vac}} A l_{\mathrm{bar}}^2 \sqrt{m_{\mathrm{mol}} k_{\mathrm{B}} T}}{3\sqrt{2\pi}}}|\chi(f)|, \tag{2.50}$$

where P_{vac} is the pressure around the bar, and m_{mol} is the mass of the residual gas molecules.

Reducing the residual gas noise requires improving the vacuum level, P_{vac}. Cooling the environment around the bar, T, also helps reduce noise, but the direct dependency is relatively small ($\propto T^{1/4}$). Instead, cooling leads to the adsorption of gas molecules onto the surface, which improves the vacuum level through a process known as cryopumping.

2.4.5 Magnetic noise

Fluctuations in the ambient magnetic field can couple to the rotation of the bar through torque noise. This noise is associated with either the magnetic dipole moment $\boldsymbol{\mu}$ of the bar or its magnetic susceptibility χ_{m}.

The torque induced by a magnetic field $\boldsymbol{B}$ is given by

$$\boldsymbol{N} = \boldsymbol{\mu} \times \boldsymbol{B}. \tag{2.51}$$

Fluctuation in time of this directly acts as a torque noise for the torsion pendulum and ASD is given by

$$\sqrt{S_{\mathrm{mag},\mu}(f)} = \mu |\chi(f)| \sqrt{S_{\mathrm{mag},\perp}(f)}, \tag{2.52}$$

where $\sqrt{S_{\mathrm{mag},\perp}(f)}$ is the ASD of the magnetic field perpendicular to $\boldsymbol{\mu}$.

Another type of magnetic noise arises from magnetic field gradients. The force caused by the magnetic gradient is expressed as

$$\boldsymbol{F} = \nabla \left(\left(\mu + \frac{\chi_{\mathrm{m}} V \boldsymbol{B}}{\mu_0} \right) \cdot \boldsymbol{B} \right), \tag{2.53}$$

where V is the volume of the magnetized region, and μ_0 is the permeability of free space.

Recently, it has been reported that magnetic dipole moments induced by eddy currents in the bar exhibit stronger coupling to the magnetic field at cryogenic temperatures compared to room temperature. The induced magnetic dipole moment is given by

$$\mu_{\mathrm{ind}}(f) = 2\pi f C_{\mathrm{shape}} \sigma(T) B(f), \tag{2.54}$$

where C_{shape}, with units of m^3, is a factor depending on the shape of the bar, and $\sigma(T)$ is the electric conductivity of the bar at temperature T. This induced moment couples to the direct current (DC) magnetic field B_{geo} and exerts a torque $N = \mu_{\mathrm{ind}} B_{\mathrm{geo}}$ on the bar. Therefore, the magnetic noise from the induced moment is given by

$$\sqrt{S_{\mathrm{mag,ind}}(f)} = 2\pi f C_{\mathrm{shape}} \sigma(T) B_{\mathrm{geo}} |\chi(f)| \sqrt{S_{\mathrm{mag}}}. \tag{2.55}$$

For conductors or metals, the electric conductivity is generally lower at cryogenic temperatures. Furthermore, materials with good thermal conductivity also tend to have good electric conductivity at low temperatures. Therefore, this noise is problematic for experiments at cryogenic temperatures.

One way to reduce these magnetic noises is to suppress B using magnetic shields. Ferromagnetic materials or superconductors can serve as effective shields for the ambient magnetic field. It has been reported that a magnetic shield made of high-temperature superconductors such as Bi-Sr-Ca-Cu-O_x can suppress magnetic field fluctuations by more than six orders of magnitude at 0.2 Hz [92].

To reduce magnetic noise from induced currents, changing the material of the bar from metals to insulators or semiconductors is also effective. Unlike metals, insulators and semiconductors have lower electric conductivity at low temperatures than at room temperature [93]. In particular, silicon is widely used in cryogenic experiments, and its characteristics are well-known.

2.4.6 Laser frequency noise

If we measure the motion of the bars using laser interferometers, the noise from the laser sources themselves is also transferred to the measurement signals. Here, we assume that the rotational motion is measured with two Fabry-Pérot cavities at both ends of the bar. In principle, the fluctuation of the laser frequency cannot be distinguished from the displacement of the bar, which corresponds to one of the mirrors forming the Fabry-Pérot cavity. The coupling between frequency noise $\delta\nu$ and the rotational signal $\delta\theta$ is given by

$$\frac{\delta\theta}{\delta\nu} = \frac{l_{\rm cav}}{D\nu_0}, \tag{2.56}$$

where $l_{\rm cav}$ is the length of the cavity, D is the distance between two cavities, and ν_0 is the frequency of the laser. If the incident beam is split and injected into each cavity, the coupling of frequency noise can be reduced using the common-mode rejection technique. This is because the rotational signal is opposite in phase for each cavity as discussed in Section 2.1.2, while the frequency noise is common. Thus, the frequency noise is given by

$$\sqrt{S_{\rm freq}(f)} = \frac{l_{\rm cav}}{D\nu_0} C_{\rm CMRR} \sqrt{S_\nu(f)}, \tag{2.57}$$

where $C_{\rm CMRR}$ is the common-mode rejection ratio, and $\sqrt{S_\nu(f)}$ is the frequency noise of the laser source. According to Eq. (2.57), in addition to suppressing the frequency noise of the laser source itself through feedback control, reducing the cavity length and increasing the distance between the cavities are effective methods for mitigating frequency noise.

2.5 Previous prototypes

2.5.1 Development roadmap of TOBA

To realize Final TOBA, we have been developing small-scale (20 cm–35 cm) prototypes to address technical challenges. The development roadmap for TOBA is summarized in Fig. 2.6. In the following sections, we introduce the configurations and results of Phase-I

TOBA, Phase-II TOBA, SWIM$\mu\nu$, and research on seismic noise. We consider Phase-III TOBA to be just one step before Final TOBA, with a configuration closer to Final TOBA than previous prototypes. Details of Phase-III TOBA are described in Section 2.6.

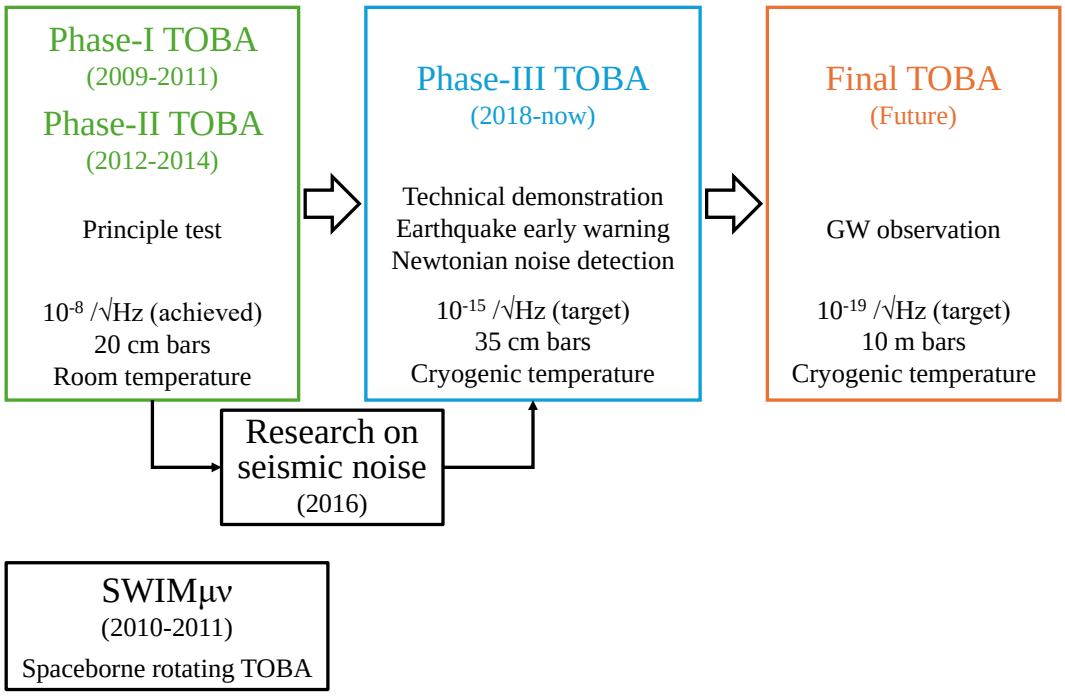

Figure 2.6: Development roadmap of TOBA.

2.5.2 Phase-I TOBA

The first prototype named Phase-I TOBA was built around 2012 to 2014. The superconducting material at the top is cooled, and the neodymium magnets are supported by superconducting magnetic levitation. This allowed the resonant frequency to be lowered to 5 mHz and reduced thermal noise from the suspension. The TM with the length of 20 cm was made of aluminum. The rotation of the TM was measured with a Michelson interferometer.

A sensitivity of 1×10^{-8} $/\sqrt{\text{Hz}}$ was achieved at 0.1 Hz as shown in Fig. 2.7. Below 0.1 Hz, magnetic noise limits the sensitivity. The cause of this magnetic noise is the torque on the TM due to fluctuations in the external magnetic field. Above 0.1 Hz, seismic noise limits the sensitivity. The two mirrors of the Michelson interferometer are not aligned parallel, causing the coupling noise from translational seismic noise.

Phase-I TOBA set an upper limit for the stochastic GW background at $\Omega_{\text{GW}}(f = 0.2\,\text{Hz}) < 4.3 \times 10^{17}$ [69]. Furthermore, a pair of TOBAs in Tokyo and Kyoto conducted simultaneous 7-hour observations and set an upper limit on the stochastic GW background to $\Omega_{\text{GW}h_0^2} < 1.9 \times 10^{17}$ at 0.035 Hz–0.830 Hz [94].

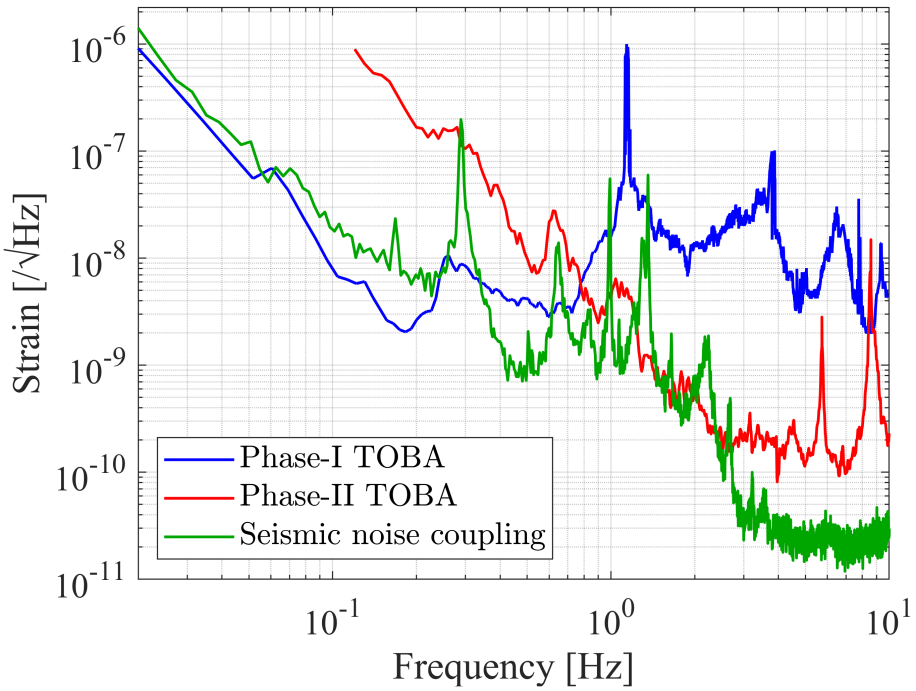

Figure 2.7: Achieved sensitivities of the prototype TOBAs. The blue, red, and green lines represent the sensitivity of Phase-I TOBA [69], Phase-II TOBA [62], and research on seismic noise coupling [95], respectively.

2.5.3 Phase-II TOBA

The second prototype Phase-II TOBA was built around 2016. Since the sensitivity of Phase-I TOBA below 0.1 Hz was limited by magnetic field noise, Phase-II TOBA adopted tungsten for the suspension wires. An optical bench (OB) was suspended, and active vibration isolation was applied at the suspension points. The TM with the length of 24 cm was made of aluminum. Laser was directed into the OB via optical fibers, and the rotation of the TM was measured using a Michelson interferometer. Furthermore, Phase-II TOBA introduced two additional outputs by measuring the rotation of the bars on the vertical planes other than on the horizontal plane. This methos increases event detection rates and parameter resolution [96].

A sensitivity of 1×10^{-10} $/\sqrt{\mathrm{Hz}}$ was achieved at 3 Hz as shown in Fig. 2.7 [62]. The sensitivity is limited by the phase noise of the Michelson interferometer. The cause of this phase noise is thought to be the vibration noise of the fiber beam splitter.

Phase-II TOBA set the upper limits on the stochastic GW background as follows: $h_0^2\Omega_{\mathrm{GW}}(f = 2.58\,\mathrm{Hz}) < 6.0 \times 10^{18}$ (frequentist), $h_0^2\Omega_{\mathrm{GW}}(f = 2.58\,\mathrm{Hz}) < 1.2 \times 10^{20}$ (Bayesian) [97]. It also provided a constraint that a intermediate-mass black hole binary merger with a mass of 200 $M_\odot$ does not exist within 1.2×10^{-4} pc [98].

2.5.4 SWIM$\mu\nu$

Spaceborne experiment of TOBA named SWIM$\mu\nu$ (SpaceWire Interface demonstration Module $\mu\nu$) was performed from 2010 to 2011 [70]. This was the first GW experiment in space. The satellite contained a small bar with the mass of 50 g made of aluminum and its motion was measured with photo-reflective displacement sensors. The bar and the housing satellite rotated at $f_{\rm rot} = 46.5\,{\rm mHz}$ to up-convert the low-frequency GW signal to around the rotational frequency. This method was used to improve the signal-to-noise ratio (SNR) when the noise spectrum has steeper frequency dependence than f^{-2} between the target frequency and $f_{\rm rot}$. In addition, the rotating configuration is directly sensitive to circular polarizations of GWs defined as $h_{\rm FW(RE)} = (h_+ \pm ih_\times)/\sqrt{2}$ [4]. Two GW polarizations at $f_{\rm GW}$ appears separately at $f_{\rm rot} + f_{\rm GW}$ and $f_{\rm rot} - f_{\rm GW}$.

The observation data was recorded for six hours. SWIM$\mu\nu$ set upper limits of $\Omega_{\rm GW}^{\rm FW} < 1.7 \times 10^{31}$ and $\Omega_{\rm GW}^{\rm RE} < 3.1 \times 10^{30}$ for two circular polarizations of the stochastic GW background.

2.5.5 Research on seismic noise coupling

An experimental demonstration was conducted to investigate the way of reducing the translational seismic noise coupling in 2016 [95]. A single TM bar with the length of 20 cm was suspended with double-stage pendulum. The TM was made of fused silica with an optical coating on the surface. The surface at both end of the TM was used as two mirrors and the rotation of the bar was measured with a Michelson interferometer. The method of coating directly on the bar reduced the relative tilt between the mirrors surface, which was the main cause of the seismic noise coupling in Phase-I TOBA.

A sensitivity of $1 \times 10^{-9}\ /\sqrt{\rm Hz}$ was achieved at 0.5 Hz as shown in Fig. 2.7 [95]. Though the achieved cross-coupling transfer function of $5 \times 10^{-6}\,{\rm rad/m}$ at 0.1 Hz [90] is insufficient for the future sensitivity of TOBA, this work successfully tested the model of the coupling of the seismic noise and established the basic strategy to reduce the coupling by tuning the tilt angle of the bar with balance weights and actuators.

2.6 Phase-III TOBA

Currently, the development of the third prototype, Phase-III TOBA, is underway. The goal is to reduce the noise to $1 \times 10^{-15}\ /\sqrt{\rm Hz}$ at 0.1 Hz using 35 cm TMs. This noise level will achieve the target sensitivity of Final TOBA, $1 \times 10^{-19}\ /\sqrt{\rm Hz}$, by scaling up to 10 m. Various components have been developed, and demonstrations are progressing.

[4] The sign is determined such that the direction of the bar's rotation coincides with the rotation direction (forward mode) for $h_{\rm FW}$, and is opposite to the rotation direction (reverse mode) for $h_{\rm RE}$.

2.6.1 Overview of experimental setup

The configuration and picture of Phase-III TOBA are shown in Fig. 2.8. The system of Phase-III TOBA is composed of four main components: optical system, suspension system, cryogenic system, and vibration isolation system. The optical system measures the horizontal rotation of the TMs, while the other three components are dedicated to noise reduction.

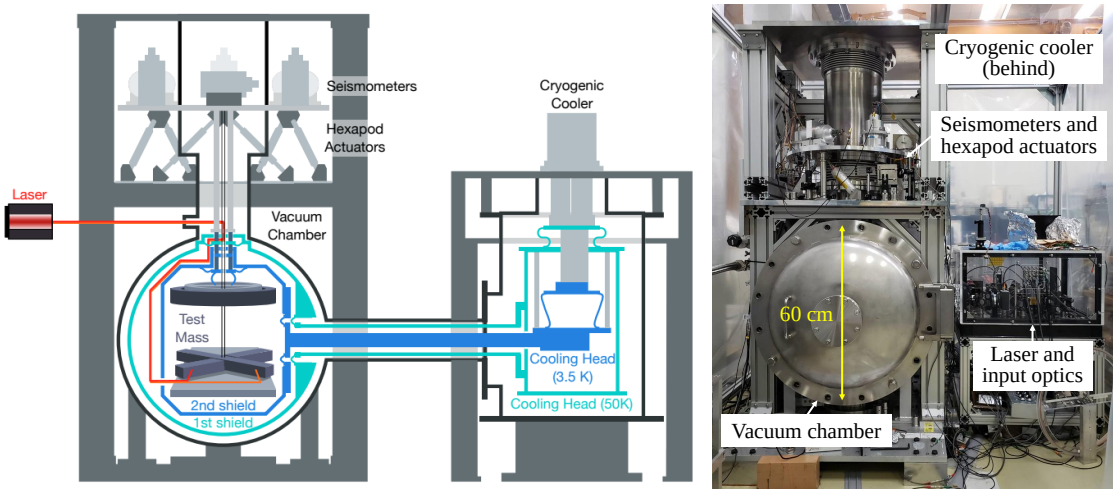

Figure 2.8: Configuration (left) and picture (right) of Phase-III TOBA. The left figure is taken from [71].

Optical system

The optical system is used to read the horizontal rotation of the TM. For the laser interferometer configuration, trade-off studies and proof-of-concept experiments such as improved wavefront sensors mentioned in Section 2.6.3 were conducted extensively. As a result, a configuration was finalized in which two Fabry-Pérot cavities are formed at both ends of the TM, and rotation is detected from the differential lengths. The TM is made of silicon with an optical coating applied to its surface. Coating the bar directly helps reduce the relative tilt between mirror surfaces and minimizes translational seismic cross-coupling noise.

Suspension system

The suspension system consists of a double-stage pendulum, providing passive vibration isolation for the TMs.

Two TM bars, each 35 cm in length, are independently suspended from an intermediate mass (IM). The horizontal rotations of the two TMs are excited in opposite directions in response to gravity gradients, allowing for the reduction of common noise as discussed in Section 2.1.2. This differential rotation is measured using the optical system mounted on an OB. The TM bars are made of silicon, chosen for its excellent optical properties at

cryogenic temperatures and its low mechanical loss. Each TM is suspended from the IM by a wire made of silicon or sapphire.

The IM itself is suspended by a wire made of copper beryllium or tungsten from the active vibration isolation stage. The OB is also suspended from the IM. Both the IM and the OB are made of oxygen-free copper, since it has high thermal conductivity at cryogenic temperature and helps effective heat extraction. To further enhance radiative cooling, the surfaces of the masses are oxidized.

Cryogenic system

The cryogenic system is used to cool the TMs and suspension wires, reducing thermal noise. The target temperature for Phase-III TOBA is 4 K, and it is necessary to cool the pendulum within an acceptable time scale. However, torsion pendulums are highly sensitive to small forces, and we should avoid attaching additional components to the pendulums. Furthermore, any additional vibration noise introduced by the cooling system must be minimized. Meeting these two requirements simultaneously is a serious issue.

The cooling system consists of a pulse tube refrigerator and two layers of radiation shields. The radiation shields are connected to the cryocooler and cooled to 50 K (first shield) and 3.5 K (second shield), respectively. In addition, to enhance conductive cooling, heat-links made of high-purity aluminum wires are attached between the second radiation shield and the IM, as well as between the IM and the OB.

Vibration isolation system

The active vibration isolation system is implemented to suppress vibration noise. In general, seismic noise is significant at low frequencies and represents a dominant noise source for TOBA. To address this, we install an active vibration isolation system in addition to the passive isolation by suspending the masses using a double-stage pendulum.

Seismometers are placed on top of the vacuum chamber to monitor vibrations in all degrees of freedom. These seismometers provide feedback signals to hexapod actuators for control. The hexapod actuators are composed of six piezoelectric actuators, and enable to control the stage in all directions, translation along three axes and rotation around three axes.

In addition, we also need vibration isolation from the cryocooler. The heat-links on the IM are not directly connected to the second shield. Instead, they are connected to the second shield via the active vibration isolation stage. This configuration allows the system to reduce not only seismic noise but also vibrations transmitted from the cryocooler to the suspended masses through the heat-links.

2.6.2 Design sensitivity and noise sources

The design sensitivity of Phase-III TOBA is shown in Fig. 2.9. The target sensitivity at 0.1 Hz is 1×10^{-15} $/\sqrt{\text{Hz}}$. At frequencies below 0.2 Hz, the sensitivity is primarily limited by seismic noise and suspension thermal noise. Above 0.2 Hz, quantum shot noise

becomes the dominant factor. The design parameters of Phase-III required to achieve the target sensitivity are summarized in Table 2.3. The noise sources for Phase-III TOBA are calculated as follows. The design sensitivity in Fig. 2.9 is plotted in strain with the unit $/\sqrt{\text{Hz}}$, while the calculations in Eq. (2.60)–Eq. (2.70) use the unit $\text{rad}/\sqrt{\text{Hz}}$. To convert rotational sensitivity in $\text{rad}/\sqrt{\text{Hz}}$ to strain sensitivity in $/\sqrt{\text{Hz}}$, divide it by the TOBA response function defined in Eq. (2.23), substituting $f_0 = 7.7\,\text{mHz}$ and $\phi = 10^{-8}$.

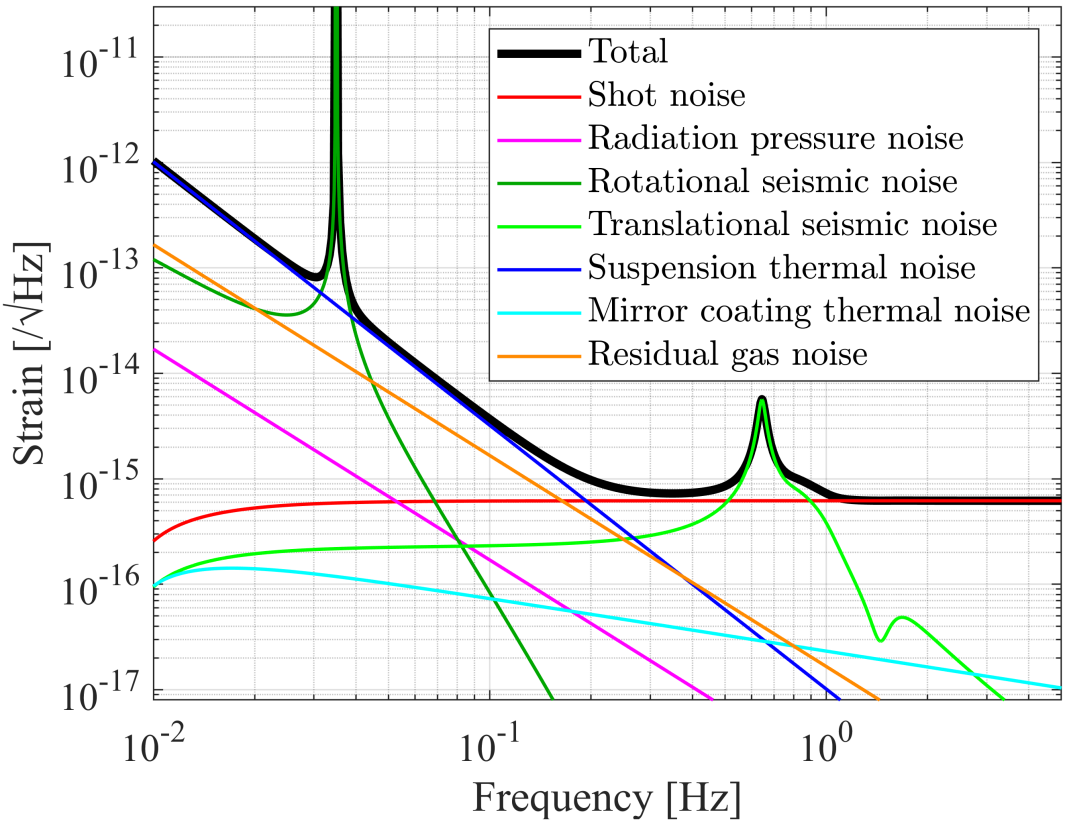

Figure 2.9: Design sensitivity of Phase-III TOBA. The black line represents the total sensitivity, and other colored lines show the noise budget.

Suspension thermal noise

Here, we assume the suspension wire is made of silicon, as summarized in Table 2.3. Using these parameters, we calculate:

$$\kappa = 2.3 \times 10^{-5}\,\text{N m/rad}, \tag{2.58}$$

$$f_0 = \frac{1}{2\pi}\sqrt{\frac{\kappa}{I}} = 7.7\,\text{mHz}. \tag{2.59}$$

From Eq. (2.26),

$$\sqrt{S_{\text{th,sus}}(f)} \simeq 1.6 \times 10^{-16}\left(\frac{T}{4\,\text{K}}\right)^{\frac{1}{2}}\left(\frac{\phi_{\text{wire}}}{1\times10^{-8}}\right)^{\frac{1}{2}}\left(\frac{f}{0.1\,\text{Hz}}\right)^{-\frac{5}{2}}\ \text{rad}/\sqrt{\text{Hz}}. \tag{2.60}$$

Table 2.3: Design parameters of Phase-III TOBA.

Parameter	Value
Optical system	
Wavelength of laser	1550 nm
Power of laser	1 mW
Beam spot size	350 μm
Finesse of Fabry-Pérot cavity	50
Distance between two Fabry-Pérot cavities	200 mm
Loss angle of mirror substrate	1×10^{-8}
Loss angle of mirror coating	5×10^{-4}
Suspension system	
Material of TM	Silicon
Shape and size of TM	Rectangular, $350 \times 40 \times 40\,\mathrm{mm}^3$
Mass of TM	0.98 kg
Moment of inertia of TM	$0.010\,\mathrm{kg\,m}^2$
Loss angle of TM	1×10^{-8}
Material of wire	Silicon
Length of wire	160 mm
Diameter of wire	0.15 mm
Loss angle of wire	1×10^{-8}
Torsional resonant frequency of TM	7.7 mHz
Torsional resonant frequency of IM	3.2 mHz
Cryogenic system	
Temperature	4 K
Vibration isolation system	
Rotational vibration	5×10^{-11} rad/$\sqrt{\mathrm{Hz}}$ at 0.1 Hz
CMRR for rotational motion	1×10^{-3}
Translational vibration	1×10^{-7} m/$\sqrt{\mathrm{Hz}}$ at 0.1 Hz
Tilt angle of TM	1×10^{-8} rad
Others	
Residual gas pressure	1×10^{-7} Pa

Bar thermal noise

We assume the bar shape as $350 \times 40 \times 40\,\mathrm{mm}^3$ rectangular shape, and the bar is made of silicon as summarized in Table 2.3. From Eq. (2.30) the second eigenfrequency is $\sim 4\,\mathrm{kHz}$. Assuming the bar thermal noise is given from Eq. (2.31) by

$$\sqrt{S_{\mathrm{th,bar}}(f)} \simeq 6.6 \times 10^{-17} \left(\frac{T}{4\,\mathrm{K}}\right)^{\frac{1}{2}} \left(\frac{\phi_{\mathrm{bar}}}{1 \times 10^{-8}}\right)^{\frac{1}{2}} \left(\frac{f}{0.1\,\mathrm{Hz}}\right)^{-\frac{5}{2}} \mathrm{rad}/\sqrt{\mathrm{Hz}}. \tag{2.61}$$

Mirror thermal noise

Assuming the substrate of the mirror is made of silicon and the coating is composed of a silica-tantala layer, we also consider the beam spot size $w_0 = 350\,\mu\mathrm{m}$ and the distance between the two Fabry-Pérot cavities $D = 200\,\mathrm{mm}$. The averaged properties of silica and tantala are used as the effective properties of the coating. From Eq. (2.32), we calculate the substrate and coating thermal noise of the mirror as follows:

$$\begin{aligned}&\sqrt{S_{\mathrm{th,mir(sub)}}(f)}\\ &\simeq 8.2 \times 10^{-19} \left(\frac{T}{4\,\mathrm{K}}\right)^{\frac{1}{2}} \left(\frac{\phi_{\mathrm{sub}}}{1 \times 10^{-8}}\right)^{\frac{1}{2}} \left(\frac{w_0}{350\,\mu\mathrm{m}}\right)^{-\frac{1}{2}} \left(\frac{D}{200\,\mathrm{mm}}\right)^{-1} \left(\frac{f}{0.1\,\mathrm{Hz}}\right)^{-\frac{5}{2}} \mathrm{rad}/\sqrt{\mathrm{Hz}},\end{aligned} \tag{2.62}$$

$$\begin{aligned}&\sqrt{S_{\mathrm{th,mir(coat)}}(f)}\\ &\simeq 3.7 \times 10^{-17} \left(\frac{T}{4\,\mathrm{K}}\right)^{\frac{1}{2}} \left(\frac{\phi_{\mathrm{coat}}}{5 \times 10^{-4}}\right)^{\frac{1}{2}} \left(\frac{w_0}{350\,\mu\mathrm{m}}\right)^{-\frac{1}{2}} \left(\frac{D}{200\,\mathrm{mm}}\right)^{-1} \left(\frac{f}{0.1\,\mathrm{Hz}}\right)^{-\frac{5}{2}} \mathrm{rad}/\sqrt{\mathrm{Hz}},\end{aligned} \tag{2.63}$$

Therefore, the contribution from the coating is dominant for the mirror thermal noise.

Quantum noise

We assume the optical parameters as summarized in Table 2.3. The shot noise is calculated by Eq. (2.38) as follow:

$$\sqrt{S_{\mathrm{shot}}(f)} \simeq 3.1 \times 10^{-16} \left(\frac{P_0}{1\,\mathrm{mW}}\right)^{-\frac{1}{2}} \left(\frac{\mathcal{F}}{50}\right)^{-1} \left(\frac{D}{200\,\mathrm{mm}}\right)^{-1} \mathrm{rad}/\sqrt{\mathrm{Hz}}. \tag{2.64}$$

The radiation pressure noise is given by Eq. (2.39) as follow:

$$\sqrt{S_{\mathrm{RP}}(f)} \simeq 8.5 \times 10^{-17} \left(\frac{P_0}{1\,\mathrm{mW}}\right)^{\frac{1}{2}} \left(\frac{\mathcal{F}}{50}\right) \left(\frac{D}{200\,\mathrm{mm}}\right) \left(\frac{f}{0.1\,\mathrm{Hz}}\right)^{-2} \mathrm{rad}/\sqrt{\mathrm{Hz}}. \tag{2.65}$$

The contribution from the radiation pressure noise is negligible compared to other noises, while the shot noise is dominant above $\sim 0.2\,\mathrm{Hz}$.

Rotational seismic noise

From the parameters of the TMs suspended by a double-stage pendulum, the transfer function Eq. (2.42) above 0.1 Hz is approximated to

$$H_{\rm rot}(f) \simeq 8.4 \times 10^{-4} \left(\frac{f}{0.1\,\mathrm{Hz}} \right)^{-4}. \tag{2.66}$$

There is no measurement data about the rotational seismic noise. Here we assume the value to be

$$\sqrt{S_{\rm g,rot}} = \frac{1 \times 10^{-10}\ \mathrm{rad}/\sqrt{\mathrm{Hz}}}{1 + (f/0.1\,\mathrm{Hz})^2}. \tag{2.67}$$

Also we assume that the CMRR is $C_{\rm CMRR} \simeq 1 \times 10^{-3}$. Therefore, we calculate from Eq. (2.43)

$$\sqrt{S_{\rm seis,rot}(f)} \simeq 4.2 \times 10^{-17} \left(\frac{C_{\rm CMRR}}{1 \times 10^{-3}} \right) \left(\frac{f}{0.1\,\mathrm{Hz}} \right)^{-4} \mathrm{rad}/\sqrt{\mathrm{Hz}}. \tag{2.68}$$

Translational seismic cross-coupling noise

In Phase-III TOBA, the TM is directly coated with an optical layer on its surface to reduce the relative tilt between mirror surfaces. Therefore, the third term in Eq. (2.44) is negligible and we calculate only the first and second terms. We assume the tilt angles $\phi_{\rm P}$ and $\phi_{\rm R}$ is suppressed below $< 1 \times 10^{-8}$. The translational vibration at suspension stage is below 1×10^{-7} m$/\sqrt{\mathrm{Hz}}$ at 0.1 Hz by feedback control, and this corresponds to a suppression ratio of $\sim 1/100$. From Eq. (2.44),

$$\sqrt{S_{\rm seis,trans}(f)} \simeq 4.1 \times 10^{-17} \left(\frac{\phi_{\rm P(R)}}{1 \times 10^{-8}} \right) \left(\frac{\sqrt{S_{\rm g,trans}}}{1 \times 10^{-7}\ \mathrm{m}/\sqrt{\mathrm{Hz}}} \right) \mathrm{rad}/\sqrt{\mathrm{Hz}}. \tag{2.69}$$

Residual gas noise

The vacuum level is required to be evacuated down to 1×10^{-7} Pa, utilizing the cryopump. We assume that the residual gas consists of water molecules. From Eq. (2.50) we get

$$\sqrt{S_{\rm gas}(f)} \simeq 1.6 \times 10^{-16} \left(\frac{P_{\rm vac}}{1 \times 10^{-7}\,\mathrm{Pa}} \right)^{\frac{1}{2}} \left(\frac{T}{4\,\mathrm{K}} \right)^{\frac{1}{4}} \mathrm{rad}/\sqrt{\mathrm{Hz}}. \tag{2.70}$$

2.6.3 Previous results

Optical system

The cryogenic monolithic interferometer was demonstrated in 2024. A TM bar made of silicon was not suspended but fixed on a silicon breadboard. The optics made of silicon were glued on the breadboard as well and consisted of a monolithic interferometer. Two Fabry-Pérot cavities at both ends of the TM were operated stably at 12 K and achieved

the sensitivity of 3.6×10^{-14} m/$\sqrt{\text{Hz}}$ at 0.1 Hz [71, 99]. The performance was limited by the seismic noise on the vertical axis. It has become clear that vertical vibration isolation is necessary to reduce vertical seismic noise.

Another method to measure the rotation of the bar, using wavefront sensors with a folded cavity or a coupled cavity, was proposed [100]. These methods offer better sensitivity than conventional angular measurement methods, such as optical levers. Compared to rotation measurements using differential Fabry-Pérot cavities, the configurations and operation are more complicated. However, direct rotation measurement with wavefront sensors has the advantage of reduced cross-coupling noise. The basic principle of this method has been demonstrated from 2018 to 2021 [100–103]. Trade-off studies were conducted and two Fabry-Pérot cavities at both ends of the TM are the most promising candidate.

Suspension system

The Q factors of torsional mode with 1 mm thick sapphire fibers were measured. The maximum measured value was 1.3×10^5 at 1.31 Hz at room temperature [104]. The measurements at low temperatures are continuing with the aim of meeting the required specifications.

Cryogenic system

The cryogenic torsion pendulum was demonstrated in 2020 [105]. The TM bars were successfully cooled down to 6.1 K in 10 days, and the achieved sensitivity was 8.5×10^{-7} /$\sqrt{\text{Hz}}$ at 0.1 Hz as shown in Fig. 2.10. The sensitivity was limited by beam jitter noise. We found that both fiber-coupled light injection and vibration isolation of the OB are necessary to reduce beam jitter noise.

The achieved temperature was slightly higher than the target of 4 K, mainly because the second shield was heated by the electrical lead wires connected between the vacuum chamber flange and the second shield, and because the thermal conductivity of the heat links was 30%–50% lower than expected.

Vibration isolation system

A prototype of the vibration isolation system was developed, and its performance was tested in 2019 without the suspension system. The vertical seismic vibration was suppressed by 10^{-3} around 0.7 Hz, and the horizontal vibration by 3×10^{-2} around 1.7 Hz [71, 106].

However, the performance was still insufficient to meet the requirements. One reason was tilt-horizontal coupling [107] at frequencies below 0.5 Hz. This coupling distorted the true signal of the horizontal motion and introduced instability in the control. Another reason was the parasitic resonance modes of the supporting frame of the system. These modes prevented us from increasing the feedback gain and resulted in an inadequate suppression ratio.

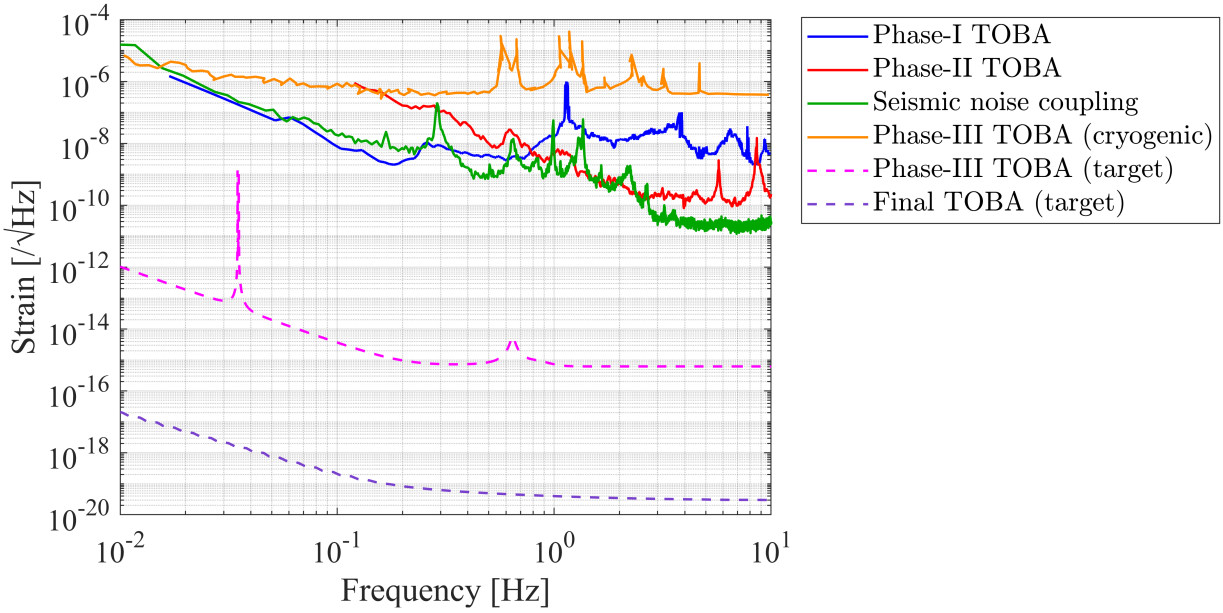

Figure 2.10: Achieved sensitivities of the prototype TOBAs and target sensitivities of Phase-III TOBA and Final TOBA. The blue, red, green, and orange lines represent the sensitivity of Phase-I TOBA [69], Phase-II TOBA [62], research on seismic noise coupling [95], and the cryogenic torsion pendulum for Phase-III TOBA [105], respectively. The dashed magenta (purple) line is the target sensitivity of Phase-III TOBA (Final TOBA [61]).

3 Experimental Setup

We designed and developed the optical and suspension system for Phase-III TOBA. In this chapter, we outline the objectives of the experiment in Section 3.1. We provide the conceptual design and discuss the design sensitivity in Section 3.2. Subsequently, we describe the overview of the experimental setup, optical system, suspension system, and sensors and actuators in detail in Section 3.3, Section 3.4, Section 3.5, and Section 3.6, respectively.

3.1 Objective

The objective of this work is to complete the integrated configuration of the optical and suspension systems of TOBA, addressing the issues identified during component development in previous studies. The role of this study within the TOBA development roadmap is summarized in Fig. 3.1. This research aims to finalize the optical and suspension system with cryogenic specification. Building on the outcomes of this work, the following advancements will be pursued: the implementation of silicon test masses (TMs), cooling of the optical and suspension systems, improvement of suspension wires, and the introduction of an active vibration isolation system. These steps are essential to achieving the target sensitivity for Phase-III TOBA. Subsequently, scaling up Phase-III TOBA will pave the way for realizing the Final TOBA.

3.2 Concept and design

3.2.1 Conceptual setup

The conceptual designs of this study and previous research [105] are illustrated in Fig. 3.2. A comparison of the designs in previous research [105], this study, and the Phase-III TOBA target is listed in Fig. 3.3.

In previous prototype TOBAs, the optical system used to detect TM rotation was either an optical lever or a Michelson interferometer. For Phase-III TOBA, this is replaced

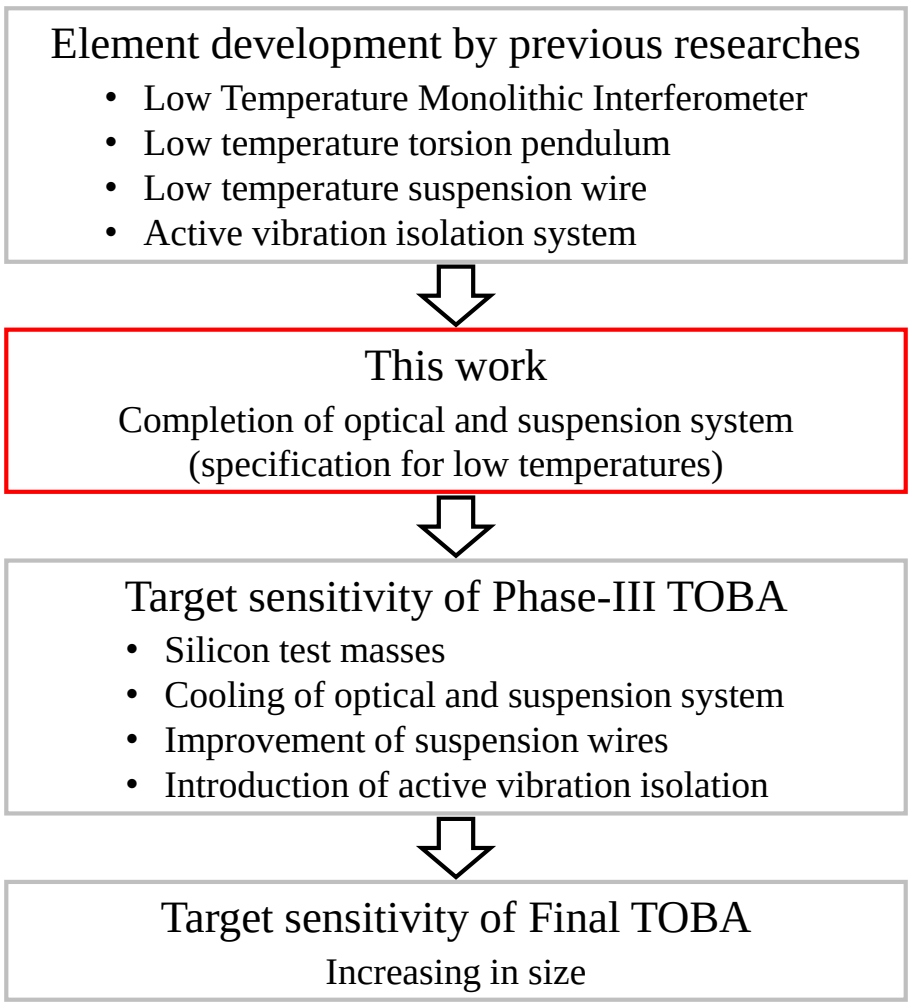

Figure 3.1: Objective of this work.

with a more sensitive differential Fabry-Pérot cavity. Optical levers are also included as auxiliary sensors.

In this study, we design the TMs with cryogenic silicon specification. We fabricate torsion pendulums designed to prevent silicon from cracking during cooling.

Additionally, the suspension system should be redesigned to minimize seismic noise coupling. In earlier setups, the TMs and optical bench (OB) were suspended on separate chains, with their relative motion being monitored. In this configuration vibrations from the OB were contributed as noise. Damping magnets were not suspended and that makes the passive vibration isolation ratio worse. Furthermore, no mechanisms for passively reducing vertical vibrations have been implemented so far, and coupling from vertical seismic noise has been identified as an issue in previous studies.

In this work, to prevent vibrations of the OB from contributing as noise, the OB and the TMs will be suspended on the same suspension chain. This design enables direct detection of the differential rotation between the two TMs without relying on the OB. A passive vertical vibration isolation mechanism will be installed in the suspension chain

for the first time in TOBA to reduce coupling from vertical seismic noise.

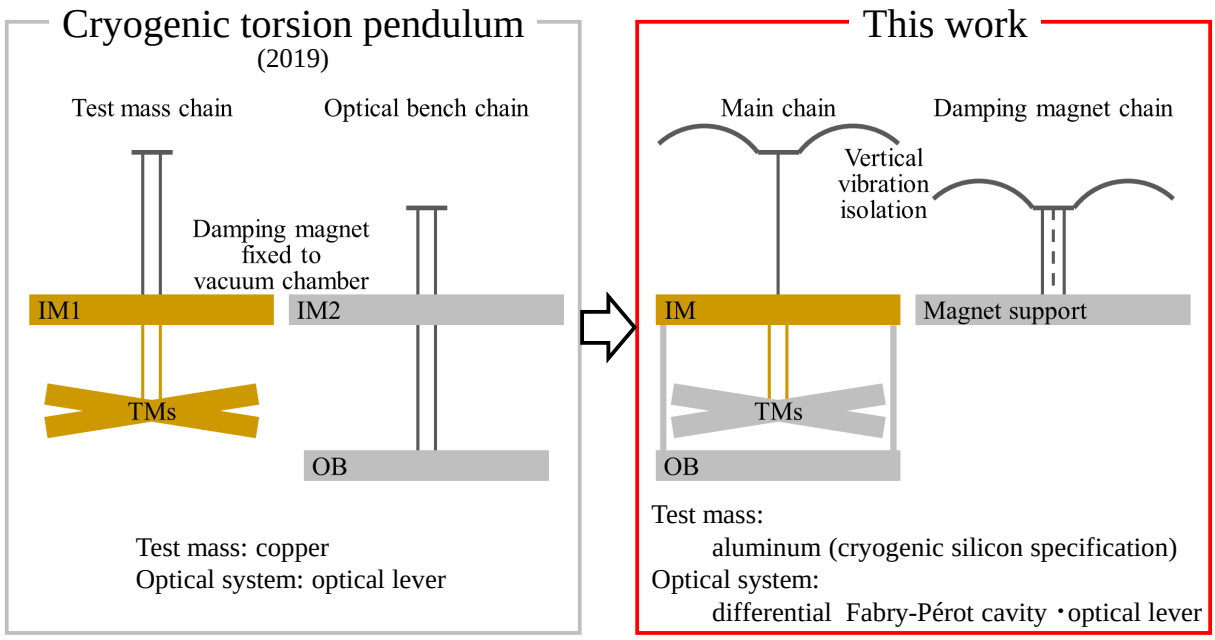

Figure 3.2: Overview of the conceptual setup. Overview of the cryogenic torsion pendulum for Phase-III TOBA in 2019 [105] is also illustrated for comparison with this work.

3.2.2 Design sensitivity and noise sources

The design sensitivity of the experiment is shown in Fig. 3.4. The target sensitivity is 6.6×10^{-9} rad/$\sqrt{\text{Hz}}$ at 0.1 Hz and 4.6×10^{-11} rad/$\sqrt{\text{Hz}}$ at 0.5 Hz. At frequencies below 0.35 Hz, the sensitivity is primarily limited by suspension thermal noise, while at frequencies above 0.35 Hz, translational seismic noise becomes dominant. If we achieve this target sensitivity, further improvement can be made by replacing the suspension wire, cooling the setup and installing the active vibration isolation system. The design parameters required to achieve the target sensitivity are summarized in Table 3.1. The noise sources are calculated using the design values as follows. Note that the design sensitivity in Fig. 3.4 is plotted in terms of the rotation angle, with the unit of rad/$\sqrt{\text{Hz}}$.

Suspension thermal noise

The TMs, with their parameters summarized in Table 3.1, are suspended using copper beryllium wires. With these parameters, we calculate:

$$\kappa = 3.3 \times 10^{-4}\,\text{N m/rad}, \tag{3.1}$$

$$f_0 = \frac{1}{2\pi}\sqrt{\frac{\kappa}{I}} = 28.7\,\text{mHz}. \tag{3.2}$$

		Phase-III TOBA		
		Cryogenic torsion pendulum (2019)	This work	Target
Optical system	Optical lever	✓	✓	✓
	Differential Fabry-Pérot cavity	None	✓	✓
Suspension system	Test mass	Copper	Aluminum (silicon specification design)	Silicon
	Suspension wire	Copper beryllium (Q factor 10^3)	Copper beryllium (Q factor 10^3)	Silicon (Q factor 10^8)
	Optical bench	Suspended by different chain than TM	Suspended by same chain as TM	Suspended by same chain as TM
	Damping magnets	Fixed	Suspended	Suspended
	Passive vertical vibration isolation	None	✓ (GAS filter)	✓
Cryogenic system		✓ (6K)	None	✓ (4 K)
Active vibration isolation		None	None	✓

Figure 3.3: Summary of the conceptual setup. The configuration of the cryogenic torsion pendulum for Phase-III TOBA in 2019 [105] and the target of Phase-III TOBA is summarized for comparison with this work.

From Eq. (2.26), we calculate:

$$\sqrt{S_{\mathrm{th,sus,TM}}(f)} \simeq 2.5\times10^{-11}\left(\frac{T}{300\,\mathrm{K}}\right)^{\frac{1}{2}}\left(\frac{\phi_{\mathrm{wire}}}{1\times10^{-3}}\right)^{\frac{1}{2}}\left(\frac{f}{0.1\,\mathrm{Hz}}\right)^{-\frac{5}{2}}\mathrm{rad}/\sqrt{\mathrm{Hz}}. \tag{3.3}$$

The intermediate mass (IM), with their parameters summarized in Table 3.1, is suspended using tungsten wire and damped through eddy current damping. According to [108], the suspension thermal noise due to the damped IM is calculated as follows:

$$\sqrt{S_{\mathrm{th,sus,IM}}(f)} \simeq 6.6\times10^{-9}\left(\frac{T}{300\,\mathrm{K}}\right)^{\frac{1}{2}}\left(\frac{f_{\mathrm{Y,IM}}}{37.9\,\mathrm{mHz}}\right)^{2}\left(\frac{f}{0.1\,\mathrm{Hz}}\right)^{-4}\mathrm{rad}/\sqrt{\mathrm{Hz}}. \tag{3.4}$$

Quantum noise

We assume the optical parameters as summarized in Table 3.1. The shot noise is calculated by Eq. (2.38) as follow:

$$\sqrt{S_{\mathrm{shot}}(f)} \simeq 9.4\times10^{-17}\left(\frac{P_0}{1\,\mathrm{mW}}\right)^{-\frac{1}{2}}\left(\frac{\mathcal{F}}{300}\right)^{-1}\left(\frac{D}{110\,\mathrm{mm}}\right)^{-1}\mathrm{rad}/\sqrt{\mathrm{Hz}}. \tag{3.5}$$

The radiation pressure noise is given by Eq. (2.39) as follow:

$$\sqrt{S_{\mathrm{RP}}(f)} \simeq 2.8\times10^{-16}\left(\frac{P_0}{1\,\mathrm{mW}}\right)^{\frac{1}{2}}\left(\frac{\mathcal{F}}{300}\right)\left(\frac{D}{110\,\mathrm{mm}}\right)\left(\frac{f}{0.1\,\mathrm{Hz}}\right)^{-2}\mathrm{rad}/\sqrt{\mathrm{Hz}}. \tag{3.6}$$

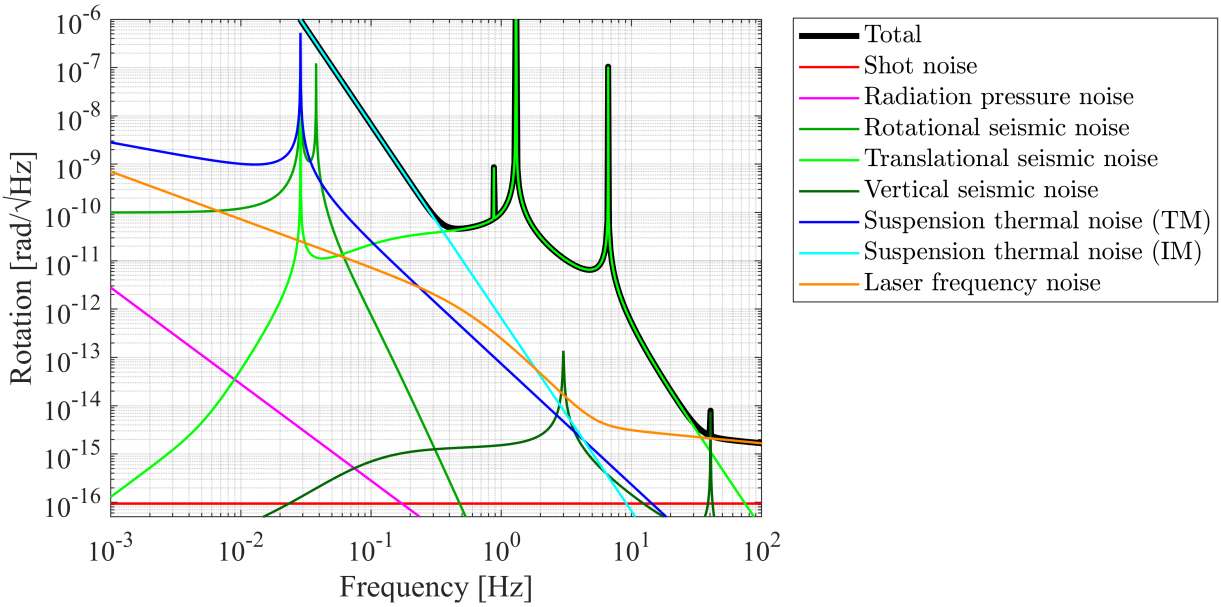

Figure 3.4: Design sensitivity of the experiment. The black line represents the total sensitivity, and other colored lines show the noise budget.

The contribution from shot noise and radiation pressure noise is negligible compared to other noises for the experiment.

Rotational seismic noise

From the parameters of the TMs suspended by a double-stage pendulum, the transfer function Eq. (2.42) above 0.1 Hz is approximated to

$$H_{\mathrm{rot}}(f) \simeq 1.4 \times 10^{-2} \left(\frac{f}{0.1\,\mathrm{Hz}} \right)^{-4}. \tag{3.7}$$

Here we assume the rotational seismic noise to be

$$\sqrt{S_{\mathrm{g,rot}}} = \frac{1 \times 10^{-10}\ \mathrm{rad}/\sqrt{\mathrm{Hz}}}{1 + (f/0.1\,\mathrm{Hz})^2}. \tag{3.8}$$

We calculate from Eq. (2.43)

$$\sqrt{S_{\mathrm{seis,rot}}(f)} \simeq 7.3 \times 10^{-13} \left(\frac{f}{0.1\,\mathrm{Hz}} \right)^{-4} \mathrm{rad}/\sqrt{\mathrm{Hz}}. \tag{3.9}$$

Translational seismic cross-coupling noise

Here the spectrum of translational seismic noise is modeled using the following equation, which was obtained by fitting the measurement results from a seismometer:

$$\sqrt{S_{\mathrm{g,trans}}} = \frac{1 \times 10^{-5}\ \mathrm{rad}/\sqrt{\mathrm{Hz}}}{1 + (f/0.1\,\mathrm{Hz})^2}. \tag{3.10}$$

Table 3.1: Design parameters of the experiment.

Parameter	Value
Optical system	
Wavelength of laser	1550 nm
Power of laser	1 mW
Finesse of Fabry-Pérot cavity	300
Length of Fabry-Pérot cavity	23 mm
Distance between two Fabry-Pérot cavities	110 mm
CMRR for laser frequency noise	0.02
Suspension system	
Moment of inertia of TM	$0.010\,\mathrm{kg\,m^2}$
Length of wire for TM	122 mm
Diameter of wire for TM	0.3 mm
Loss angle of wire for TM	1×10^{-3}
Torsional resonant frequency of TM	28.7 mHz
Moment of inertia of IM	$0.022\,\mathrm{kg\,m^2}$
Length of wire for IM	320 mm
Diameter of wire for IM	0.4 mm
Loss angle of wire for IM	1×10^{-3}
Torsional resonant frequency of IM	37.9 mHz
Tilt angle of TM	1×10^{-4} rad
Tilt angle of end mirrors of cavities	1×10^{-4} rad
CMRR for translational motion	0.02
Resonant frequency of GAS filter	3 Hz
Temperature	300 K

We assume the tilt angles of the TMs are suppressed below $\phi_{\mathrm{R}} = \delta x/\delta z = 1 \times 10^{-4}\,\mathrm{rad}$ and $\phi_{\mathrm{P}} = \delta y/\delta z = 1 \times 10^{-4}\,\mathrm{rad}$, the tilt angle of two mirrors is $\phi_{\mathrm{mir}} = 1 \times 10^{-4}\,\mathrm{rad}$, and the CMRR for translational mode is $C_{\mathrm{CMRR}} \simeq 0.02$. From Eq. (2.44)–Eq. (2.47), $\sqrt{S_{\mathrm{seis,trans}}(f)} \simeq 2.2 \times 10^{-11}\ \mathrm{rad}/\sqrt{\mathrm{Hz}}$ at 0.1 Hz. The values of the moments of inertia and resonant frequencies for various degrees of freedom used in the calculations are described in detail in Section 3.5 and Section 4.2. Among the terms in Eq. (2.44), the first and third terms are dominant. The sensitivity above 0.35 Hz is limited by translational seismic noise.

Vertical seismic cross-coupling noise

Here the spectrum of vertical seismic noise is modeled using the following equation:

$$\sqrt{S_{\mathrm{g,trans}}} = \frac{1 \times 10^{-5}\ \mathrm{rad}/\sqrt{\mathrm{Hz}}}{1 + (f/0.1\,\mathrm{Hz})^2}. \tag{3.11}$$

By assuming the tilt angle of two mirrors is $\phi_{\mathrm{mir}} = 1 \times 10^{-4}\,\mathrm{rad}$, the resonant frequency of GAS filter is 3 Hz, and the CMRR for translational mode is $C_{\mathrm{CMRR}} \simeq 0.02$, the vertical

seismic cross-coupling noise is calculated to be $\sqrt{S_{\mathrm{seis,trans}}(f)} \simeq 7.0 \times 10^{-16}$ rad/$\sqrt{\mathrm{Hz}}$ at 0.1 Hz.

Laser frequency noise

Substituting the cavity length $l_{\mathrm{cav}} = 23\,\mathrm{mm}$, the distance between two cavities $D = 110\,\mathrm{mm}$, and the laser frequency $\nu_0 = c/\lambda = 193\,\mathrm{THz}$ into Eq. (2.57). Here we assume the CMRR is $C_{\mathrm{CMRR}} = 0.02$. Then, we get the value of

$$\sqrt{S_{\mathrm{freq}}(f)} \simeq 7.2 \times 10^{-12} \left(\frac{C_{\mathrm{CMRR}}}{0.02}\right) \left(\frac{\sqrt{S_\nu(f)}}{3.3 \times 10^5\ \mathrm{Hz}/\sqrt{\mathrm{Hz}}}\right) \mathrm{rad}/\sqrt{\mathrm{Hz}}. \tag{3.12}$$

at 0.1 Hz. For the spectrum of laser frequency noise $\sqrt{S_\nu(f)}$, a model obtained by fitting measurements taken using an asymmetric Michelson interferometer is employed.

3.3 Overview of experimental setup

The overview of the experimental setup is shown in Fig. 3.5. The suspension system is placed inside the vacuum chamber, and the laser source is located outside the chamber. Laser light is introduced into the vacuum chamber and onto the OB using optical fibers. Photographs of the setup in the vacuum chamber are shown in Fig. 3.6.

3.4 Optical system

3.4.1 Input optics

The schematic of the input optics outside the chamber is shown in Fig. 3.7. The laser source with a wavelength of 1550 nm and a power of 40 mW is a fiber laser and used for Fabry-Pérot cavities. Laser light passes through a fiber isolator to prevent light from returning to the light source, a fiber electro-optic modulator (EOM) to apply phase modulation, and a fiber polarizer to suppress the residual amplitude modulation (usually called RAM) caused by the EOM. It is introduced into a vacuum chamber through a fiber feedthrough.

The laser source with a wavelength of 1064 nm and a power of 500 mW is spatial light and is used for the optical levers. The polarization axis of the laser is aligned to a Faraday isolator through a quarter-wave plate (QWP) and a half-wave plate (HWP) (but in this case, we misaligned the polarization axis to dump the laser power to inject into an optical fiber), then the laser passes through the Faraday isolator to prevent returned light. Two lenses are used to mode-match the beam width to a collimator and a HWP aligns the polarization axis to s-polarization for an optical fiber. A neutral density (ND) filter is used to reduce the light intensity to 20 mW, and the light is introduced into the optical fiber through the collimator. The two mirrors in front of the collimator are steering mirrors

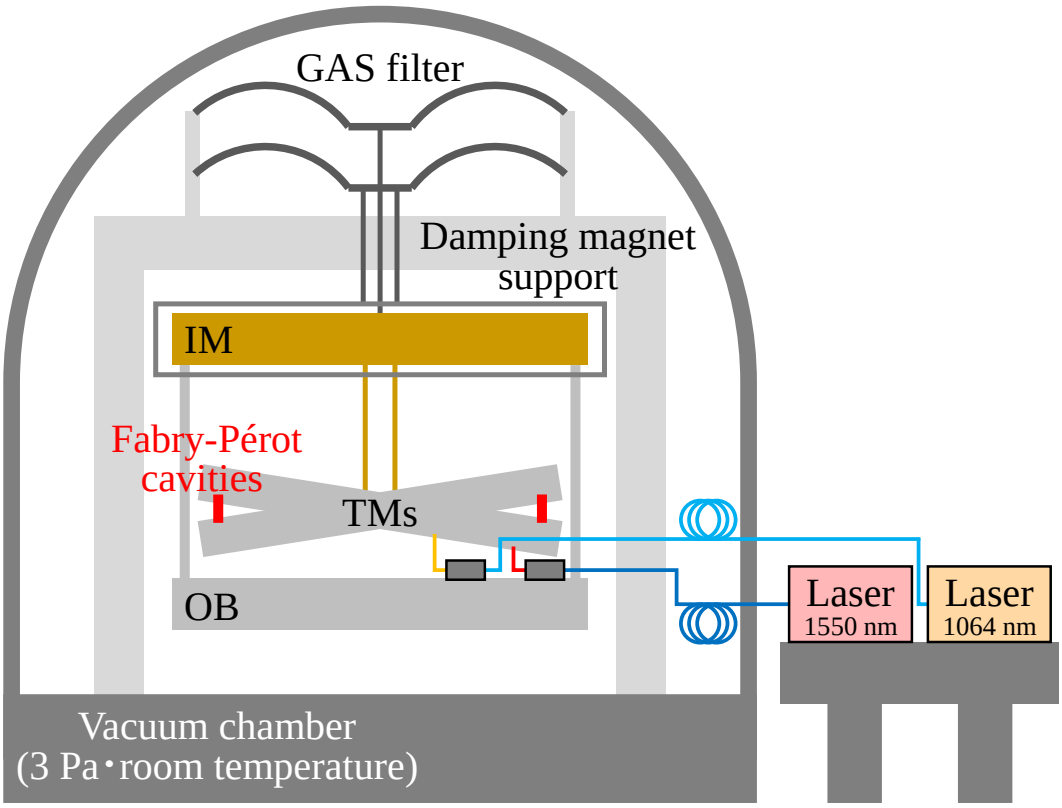

Figure 3.5: Overview of the experimental setup.

for alignment. As with the 1550 nm laser beam, the 1064 nm beam is introduced into the vacuum chamber through the fiber feedthrough.

3.4.2 Optics on optical bench

Fig. 3.8 shows the schematic of the optics on the OB. Two TMs, each with a length of 300 mm, TM1 and TM2, are arranged orthogonally. Both TM1 and TM2 are equipped with two wing-shaped components for each to improve symmetry; details will be explained in Section 3.5. Two front mirrors are attached to TM1, and two end mirrors are attached to TM2, forming two Fabry-Pérot cavities between TM1 and TM2. From the front mirror side, the left cavity is labeled as Cavity1, and the right as Cavity2. The cavity length is set as short as possible, and the distance between the two cavities is set as long as possible to suppress frequency noise, as discussed in Section 2.4.6. The curvature of the end mirrors was designed to be flat to reduce coupling from translational seismic noise and to anticipate that the surface of the TMs will be polished and directly coated in the future, as discussed in Section 2.4.3. Coils are mounted in a similar configuration to the cavities, forming two sets of coil-coil actuators between TM1 and TM2 (two additional sets of coil-coil actuators are implemented for symmetry). By forming cavities and actuators between the two TMs, the system prevents the motion of the OB from contributing as noise. Additionally, auxiliary sensors in the form of optical levers are included. Oplev1

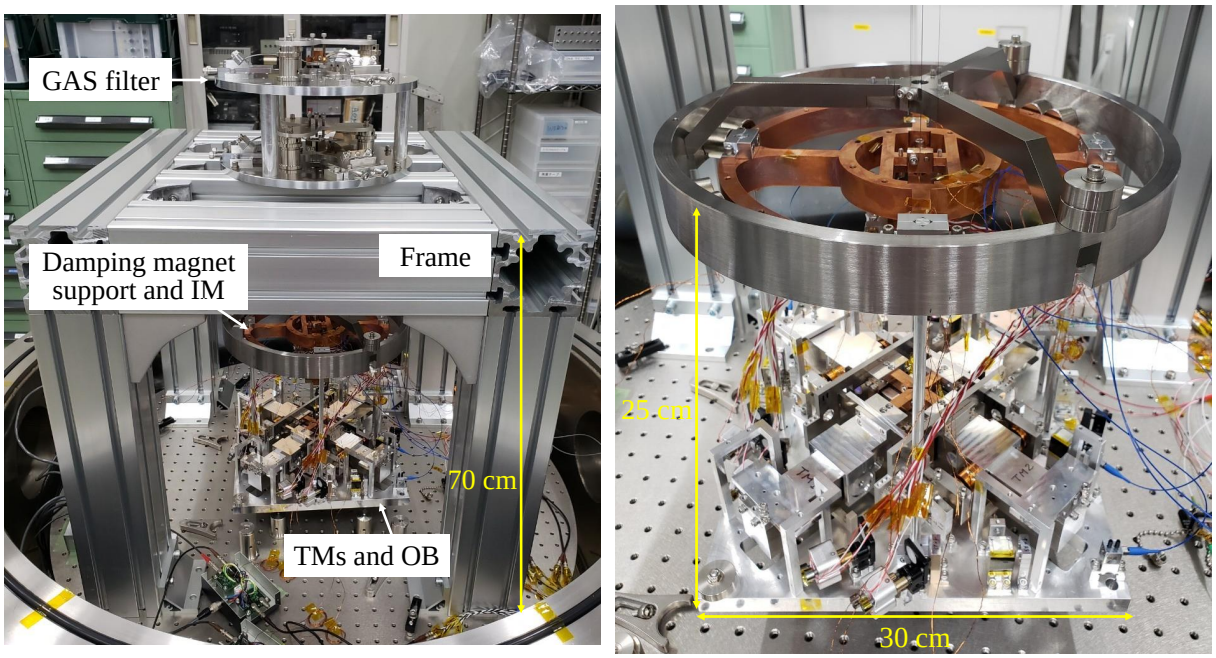

Figure 3.6: Pictures of the entire setup. Left: picture of the entire setup including frames support the GAS filters. Right: picture of the TMs, OB, IM and damping magnet support.

detected the rotation of TM1, while Oplev2 detected the rotation of TM2.

The laser light is introduced into the vacuum chamber through a fiber feedthrough, and a 50:50 fiber coupler splits the laser beam into two. The laser beam is emitted from the collimators as a spatial light. A total of four collimators are located on the OB (two collimators for 1550 nm and two for 1064 nm). The laser wavelength is 1550 nm for the cavities and 1064 nm for the optical levers. The laser beam with the wavelength of 1550 nm passes through two mode-matching lenses for the Fabry-Pérot cavity, is aligned by two steering mirrors with piezoelectric transducer (PZT) drive motors, and then is injected to the cavity. The front mirrors of the cavities are glued to a wing-shape component attached to TM1, The end mirrors are glued to TM2. On the front mirror side, a beam splitter (BS) and photodiode (PD) are placed to detect reflected light, and on the end mirror side, a PD is placed to get transmitted light after passing through a hole in TM2. The laser light with the wavelength of 1064 nm is used for optical lever. After passing through the BS, it hits the mirror attached to the wing-shape component attached to TM1 (for Oplev1) or TM2 (for Oplev2) and the light is reflected and returns to the BS. Then it is aligned by the steering mirror and enters the quadrant photodiode (QPD). Note that in Fig. 3.8 the laser beam at the unused port of the BS is dumped.

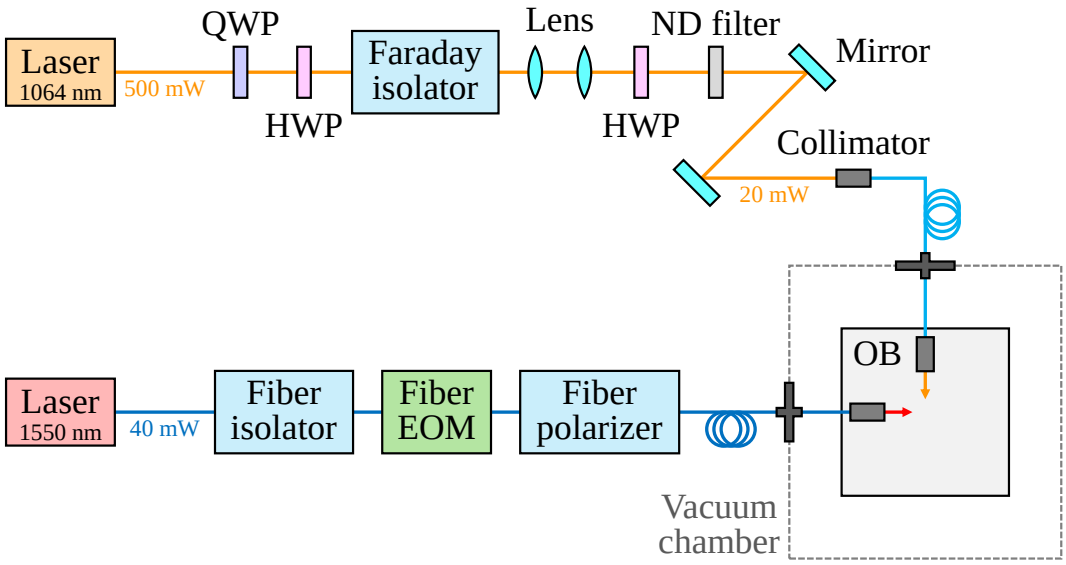

Figure 3.7: Schematic of the input optics.

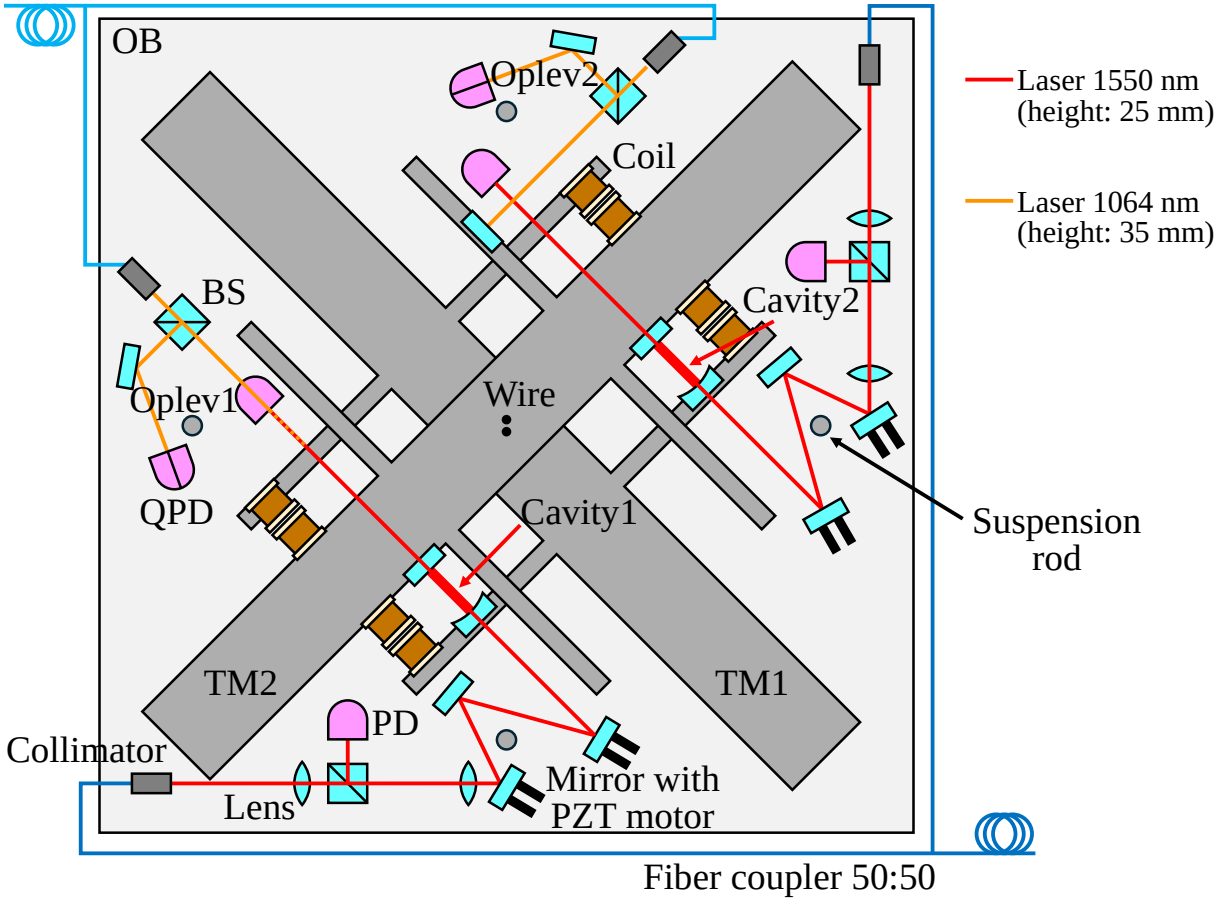

Figure 3.8: Schematic of the optics on the OB. This is a top view, and the TMs and the OB are suspended in a double-pendulum configuration. The elements drawn in light blue represent optical components such as mirrors, lenses, and BSs. The elements drawn in pink represent PDs and QPDs.

Fig. 3.9 is the picture of the optics on the OB. The mirrors and lenses are half inch in diameter and the BS is 10 mm per side. The mirrors, lensed, BSs, PDs, and QPDs are glued to holders made of aluminum, and the holders are screwed on the OB. Only the steering mirrors with PZT drive motors in front of the cavities and the steering mirrors in front of the QPDs for the optical levers are installed on commercial mirror mounts.

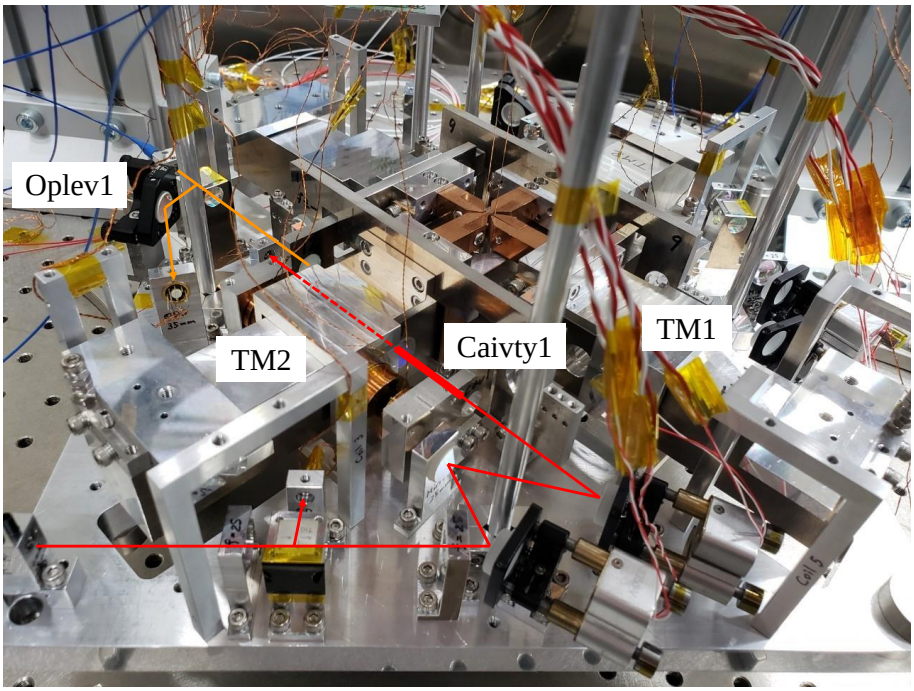

Figure 3.9: Picture of the optics on the OB.

3.5 Suspension system

3.5.1 Overview

The overview of the suspension system is shown in Fig. 3.10. The suspension system consists of two chains: a main chain that includes the TMs, and an auxiliary chain that suspends only the damping magnet support as illustrated in Fig. 3.10 (a). The heights of the top suspension points differ between the two chains, and both are equipped with geometric anti-spring (GAS) filters at their suspension points to provide vertical vibration isolation.

In the main chain, the IM is suspended by a single wire from the GAS filter. From the IM, two TMs are independently suspended, each by a single wire. The OB is suspended from the same IM using four rods, each 7 mm in diameter. The system is designed to minimize relative motion between the OB and TMs by suspending the OB and TMs from the common IM, and by suspending the OB with thick rods to ensure that the OB and IM move as a single unit within the observation frequency band.

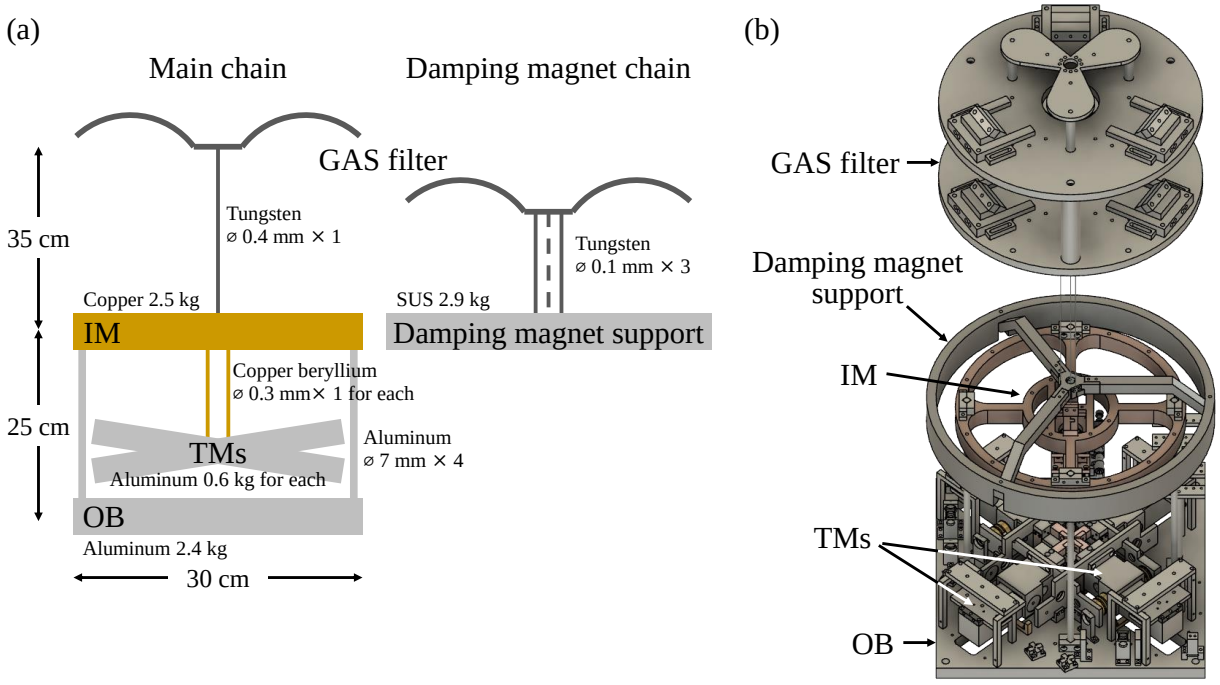

Figure 3.10: Overview of the suspension system: (a) the system consists of two independent suspension chains (left: main chain, right: damping magnet chain), (b) the heights of the intermediate mass (IM) and the damping magnet support are aligned, with the IM enclosed within the damping magnet support.

The damping magnet support is suspended by three wires from its GAS filter. The heights of the damping magnet support and the IM are aligned, with the damping magnet support positioned to enclose the IM as shown in Fig. 3.10 (b). A set of permanent magnets is attached to the inner surface of the damping magnet support, providing eddy current damping to suppress the motion of the IM. By suspending the damping magnet support and passively isolating it from seismic noise, the system prevents the motion of the magnets from contributing to noise via eddy current damping.

Furthermore, the TM, IM, and damping magnet support are designed to be installed into the cryogenic first shield in the vacuum chamber of the Phase-III TOBA with the size of $340 \times 355 \times 403\,\mathrm{mm}^3$. The GAS filter is also designed to fit into the active vibration isolation stage of the Phase-III TOBA.

Design parameters of the suspension system are summarized in Table 3.2. In this section, we describe the design of the TMs, OB, IM, damping magnet support, and GAS filter one-by-one.

3.5.2 Test masses and attached components

The two TMs are designed with their central sections removed and interlocked orthogonally, as shown in Fig. 3.11, ensuring that their centers of mass are at the same height. Aligning the centers of mass in this manner minimizes coupling noise from translational

Table 3.2: Design parameters of the suspension system.

Parameter	Value
TMs	
Material	Aluminum
Mass (TM only)	0.63 kg
Mass (with attached components)	1.17 kg
Moment of inertia for Yaw	5.45×10^{-3} kg m^2
Moment of inertia for Pitch	9.62×10^{-5} kg m^2
Moment of inertia for Roll	5.45×10^{-3} kg m^2
Distance between suspension point and center of mass	27 mm
Wire for the TMs	
Material	Copper beryllium
Young's modulus	132 GPa
Poisson's ratio	0.30
Length	122 mm
Diameter	0.3 mm
Number of wire	One for each TM
OB	
Material	Aluminum
Mass	2.4 kg
Rods for the OB	
Material	Aluminum
Length	235 mm
Diameter	7 mm
Number of wire	Four
IM	
Material	Copper
Mass	2.5 kg
Moment of inertia for Yaw	2.23×10^{-2} kg m^2
Wire for the IM	
Material	Tungsten
Young's modulus	411 GPa
Poisson's ratio	0.28
Length	320 mm
Diameter	0.4 mm
Number of wire	One
Damping magnet support	
Material	Magnetized stainless steel
Mass	2.9 kg
Wire for the damping magnet support	
Material	Tungsten
Length	190 mm
Diameter	0.2 mm
Number of wire	Three

seismic noise. In TorPeDO, as shown in Fig. 1.7, the two TMs are positioned at different heights, whereas TOBA adopts a unique design feature to align their centers of mass. The arrangement of the cavities also differs significantly from TorPeDO and represents another distinct design feature of TOBA. In TorPeDO, as shown in Fig. 1.7, mirrors are mounted diagonally at the ends to form four cavities. In contrast, TOBA constructs two cavities. To enhance the relative parallelism of the two mirrors, the TMs are directly polished and coated with high-reflectivity coatings to serve as mirrors. In the future, silicon TMs with coatings will be employed. However, in this experiment, fused silica mirrors are bonded to aluminum TMs. As shown in Fig. 3.11, holes are prepared in the TMs for bonding the mirrors. Aluminum was selected as the TM material for this experiment because its density ($2.7\,\mathrm{g/cm^3}$) closely matches that of silicon ($2.33\,\mathrm{g/cm^3}$). The TM is a rectangular block measuring $300 \times 30 \times 30\,\mathrm{mm^3}$, with a mass of 0.63 kg.

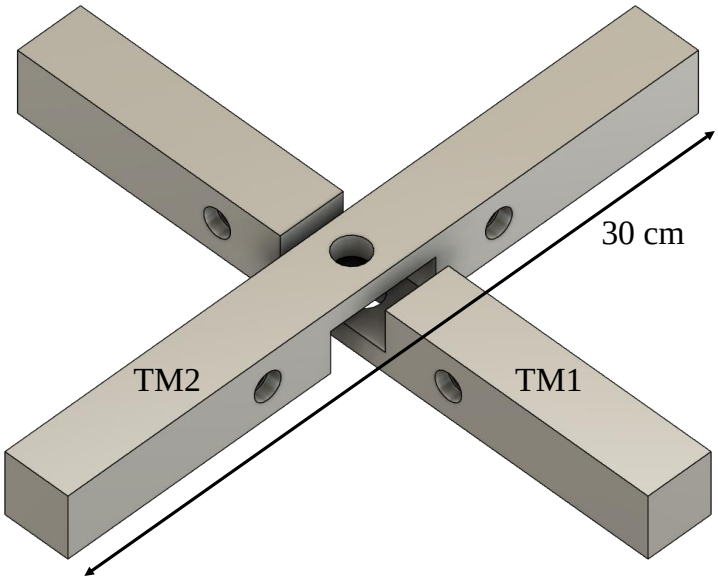

Figure 3.11: 3D CAD model of the TMs.

A 3D computer-aided design (CAD) model of the TM and its attached components is shown in Fig. 3.12. Anticipating the future use of silicon TMs and further cooling, the parts are not screwed into the TM to avoid cracking. The TM is designed so that only low thermal expansion invar, which has a thermal expansion coefficient similar to silicon, is directly glued to the TM.

First, two bottom supports made of invar are glued to the underside of the TM. Next, two side supports made of phosphor bronze are screwed in place, positioned adjacent to each other. A support for the wing-shaped component (hereafter referred to simply as the "wing") and coils are attached to these side supports. Additionally, a clamp is screwed in and positioned between the two supports for the wing and coils, securing them from both sides. The wing support is installed from below to increase the wing's inherent resonant frequency up to $\sim 600\,\mathrm{Hz}$. Furthermore, supports for balance weights made of invar are glued to both ends of the upper side of the TM, and a support for coils is screwed onto

these. If coils for Pitch and Roll control are required in the future, they can be attached to these supports (though they are not used in this experiment).

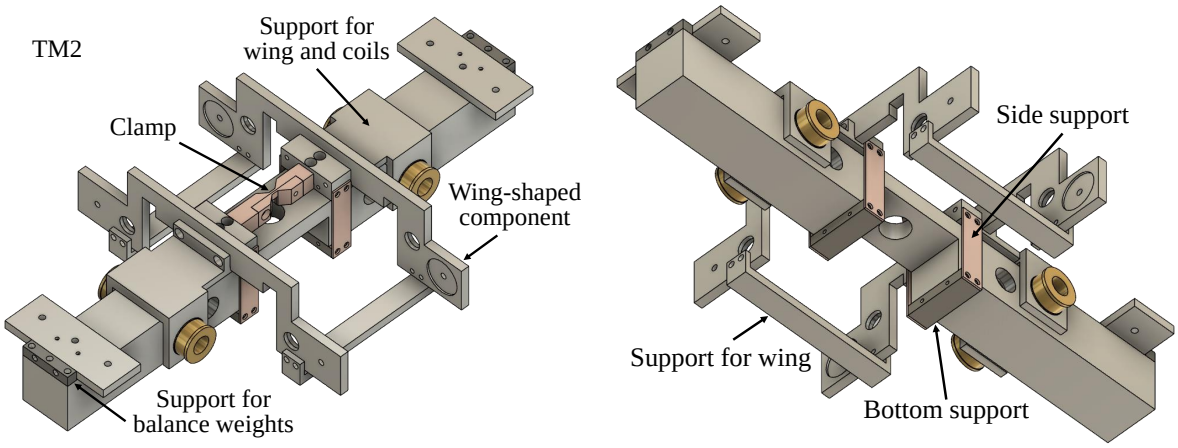

Figure 3.12: 3D CAD model of TM2 and its attached components.

A 3D CAD model of the two TMs and their attached parts is shown in Fig. 3.13. The TMs, clamps, and wings are all assembled with TM2 on the upper side and TM1 on the lower side.

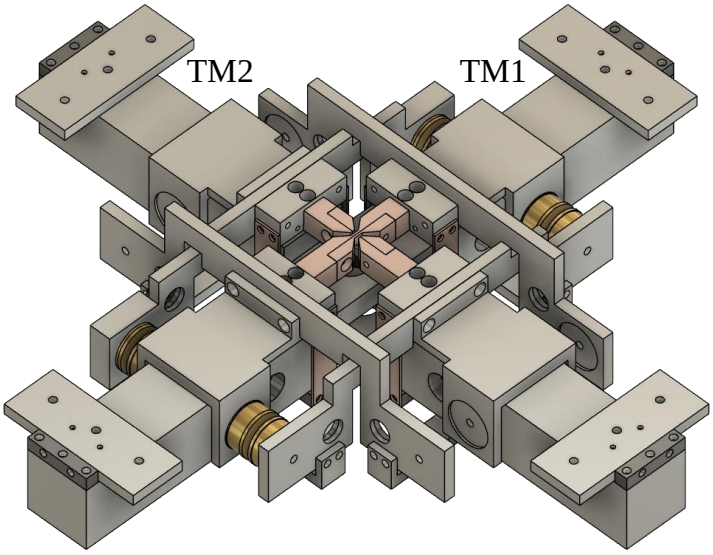

Figure 3.13: 3D CAD model of the two TMs and their attached components.

A close-up view of the area surrounding the TM clamp is shown in Fig. 3.14. In the 3D CAD model on the left, one side of the clamp is removed for illustration purposes. The clamp features protrusions designed to align the wire and keep it straight. The closer the distance between the two wires, the more effective the cancellation of common-mode

noise in rotation and translation. Due to manufacturing constraints of the clamp, the distance was set to 4 mm.

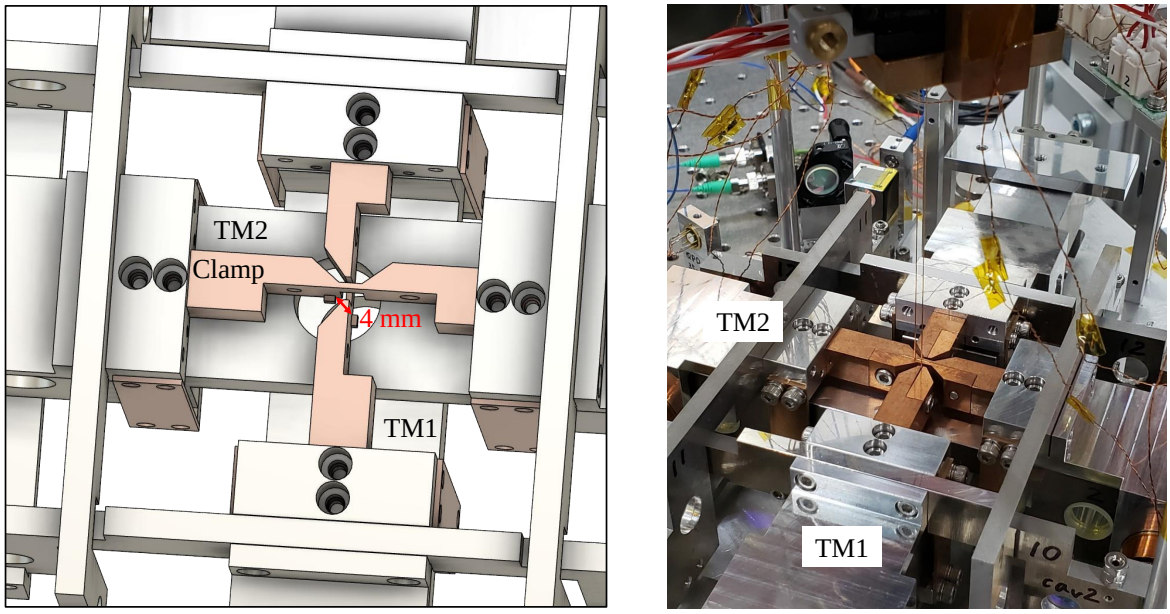

Figure 3.14: Close-up view of the area surrounding the TM clamp. Left: 3D CAD model. Right: picture.

When the TM is suspended, it may tilt slightly due to misalignment between the suspension point and the center of mass or non-uniformity in the mass distribution. As discussed in Section 2.4.3, this tilt causes coupling of translational seismic noise, requiring adjustments using balance weights. By placing screws and nuts in the screw holes on the balance weight supports at both ends of the TM and on the top of the wings as shown in Fig. 3.15, the tilt was adjusted to less than 2 mrad (corresponding to a height difference of 0.5 mm at the ends of the TM).

3.5.3 Optical bench

The OB is a square made of aluminum with sides of 280 mm, a thickness of 15 mm and a mass of 2.4 kg. The side length of 280 mm is the maximum size that can be installed in the vacuum chamber and cryocooler of Phase-III TOBA. The 15 mm thickness is designed to increase the intrinsic resonant frequencies. To reduce its mass, the area beneath the TM, where no optical elements are placed, is hollowed out.

The OB is suspended from the same IM as the TMs using four aluminum rods, each with a diameter of 7 mm, as shown in Fig. 3.16. By suspending the OB and TMs from a common IM, and further suspending the OB with thick rods to ensure that the OB and IM move as a single unit within the observation frequency band, the system is designed to minimize relative motion between the OB and TMs. The lowest resonant frequency of the torsional mode of the OB is simulated to be 13 Hz using 3D CAD, while the translational

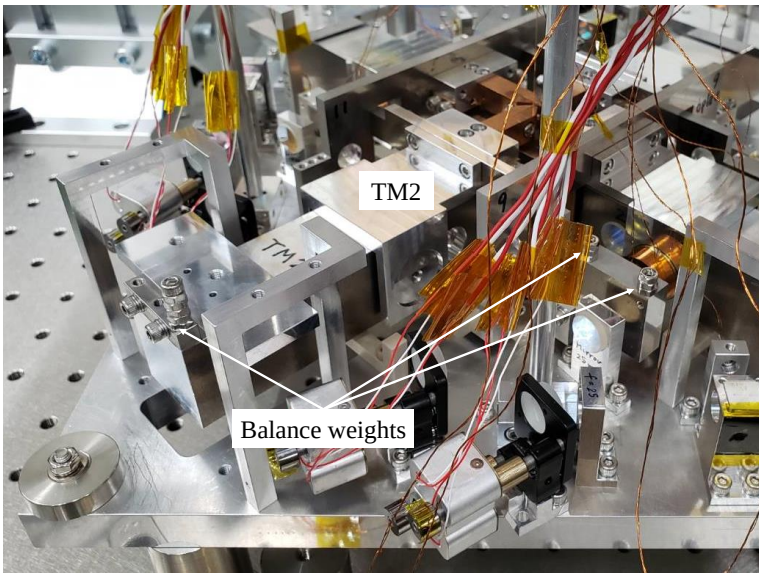

Figure 3.15: Picture of balance weights on TM2.

mode is 68 Hz. Both frequencies are sufficiently higher than the observation frequency band of TOBA.

3.5.4 Intermediate mass

The IM is a ring-shaped disk with a diameter of 240 mm and a mass of 2.5 kg. It is designed in a ring shape to increase the moment of inertia and lower the torsional resonant frequency. Copper was chosen for its material to enable eddy current damping using magnets. As shown in Fig. 3.16, it is suspended by a single wire.

As shown in Fig. 3.17, two rotation stages for the TMs are installed below the IM to compensate the DC rotation of the TMs caused by the stiffness of the wire. The upper clamp for the TMs precisely sets and clamps the distance between the two wires, while the bottom clamps secure the wires to the rotation stages. The effective wire length that determines the rotational and translational frequencies of the TM is measured from the bottom clamp downwards.

3.5.5 Damping magnet support

The damping magnet support is a ring-shaped disk with a diameter of 300 mm and a mass of 2.9 kg (3.6 kg including the magnets and balance weights). Magnetized stainless steel was chosen for attaching permanent magnets. As shown in Fig. 3.18, it is suspended by three wires and the heights of the damping magnet support and the IM are aligned, with the damping magnet support positioned to enclose the IM. Several permanent magnets are attached to the inside of the damping magnet support, and the IM is damped through eddy current damping. By suspending the damping magnet support and passively isolating it

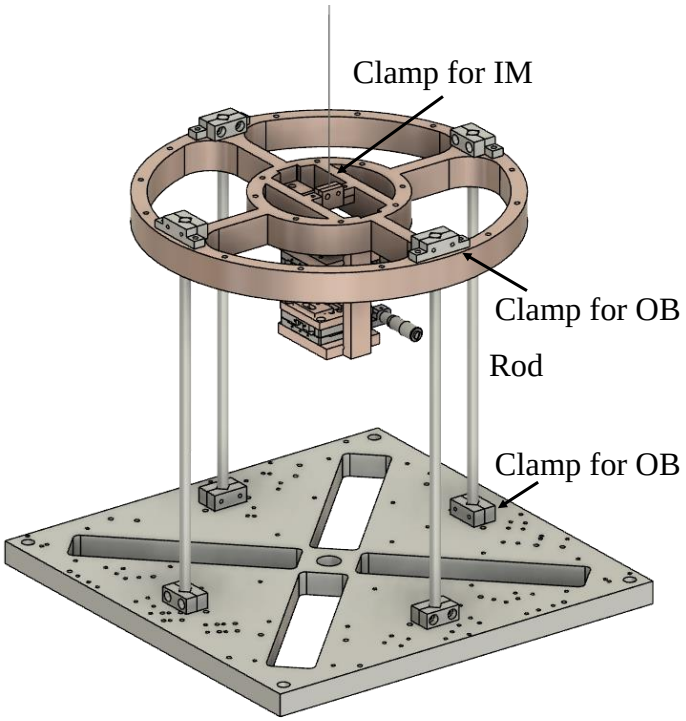

Figure 3.16: 3D CAD model of the OB and the IM.

from seismic noise, the system prevents the motion of the magnets from contributing to noise via eddy current damping.

3.5.6 GAS filter

Passive vibration noise isolation in the vertical direction can be achieved by introducing a mechanism with a low resonant frequency in the vertical direction, similar to horizontal vibration isolation. However, it is difficult to achieve a low resonant frequency in the vertical direction because the stiffness required to hold a payload contradicts the softness needed for a low resonant frequency. The geometric anti-spring (GAS) filter is a low-frequency vertical spring that can resolve this contradiction. The concept of GAS filter was first proposed by [109]. It was then improved by [110] and [111]. These GAS filters all had a composite structure. The monolithic configuration of the GAS filter was later developed by [112].

A GAS filter consists of a set of radially converging blades. The monolithic GAS blades are initially straight when unloaded, as shown in Fig. 3.19 (left), and are bent by a vertical load, as shown in Fig. 3.19 (right). The blades are clamped at a fixed angle. An intuitive explanation of the working principle of the GAS filter is as follows. The monolithic GAS blades are horizontally compressed by pushing against each other at the center. Due to the symmetry of the filter around its center, the horizontal compression forces cancel each other out. As a result, the center ring of the blades does not move horizontally and is geometrically constrained to move purely in the vertical direction. It

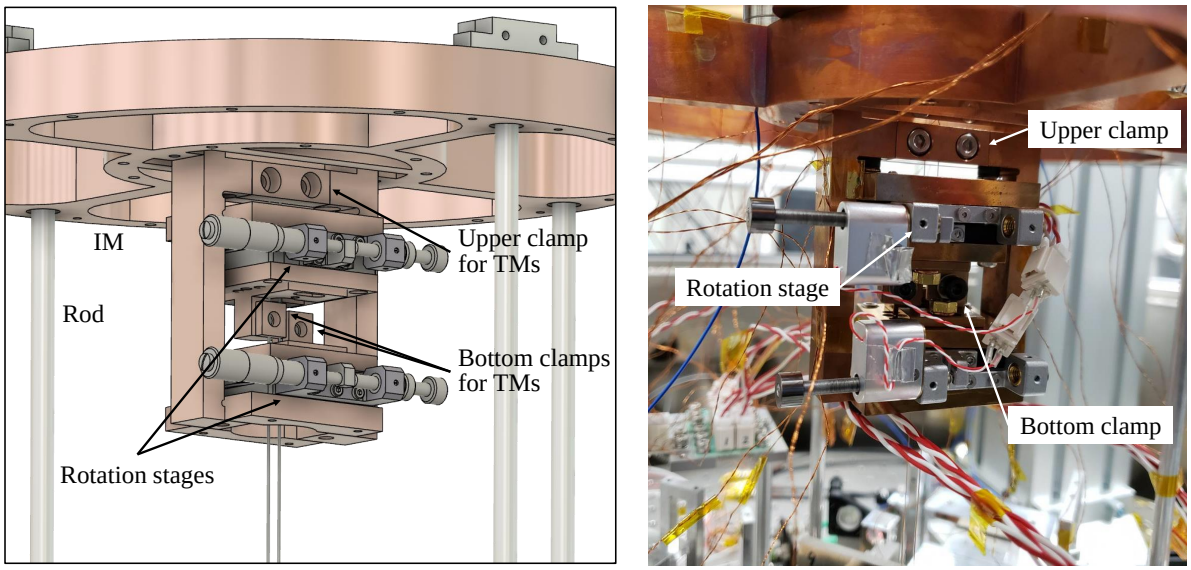

Figure 3.17: Close-up view of the area surrounding the rotation stages. Left: 3D CAD model. Right: picture.

is this geometric constraint that produces the anti-spring effect.

In this experiment, for the first time in TOBA, the GAS filter is installed at the suspension point. Previous studies [113, 114] have used Maraging steel, known for its excellent strength and toughness. However, due to its high cost and difficulty in obtaining, this study fabricates the GAS filter using stainless steel for springs, SUS304-CSP, which has not been done before. Additionally, the load is lighter, ranging from several kg to 10 kg, compared to previous studies. See Section 4.2.3 and Section 4.2.4 for the evaluation of the GAS filter, and see Appendix A for the drawings of the monolithic GAS blades and construction of the GAS filter.

3.5.7 Suspension jigs

To facilitate the suspension and installation into the vacuum chamber, the suspension jigs were carefully designed. As shown in Fig. 3.20, there are plates beneath the IM and the OB, and four rods connect them. As shown in the left picture of Fig. 3.21, the jigs were used to precisely suspend the OB and IM from the IM outside the vacuum chamber. After that, as shown in the right picture of Fig. 3.21, the jigs were installed into the vacuum chamber, and the IM is suspended, and then the jigs were disassembled inside the chamber and removed. By performing more tasks outside the vacuum chamber and fewer inside, the work efficiency is significantly improved. The jigs are designed to be installed directly into the vacuum chamber and cryocooler of Phase-III TOBA.

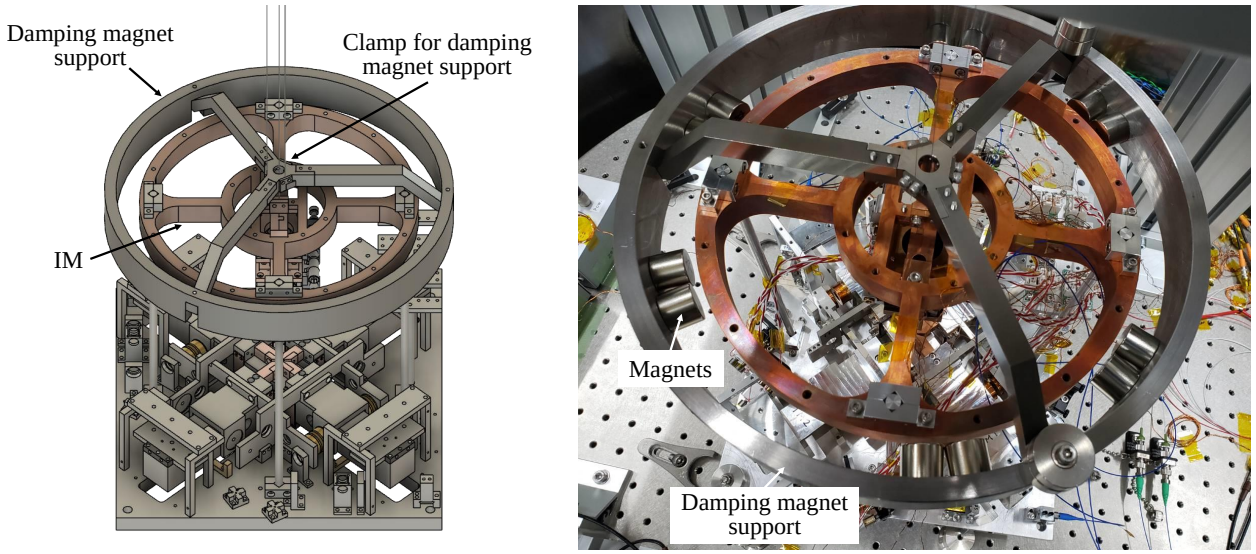

Figure 3.18: 3D CAD model (left) and picture (right) of the damping magnet support.

3.6 Sensors and actuators

As shown in Fig. 3.8, four single PDs and two QPDs are located on the OB. The PDs are used to acquire reflected and transmitted light from Fabry-Pérot cavities. The QPDs is used for optical levers as auxiliary sensors. An optical lever is a simple sensor to measure the displacement of laser beam reflected by a tilted mirror. As shown in Fig. 3.8, the split beams are sent to the mirrors on the wings, then reflected to the QPDs. The amplitude of signal is given by

$$\delta P_{\mathrm{oplev}}(\theta) = P_{\mathrm{QPD}} \frac{8}{\sqrt{2\pi}} \frac{d}{w_{\mathrm{QPD}}} \theta, \tag{3.13}$$

where P_{QPD} and w_{QPD} are the laser power and beam radius at the QPD, respectively, and d is the distance between the mirror and the QPD. The optical lever has wider range, therefore it is suitable for auxiliary rotational monitor.

In addition, to apply a force on TMs for position controls, coil-coil actuators are attached on TMs. The coil-coil actuators are actuators developed for TOBA [115, 116]. The configuration and an example of usage of a coil-coil actuator is shown in Fig. 3.22. The principle and advantages are described below.

The coil-coil actuator consists of a pair of coils. An alternating current (AC) is applied to both coils facing each other to generate a magnetic field. The interaction of the magnetic fields creates an attractive or repulsive force between the two coils. Consider an AC with drive frequency $f_d = \omega_d/2\pi$. f_d is assumed to be sufficiently higher than the control bandwidth. When an AC $I_1 = i_1 \exp(i\omega_d t)$ is applied to one coil and an AC $I_2 = i_2 \exp(i\omega_d t + \phi)$ is applied to the other coil, time average of the energy stored in the

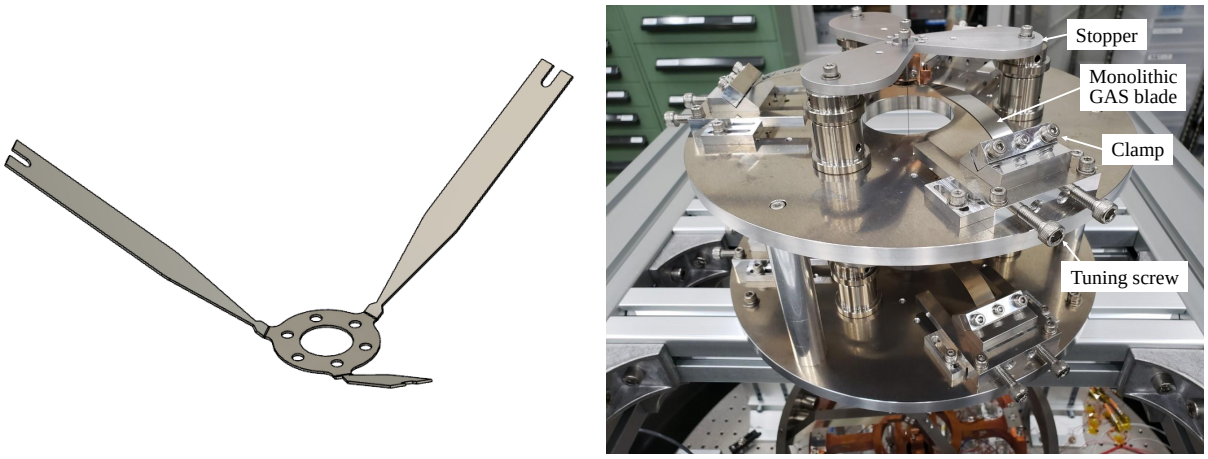

Figure 3.19: 3D CAD model and picture of the GAS filter. Left: 3D CAD model of the monolithic GAS blades before bending. Right: Picture of the GAS filter after the blades have been bent.

two coils is

$$\begin{aligned}\bar{T} &= \frac{1}{2}L_1|I_1|^2 + \frac{1}{2}L_2|I_2|^2 + M\,\mathrm{Re}[I_1 I_2] \\ &= \frac{1}{2}L_1 i_1^2 + \frac{1}{2}L_2 i_2^2 + M i_1 i_2 \cos\phi, \end{aligned} \tag{3.14}$$

where L_1 and L_2 are the self-inductance of coils, and M is the mutual inductance between the two coils. The force acting on the actuator can be written as

$$F = \frac{\partial T}{\partial x} = \frac{\mathrm{d}M}{\mathrm{d}x} i_1 i_2 \cos\phi. \tag{3.15}$$

Thus, by varying i_1, i_2 or the phase difference ϕ, the force on the coil-coil actuator changes, and furthermore, this force can be either an attractive or a repulsive force.

The coil-coil actuator offers two primary advantages for use in TOBA. One is its low magnetic noise, as the induced magnetic moment oscillates at the drive frequency, resulting in an average magnetic moment of zero. This reduces coupling with environmental magnetic field fluctuations, which increase at low frequencies. The second advantage is the adjustability of actuator efficiency to minimize actuator noise. Electrical noise in the actuator's control signal translates into force noise through the actuator. By adjusting the applied current amplitudes i_1 or i_2, the coupling from electrical noise can be remotely optimized.

Four sets of coil-coil actuators are installed as shown in Fig. 3.8, but only the cavity side is actually used. The coil-coil actuators on the opposite side were installed to symmetrically distribute the mass of the TMs and to reduce the unwanted tilt. We choose the drive frequency $f_d = 1\,\mathrm{kHz}$ and two facing coils are separated by 2.9 mm. The self-inductance of the coil is $L_{1,2} = 3.28\,\mathrm{mH}$. See Section 4.3 for the evaluation of coil-coil actuators efficiency.

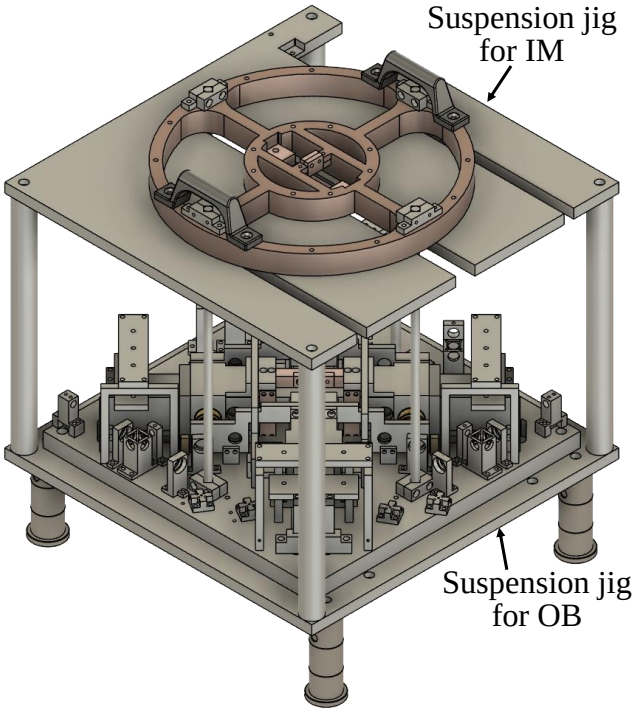

Figure 3.20: 3D CAD model of the suspension jigs.

The wires from these PDs, QPDs, and coils are collected in the cable holder on the OB as shown in Fig. 3.23 and then connected to the circuit box. Note that the wires (and optical fibers) are routed through the center of the IM so as not to increase the resonant frequency of the TM and OB in the rotational direction.

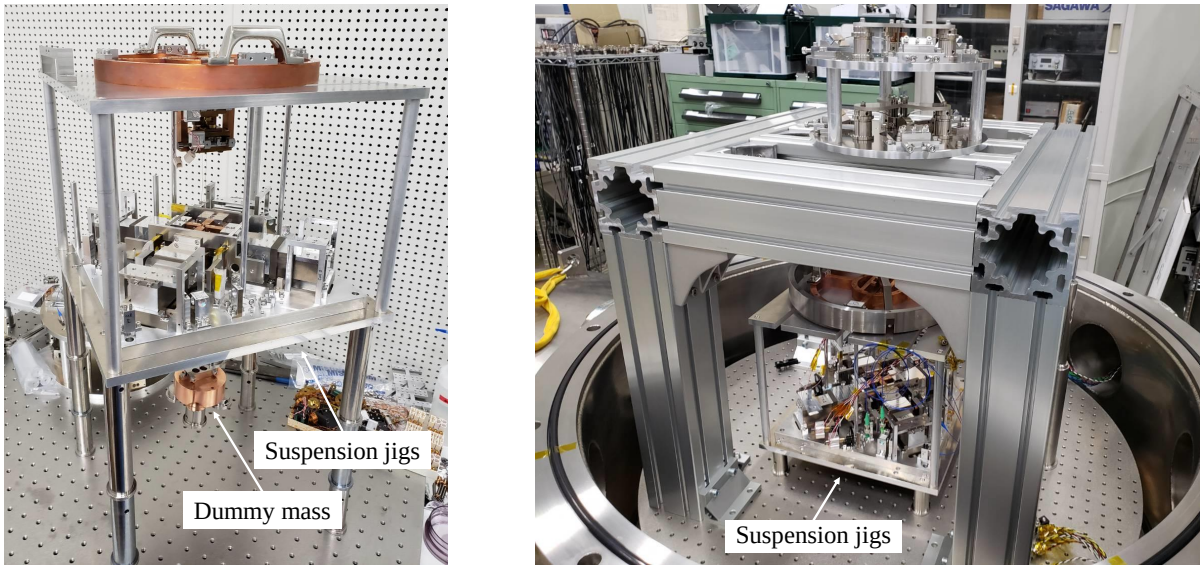

Figure 3.21: Pictures of the suspension jigs. Left: picture of suspending the TMs outside the vacuum chamber. Right: picture of installing the suspension system into the vacuum chamber.

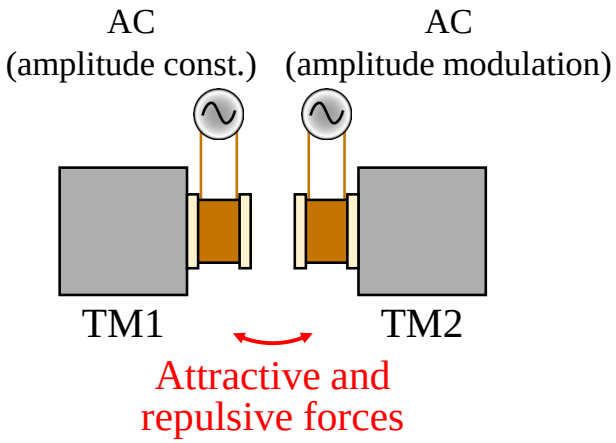

Figure 3.22: Configuration and example of usage of a coil-coil actuator.

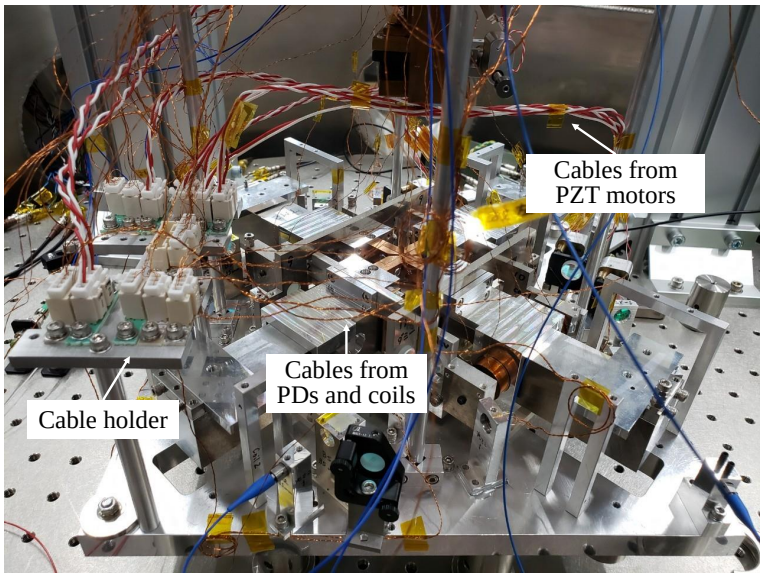

Figure 3.23: Picture of the cable holder on the OB.

4 Results and Discussion

In the previous chapter, we described the detail design of the experimental setup. Here we show the results of the measurement and discuss them. First we characterize the optical system in Section 4.1, and the suspension system in Section 4.2. Then we evaluate the efficiency of coil-coil autuators in Section 4.3 and discuss the path to locking the Fabry-Pérot cavities in Section 4.4. The rotation sensitivity is presented in Section 4.5 and discuss the noise investigation in Section 4.6.

4.1 Characterization of optical system

4.1.1 Mode-matching ratios for Fabry-Pérot cavities

The laser beam width inside a Fabry-Pérot cavity has a spatial eigenmode. It is determined by the length of the cavity and the curvature of the front and end mirrors By injecting a laser beam with a beam width matching this eigenmode into the cavity, high resonance state can be achieved.

The parameters of the Fabry-Pérot cavity in the experiment are summarized in Table 4.1. With this design, the eigenmode of the Fabry-Perot cavity was calculated as shown in Table 4.2. In all the following, the origin of the spatial profile of the beam radius is the edge of the collimator. To achieve the eigenmode, the location of lenses was designed as shown in Fig. 4.1. Two lenses with a focal length of 25 mm were placed between the collimator and the front mirror for mode-matching. The calculation also takes into account refraction by the front mirror of 6.35 mm thick fused silica. As shown in Fig. 3.8, the configuration allows to put PDs for reflected light and steering mirrors on the OB while the laser beam avoids hitting the suspension rods of the OB.

Fig. 4.2 compares the measured radius of the beam emitted from the collimator with the specification value of the collimator. Fig. 4.3 shows the measured beam radius after passing through the lenses. Both the results for Cavity1 and 2 in the horizontal (x-axis) and vertical (z-axis) are in good agreement with the designed beam radius. We calculated the estimated mode-matching ratio with the measurement results as described in Table

Table 4.1: Parameters and performance of the Fabry-Pérot cavities.

Parameter	Value
Length	23 mm
FSR	6.5 GHz
RoC of front mirror	100 mm
RoC of end mirror	∞ (flat)
Reflectivity of front mirror	99%
Reflectivity of end mirror	99.5%
Designed finesse	417
Measured finesse for Cavity1	328 ± 27
Measured finesse for Cavity2	257 ± 19

Table 4.2: Mode-matching ratios for the Fabry-Pérot cavities.

Parameter	Designed value	Cavity1	Cavity2
Beam waist size for x-axis	149.8 μm	155.2 μm	149.3 μm
Beam waist size for z-axis	149.8 μm	152.5 μm	156.6 μm
Location of beam waist for x-axis	267 mm	263 mm	257 mm
Location of beam waist for z-axis	267 mm	265 mm	269 mm
Estimated mode-matching ratio	-	99.8%	99.3%

4.2 by the following equation [117]:

$$M = 4\sqrt{\frac{z_0^2 z_x z_y}{\{(z_0+z_x)^2+(d_0-d_z)^2\}\{(z_0+z_z)^2+(d_0-d_z)^2\}}}, \tag{4.1}$$

where d_0 is the target waist position, z_0 is the target Rayleigh range, d_x, d_z are the waist positions in the x- and z-axes, and z_x, z_z are the Rayleigh ranges in the x- and z-axes, respectively. Rayleigh range z is defined as

$$z = \frac{\pi w^2}{\lambda}, \tag{4.2}$$

where w is the beam waist size and λ is the wavelength of the laser. The estimated mode-matching ratios were above 95%, which is sufficient.

4.1.2 Finesses of Fabry-Pérot cavities

We measured the finesse, which is a physical quantity that indicates the resonant performance of a Fabry-Pérot cavity. The finesse is expressed by the following equation.

$$\mathcal{F} \equiv \frac{\nu_{\mathrm{FSR}}}{\nu_{\mathrm{FWHM}}}, \tag{4.3}$$

$$\nu_{\mathrm{FSR}} = \frac{c}{2l_{\mathrm{cav}}} \tag{4.4}$$

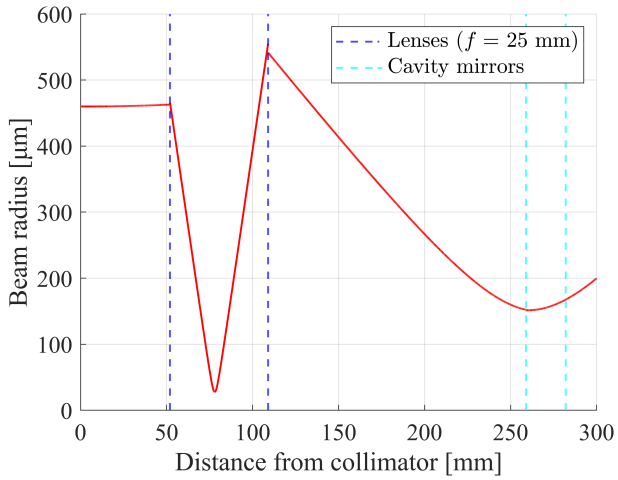

Figure 4.1: Design spatial profile of the beam radius for the Fabry-Pérot cavity. The red line indicates the spatial profile of the beam radius. The blue (cyan) dashed lines represent the locations of the mode-matching lenses with a focal length of 25 mm (cavity mirrors of 6.35 mm thick fused silica).

where ν_{FSR} is a free spectral range (FSR) in units of frequency, and ν_{FWHM} is a frequency of full width at half maximum (FWHM) of a resonant peak.

The TMs were fixed to the OB with jigs, and the resonant peak of transmitted light was obtained by applying a triangular wave voltage from a function generator to the PZT actuator in the laser source to scan the frequency. The frequency was calibrated by phase modulating with a 50 MHz signal from the function generator to the fiber EOM and setting radio frequency (RF) sideband peaks on both sides of the carrier to obtain ν_{FWHM} as shown in Fig. 4.4.

The measured finesses were summarized in Table 4.1. Errors were determined based on the standard deviation of 10 times measurements. The results for both Caivity1 and 2 were significantly smaller than the designed finesse, but in terms of shot noise levels, these values are acceptable. The results can be explained by the light losses of approximately 0.4% and 0.9% in the cavities, respectively. We confirmed that the finesses were comparable even after the jig that had secured the TMs to the OB was removed and the torsional pendulums were released and suspended.

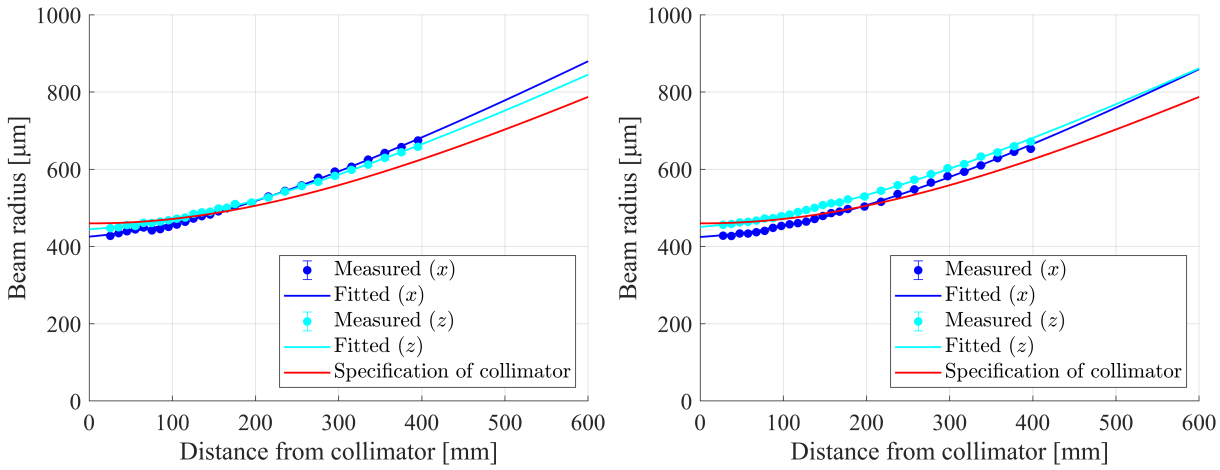

Figure 4.2: Beam radius after fiber collimators for Cavity1 (left) and Cavity2 (right). The blue (cyan) dots and line represent the measured data and fitting results for the x-axis (z-axis). The red line indicates the specification of the fiber collimator.

4.2 Characterization of suspension system

4.2.1 Resonant frequency and Q factor of Yaw mode

The resonant frequency of each pendulum mode is calculated as follows:

$$f_{\mathrm{T}} = \frac{1}{2\pi}\sqrt{\frac{g}{l+\delta z}}, \tag{4.5}$$

$$f_{\mathrm{V}} = \frac{1}{2\pi}\sqrt{\frac{k}{M}}, \qquad \kappa = \frac{\pi E d^2}{4l}. \tag{4.6}$$

$$f_{\mathrm{P}} = \frac{1}{2\pi}\sqrt{\frac{Mg\,\delta z}{I_{\mathrm{P}}}}, \tag{4.7}$$

$$f_{\mathrm{R}} = \frac{1}{2\pi}\sqrt{\frac{Mg\,\delta z}{I_{\mathrm{R}}}}, \tag{4.8}$$

$$f_{\mathrm{Y}} = \frac{1}{2\pi}\sqrt{\frac{\kappa}{I_{\mathrm{Y}}}}, \qquad \kappa = \frac{\pi E d^4}{64l(1+\nu)}, \tag{4.9}$$

$$\tag{4.10}$$

Here the subscript T, V, P, R, and Y indicate translational, vertical, Pitch, Roll, and Yaw modes, respectively. I and M are the moment of inertia and mass, and d, l, E, and ν are the diameter, length, Young's modulus, and Poisson's ratio of the wire. δz is the distance between the suspension point and the center of mass. The designed resonant frequencies obtained by substituting the parameters of Table 4.4 into these equations and the measured resonant frequencies are summarized in Table 4.3 and Table 4.4.

The resonant frequency and Q factors of Yaw mode were measured by ringdown method. The torsion pendulums were excited at 0.1 Hz by coil-coil actuators. After

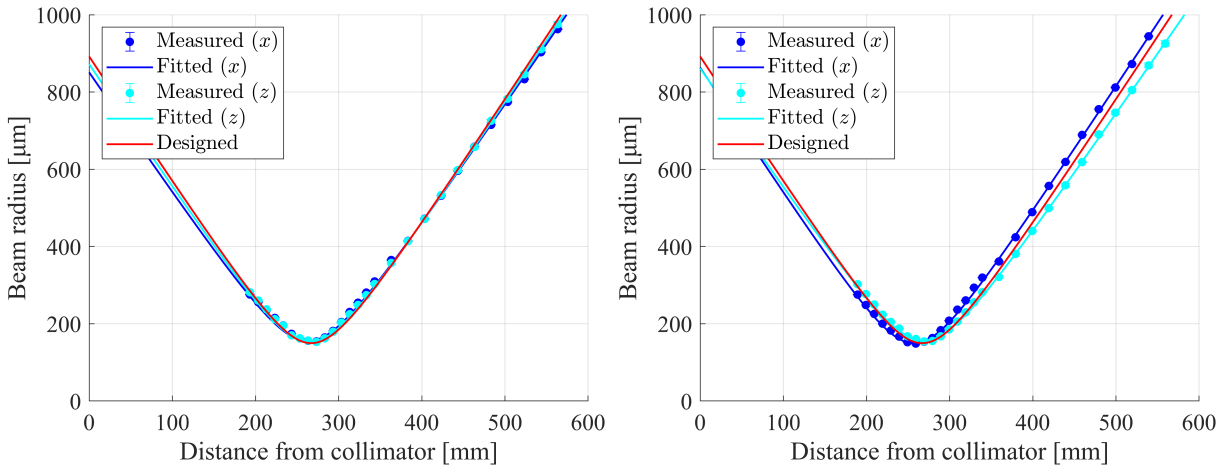

Figure 4.3: Beam radius after mode-matching lenses for Cavity1 (left) and Cavity2 (right). The blue (cyan) dots and line represent the measured data and fitting results for the x-axis (z-axis). The red line indicates the designed beam radius.

Table 4.3: Resonant frequency and Q factor of Yaw mode.

Quantity	Designed value	TM1	TM2
Resonant frequency at 1×10^5 Pa	28.7 mHz	117.9 ± 0.1 mHz	117.9 ± 0.1 mHz
Q factor at 1×10^5 Pa	1×10^3	55.2 ± 0.4	39.8 ± 0.2
Resonant frequency at 3.5 Pa	28.7 mHz	117.1 ± 0.1 mHz	117.3 ± 0.1 mHz
Q factor at 3.5 Pa	1×10^3	66.8 ± 1.5	46.5 ± 0.3

the excitation was turned off, time series data in Yaw mode were acquired by optical levers and the resonant frequencies and Q factors were measured. These measurements were performed at atmospheric pressure (1×10^5 Pa) and vacuum (3.5 Pa). The results are shown in Table 4.3 and Fig. 4.5. Errors were obtained by fitting.

As shown in Table 4.3, the torsional resonant frequencies increased to approximately four times the design value. To expand the observation band and enhance passive vibration isolation, it is necessary to reduce these frequencies. The increase in the torsional resonant frequency is likely due to the coil wires contributing significantly to the torsional restoring force. For each TM, the suspension wire has a diameter of 0.3 mm and uses a single wire, whereas the coil wires have a diameter of 0.2 mm and use eight wires, which likely has a significant impact. To address this issue, potential solutions include using thinner wires for the coils, supplying current without physical contact or controlling the Fabry-Pérot cavities without relying on coil-coil actuators.

The measured Q factors were approximately 50 under both atmospheric and vacuum conditions, compared to the design value of 1000. The Q factor due to damping from residual gas is estimated to be approximately $\sim 6 \times 10^6$, so this possibility can be ruled out. If the Q factor reduction is caused by the coil wires, improvements will be required, similar to the case of the torsional resonant frequency. On the other hand, when the Q factor decrease is due to damping of the IM that suppresses the RMS of displacement,

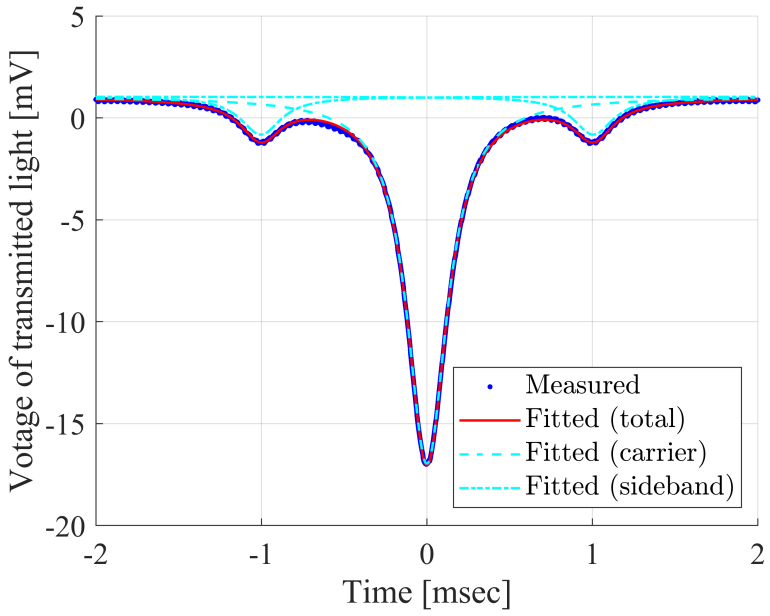

Figure 4.4: Cavity scan around a resonant peak for finesse measurement (Cavity1). The blue dots represent the measured data, and the red line indicates the fitting result for the sum of three Lorentzian peaks with the same line width. The cyan dashed (dash-dotted) line is the contribution from the carrier (sideband). The resonant frequency of the sideband corresponds to 50 MHz from the carrier.

this outcome aligns with expectations. As shown in Fig. 3.4, the designed sensitivity is limited by the thermal noise of the damped IM above 0.35 Hz. A reduced Q factor worsens the thermal noise. To reduce the thermal noise of the damped IM to the same level as the suspension thermal noise of the TM and achieve the target sensitivity of Phase-III TOBA, either of the following is required: improving the Q factor to $\sim 1 \times 10^8$ or reducing the torsional resonant frequency of the IM to about 1 mHz, as shown in Fig. 4.6.

4.2.2 Resonant frequencies of pendulum modes

To investigate the resonant frequencies of pendulum modes other than Yaw mode, the GAS filter was excited by hand, and the spectra of the optical levers were measured after the GAS vibration decreased in a few minutes. The results are shown in Fig. 4.7 and Table 4.4.

The difference of the resonant frequency in the translational mode between the designed and measured values might be caused by the change of the center of mass and moment of inertia due to the attached components to the TM, such as the wing and coils, and the restoring force due to the wires of the coils. For the calculation of the resonant frequency of each mode, the measured value including attached parts was used for the mass M. On the other hand, we simulated the distance between the suspension point and the center of mass δz using only the TM and calculated the moment of inertia of each mode $I_{\mathrm{P,R,Y}}$ assuming uniform mass distribution because it takes high cost for a

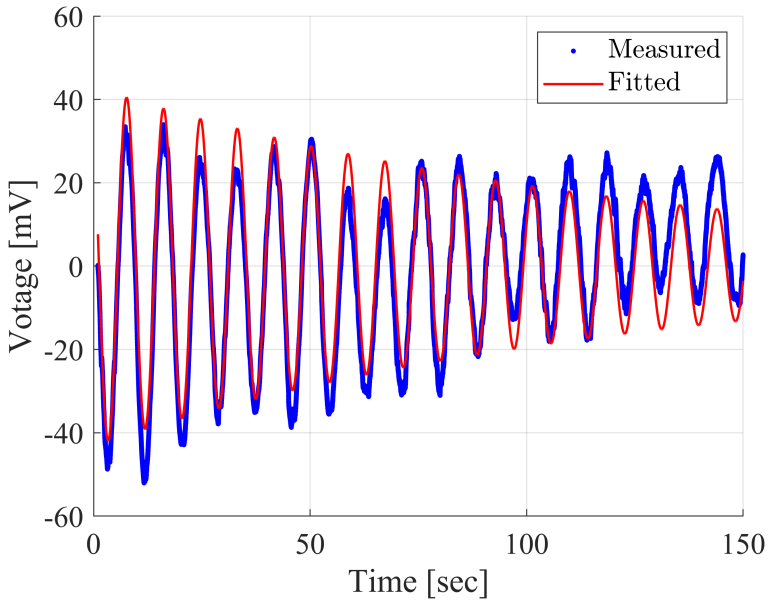

Figure 4.5: Ringdown oscillation of Yaw mode (TM2, 3.5 Pa). The blue dots represent the measured data, and the red line indicates the fitting result.

CAD simulation. This is believed to have resulted in differences between the design and measured values. For the vertical mode, which is not affected by δz and I, the designed and measured values agreed precisely. To satisfy the CMRR of 0.02 for the translational mode, the difference of translational resonant frequencies must be kept to 0.02 Hz.

Table 4.4: Resonant frequencies of pendulum modes.

Mode	Designed value (assuming uniform mass distribution)	TM1	TM2
Translational	1.29 Hz	1.33 Hz	1.38 Hz
Vertical	40.69 Hz	41.0 Hz	40.8 Hz
Pitch	6.62 Hz	3.91 Hz	3.89 Hz
Roll	0.878 Hz	0.969 Hz	0.938 Hz

4.2.3 Selection of monolithic GAS blades

According to [114], the optimum load F on the GAS filter satisfies the following relationship:

$$F \propto \frac{d^3 w E}{L^2}, \tag{4.11}$$

where d is the thickness of the blades, w is the width at the edge of the blades, E is Young's modulus of the blade material, and L is the length of the blades. Since there were no previous studies using stainless steel for springs, SUS304-CSP, for blades, we fabricated several blades with various widths and thicknesses and measured the optimum load. Fig.

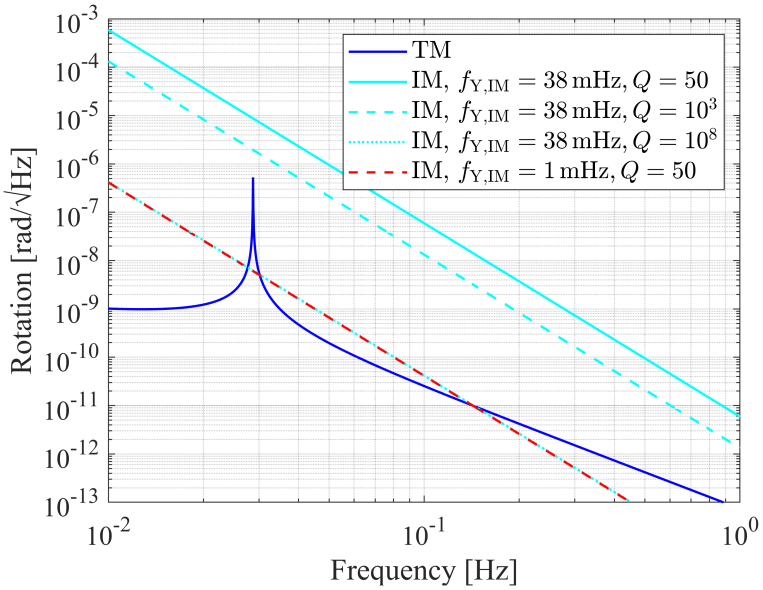

Figure 4.6: Suspension thermal noise from the damped IM. The blue line shows design sensitivity of thermal noise by the suspension wire of TM. The cyan and red lines represent thermal noise by the damped IM with various torsional resonant frequencies and Q factors.

4.8 shows the measurement results. Fig. 4.8 (right) shows the optimum load with a fixed thickness of 0.7 mm and varying widths, while Fig. 4.8 (left) shows the optimum load with a fixed width of 10 mm and varying thicknesses. The length of the blades was set to 88 mm because it is the maximum to install the vacuum chamber of Phase-III TOBA. Here, the optimum load was defined as follows: when the distance from the center ring of the blades to the clamp at the edge of the blades is defined as 1, the height at the optimal working point is approximately 0.06 above the clamp point [114]. Error bars were plotted using the load that resulted in a center ring height of ±2 mm from the optimal working point. We confirmed that the relationship in Eq. (4.11) generally holds by fitting. Based on the results in Fig. 4.8, we decided to use the blades listed in Table 4.5 for the main chain with a load of 10.1 kg and the damping magnet chain with a load of 3.6 kg.

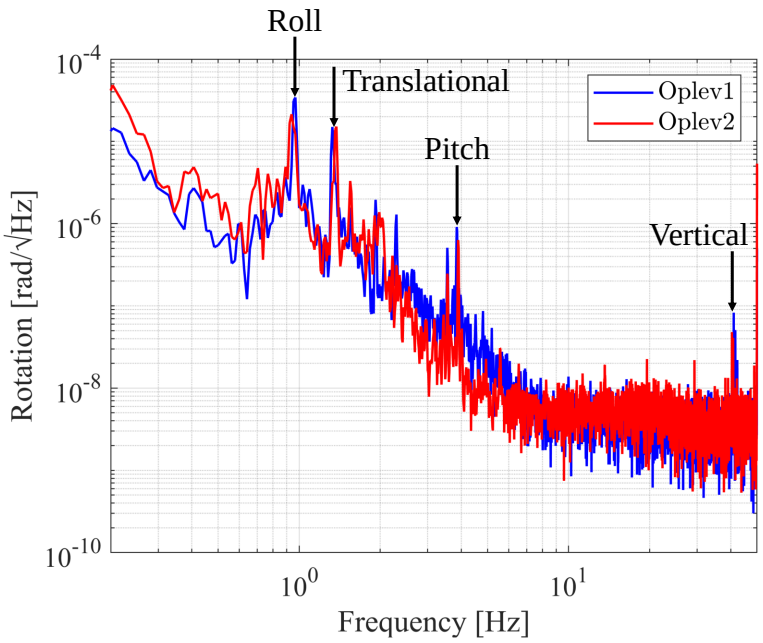

Figure 4.7: Spectra of the optical levers for pendulum modes measurement.

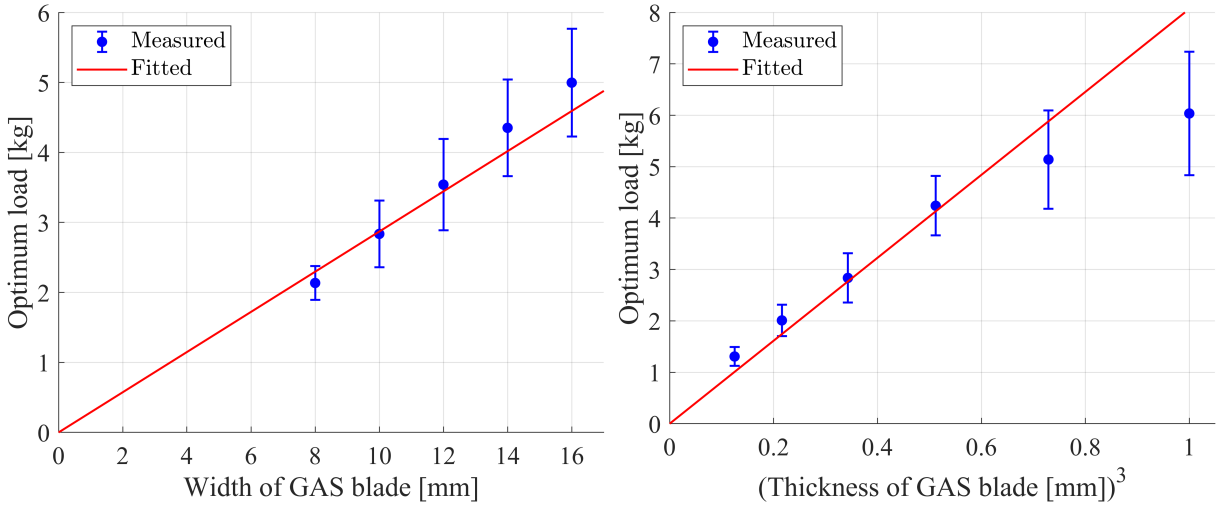

Figure 4.8: Optimum load on the GAS filter for various blade widths and thicknesses. The blue dots represent the measured data, and the red line indicates the fitting result. Left: optimum load at different widths with a fixed thickness of 0.7 mm. Right: optimum load at different thicknesses with a fixed width of 10 mm. Note that the x-axis is the cube of the width.

Table 4.5: Parameters of the GAS filters.

Parameter	Main chain	Damping magnet chain
Load	10.1 kg	3.6 kg
Material of the blades [1]	SUS304-CSP H	SUS304-CSP 3/4H
Length of the blades	88 mm	88 mm
Width of the blades	12 mm	14 mm
Thickness of the blades	1.0 mm	0.7 mm
Vertical resonant frequency	4.48 Hz	$\sim$ 3 Hz

4.2.4 Resonant frequency of GAS filter

The realized vertical resonant frequencies are listed in Table 4.5. The resonant frequencies were measured by exciting the GAS filter from above by hand. For the main chain, the frequencies were measured using the optical lever. The spectra are shown in Fig. 4.9. We suspended the main chain with monolithic GAS blades of two different widths to confirm that the peaks shifted, as it was difficult to identify the resonant frequency of the GAS filter due to many other resonant peaks of pendulum modes. For the damping magnet chain, the frequency was measured visually and with a stopwatch, as there was no sensor available to measure it.

The reason the main chain has a higher resonant frequency than the damping magnet chain is likely due to the heavier load, which caused the system to deviate from linearity of Fig. 4.8, resulting in a load exceeding the optimal value. While the significant difference in resonant frequencies led to a reduction in the Q factor and to be beneficial for damping, it is more desirable from the sensitivity perspective for the main chain's frequency to be even lower. In this setup, no fine tuning of the load was performed. However, when further sensitivity is pursued in the future, it is recommended that a slightly smaller load than designed be applied to the GAS filter first, and then the load be fine-tuned by adding weights little by little to lower the resonance frequency. In larger systems than this experiment, a resonant frequency of 0.2 Hz has been achieved. However, with the blade length used in this experiment, it is expected that the reduction is limited to around 1 Hz.

4.2.5 Effectiveness of GAS filter

The GAS filter was fixed with screws to deactivate it, and the rotational measurement was conducted using optical levers. The sensitivity and the coherence with seismic noise are shown in Fig. 4.10. The effect of the GAS filter was significantly confirmed. Below 0.9 Hz, when the GAS filter was fixed, the sensitivity worsened. Additionally, between 0.1 Hz and 0.5 Hz, the coherence with vertical seismic noise increased. Since the frequency range of 0.1 Hz to 0.5 Hz is below the resonant frequency of the GAS filter, it is believed

[1] According to Ono-Denki Seisakusho, the company that produced the monolithic GAS blades, SUS304-CSP 3/4H was used for thicknesses of 0.5 mm–1.0 mm, and SUS304-CSP H, which is more springy than 3/4H, was used for thicknesses of 1.0 mm–2.0 mm.

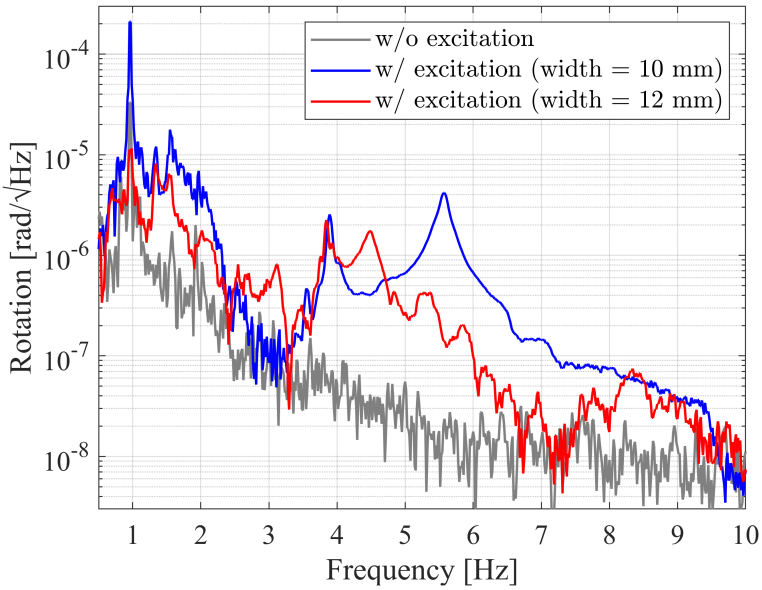

Figure 4.9: Spectra of the optical lever (Oplev1, Pitch) during GAS filter excitation. The gray line represents the spectra without excitation, while the blue and red lines show the spectra with GAS filter excitation using blade widths of 10 mm and 12 mm, respectively. The resonant peaks at 5.57 Hz and 4.48 Hz correspond to the vertical modes induced by the GAS filter.

that fixing the GAS filter caused a tilt of the suspension point, worsening the coupling from seismic noise. Moreover, between 40 Hz and 50 Hz, the coherence with translational and vertical seismic noise increased. As seen in Fig. 4.17, seismic noise is particularly noisy in this frequency range. Since 40 Hz–50 Hz is above the resonant frequency of the GAS filter, it is believed that the loss of passive vibration isolation provided by the GAS filter allowed vibration noise to mix in, increasing the coherence.

4.3 Efficiency of coil-coil actuator

Rotation of the TMs was actively damped by using coil-coil actuators to measure the efficiency of coil-coil actuators. The measured rotational signal by Oplev1 is filtered and then fed back to the coil-coil actuators. This is a kind of feedback control, while the open-loop gain exceeds 1 only around the resonance of the pendulum. The open-loop transfer function is given by

$$G = S_{\mathrm{oplev}} F A_{\mathrm{coil}} H_{\mathrm{TM}}. \tag{4.12}$$

The efficiency of the optical lever S_{oplev} was calculated by Eq. (3.13) to be 547 V/rad for Oplev1 and 513 V/rad for Oplev2. The phase compensation filter F and the mechanical

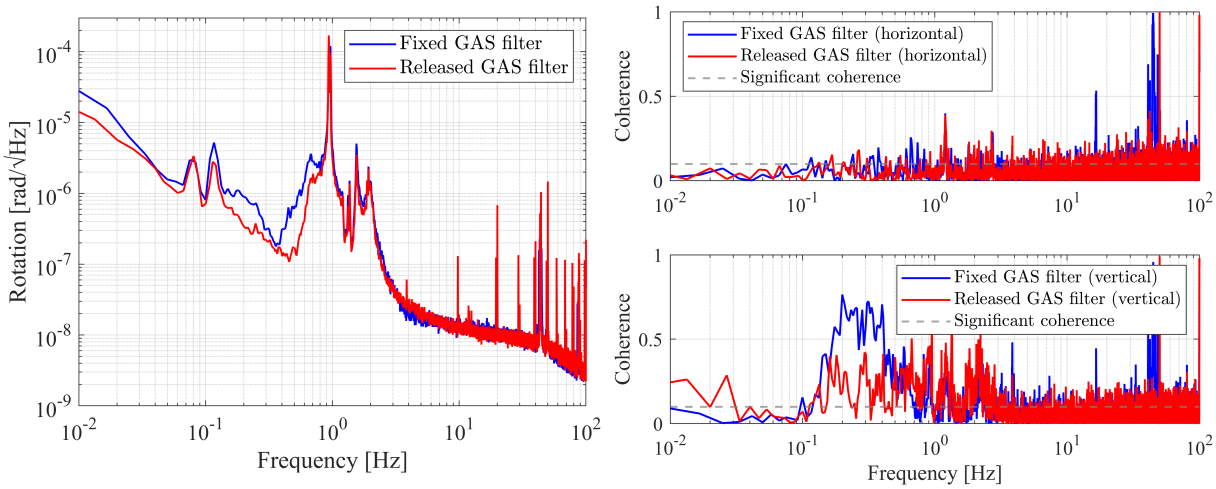

Figure 4.10: Rotation sensitivity and coherence with GAS filter fixed and released. The blue line represents the measured data with GAS filter fixed, and the red line indicates with GAS filter released. The gray dashed line represents the significance coherence [118]. Left panel: differential rotation sensitivity of TM1 and TM2. Right upper panel: coherence between differential rotation sensitivity and horizontal seismic noise. Right lower panel: coherence between differential rotation sensitivity and vertical seismic noise.

response from applied force on the end to rotational angle H_{TM} are

$$F = 180.6 \times \frac{1 + i(f/0.37\,\mathrm{Hz})}{(1 + i(f/25.5\,\mathrm{Hz}))(1 + i(f/196.8\,\mathrm{Hz})^2)}, \tag{4.13}$$

$$H_{\mathrm{TM}} = \frac{D_{\mathrm{coil}}}{4\pi^2 I_{\mathrm{Y}}} \frac{1}{f_0^2 + i f_0 f/Q - f^2} \tag{4.14}$$

where $I_{\mathrm{Y}} = 0.010\,\mathrm{kg\,m^2}$ is given from Table 3.2, and the distance between coil-coil actuators $D_{\mathrm{coil}} = 150\,\mathrm{mm}$. The resonant frequency of Yaw mode, f_0, and the Q factor, Q, were evaluated by ringdown measurement as listed in Table 4.3.

Fig. 4.11 shows the measured open-loop transfer function. The coherence in the upper panel was obtained by 10 times measurements, and the coherence drops around the resonant peak. For fitting, measurement points with coherence larger than 0.95 were used. The red line was fitted with the actuator efficiency A_{coil} as a fitting parameter. The shapes of the measured data well fitted to the theoretical expectation. The fitted actuator efficiency was $3.41 \times 10^{-7}\,\mathrm{N/V}$. The path to locking Fabry-Pérot cavities with the coil-coil actuators is discussed in Section 4.4.

4.4 Path to lock Fabry-Pérot cavities

Using the transmitted light of the Fabry-Pérot cavity for sensing, we discuss the method to lock the cavity on one shoulder of the transmitted light.

The differential length fluctuations of the two cavities should ideally be fed back to the rotational motion of the TMs using the coil-coil actuators. It is preferable to design a

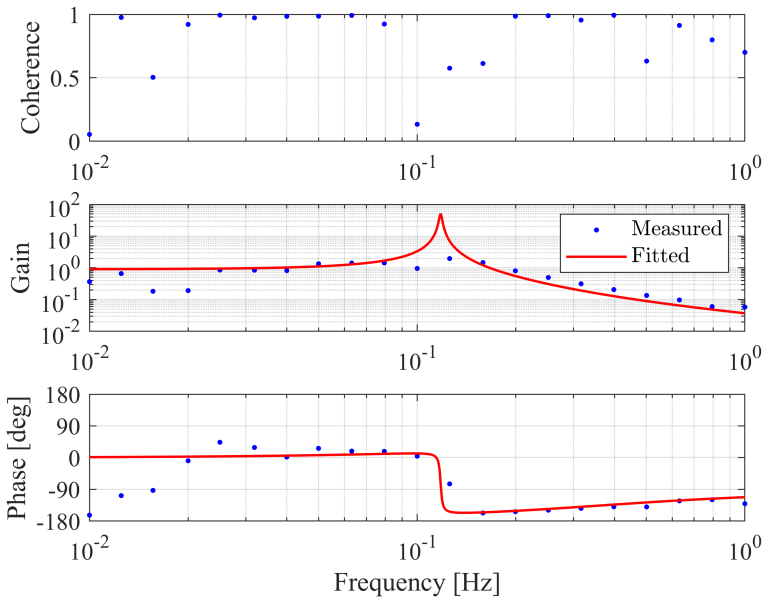

Figure 4.11: Open-loop transfer function of feedback control for Yaw mode. The blue dots are the measured data, and the red line represents the fitted function.

high DC gain to suppress low-frequency fluctuations and realize lock acquisition. On the other hand, common-mode fluctuations should be fed back to the PZT actuator in the laser source via a dual-loop control system. It is beneficial to reduce the DC gain, focus on higher frequencies, increase the unity gain frequency (UGF), and thereby broaden the control bandwidth.

Here, we focus on low-frequency control using the coil-coil actuators. From Fig. 4.4, the amplitude of the transmitted light is approximately 20 mV. Given an FSR of $\lambda/2 = 755\,\mathrm{nm}$ and a finesse of ~ 300 from Table 4.1, the half-width at half-maximum (HWHM) is $\sim 1.5\,\mathrm{nm}$. Thus, the sensing efficiency is calculated to be $\sim 1 \times 10^7\,\mathrm{V/m}$. The sensing efficiency, expressed in units of rotation, is $\sim 7 \times 10^5\,\mathrm{rad/m}$, calculated by converting displacement to rotation using the distance between the cavity mirror and the center of the TM, 55 mm. From the auto-scan of the torsion pendulums, a fringe of about 5 FSR was observed. Considering the finesse of the cavity is approximately 300, it can be estimated that a DC gain of around 10^4 is sufficient for locking the cavity. Assuming a typical DC gain of 10^4 required for cavity locking, and using the coil-coil actuator efficiency measured in Section 4.3 and the force-to-rotation conversion for the torsional pendulum, the necessary DC gain for the filter is calculated to be $\sim 1.5 \times 10^3$. Although this value is not unachievable, even an offset of 1 mV would amplify to 1.5 V, so reducing it by 1–2 orders of magnitude is desirable.

To address this, both sensing efficiency and actuator efficiency need to be improved. The sensing efficiency can be increased by enhancing the transimpedance of the photodetector for transmitted light. Currently, a $500\,\Omega$ resistor is used, so it should be replaced with one approximately 100 times larger. The efficiency of the coil-coil actuator can be increased by reducing the distance between the two facing coils, The distance between

the coils is currently 2.9 mm to avoid contact, but it could be reduced to as close as 1.0 mm. This can be achieved by redesigning the wings and supports holding the coils. These improvements are expected to enable cavity locking and detection of the torsional pendulum's rotational motion.

4.5 Achieved sensitivity

Fig. 4.12 shows the achieved sensitivity with optical levers in unit of rotation rad/$\sqrt{\text{Hz}}$. The blue and cyan lines are the rotation of the TMs obtained by optical levers, and the red line is the result of subtracting them. The sensitivity is improved by about one order of magnitude at DC–0.6 Hz and 2 Hz–5 Hz by common-mode rejection. Fig. 4.13 shows the coherence of TM1 and TM2, and the coherence of TM1 and the differential signal. Before subtraction, there was a significant correlation at DC–0.6 Hz and 2 Hz–10 Hz, but the subtraction reduced the correlation. After subtraction, TM1 and the differential signals were still correlated in 1 Hz–2 Hz.

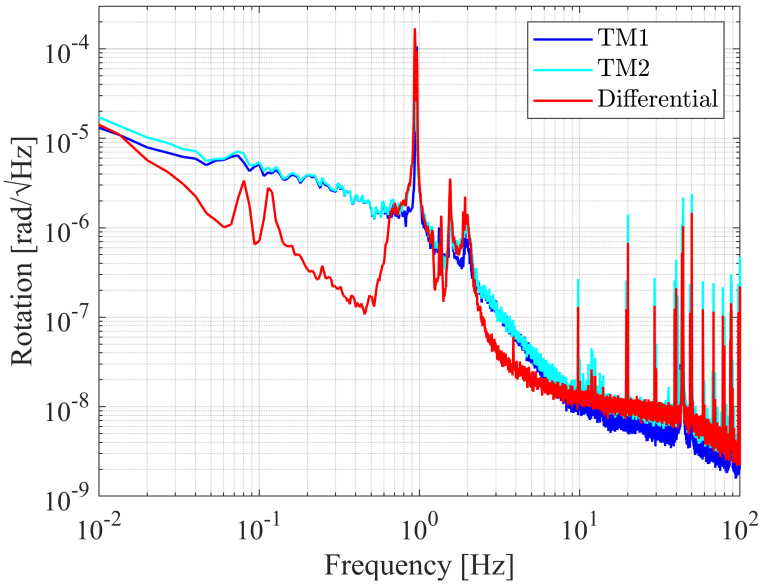

Figure 4.12: Rotation sensitivity of TM1 (blue line), TM2 (cyan line), and the differential (red line).

Fig. 4.14 shows a comparison of sensitivity in units of strain. The sensitivity achieved in this experiment is better than the sensitivity obtained in the previous research on the cryogenic torsion pendulum of Phase-III TOBA at frequencies above 0.1 Hz. Additionally, the sensitivity estimated by assuming the parameters obtained from evaluating this experimental setup and rotational detection with the differential Fabry-Pérot cavity is better than the TorPeDO prototype in the frequency range from 0.1 Hz to 1 Hz, making it the world's best sensitivity for a torsion pendulum-based gravity gradiometer. The noise budget of the estimated sensitivity of this work is plotted in Fig. 4.15.

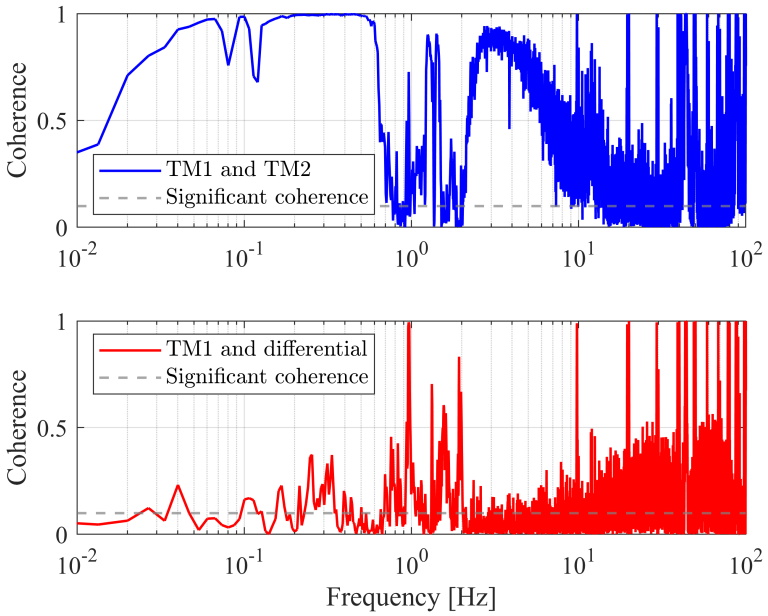

Figure 4.13: Coherence between TM1 and TM2 (upper panel), and TM1 and the differential (lower panel). The gray dashed line represents the significance coherence [118].

4.6 Noise investigation

4.6.1 Dark noise of optical levers

The laser injection on the optical lever was turned off, and the dark noise of the QPD and data logger was measured. Calibration same as that in Fig. 4.12 was performed for the dark noise of Oplev1 and Oplev2, and the contribution of dark noise to the sensitivity was determined. From the results shown in Fig. 4.16, it was found that above 4 Hz, the sensing noise of the optical lever is dominant. This suggests that replacing from the optical lever to the cavity could improve sensitivity.

4.6.2 Coherence with seismic noise

We monitored the horizontal and vertical seismic noise during the measurement for Fig. 4.12. The displacement sensitivity of horizontal and vertical seismic noise were shown in Fig. 4.17. The coherence was calculated between seismic noise and rotation signal detected with the optical levers. The coherence with horizontal seismic noise is shown in Fig. 4.18 (left), and the coherence with vertical seismic noise is shown in Fig. 4.18 (right). The coherence with TM1 is shown in the upper panel and the coherence with the differential signal is shown in the lower panel, respectively. For the horizontal direction, there was little coherence before subtraction, but after subtraction, a significant correlation peak at 1.2 Hz was revealed. It is thought that the slight difference in resonant frequencies of the translational mode between TM1 and TM2 caused coupling with the horizontal seismic noise. For the vertical direction, significant coherence was observed in

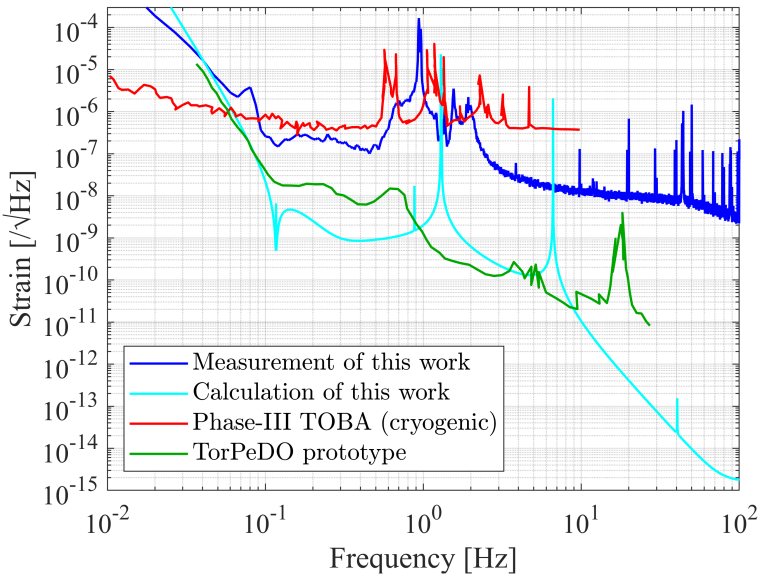

Figure 4.14: Comparison of the sensitivity of this work with previous studies. The blue, red, and green lines represent the achieved sensitivity of this work, the cryogenic torsion pendulum for Phase-III TOBA [105], and the TorPeDO prototype [64], respectively. The cyan line is the estimated sensitivity assuming the parameters of this experimental setup and rotational detection with the differential Fabry-Pérot cavity.

0.6 Hz–2 Hz for the upper panel and in 0.1 Hz–2 Hz for the lower panel. It is believed that there was coupling noise with vertical seismic noise, and other noise could be subtracted by common-mode rejection. The coupling noise is expected to persist even if the rotational detection is replaced with a differential Fabry-Perot cavity. To reduce the noise, it is necessary to decrease the tilt of the TMs, reduce the tilt of the mirrors, and lower the resonant frequency of the GAS filter.

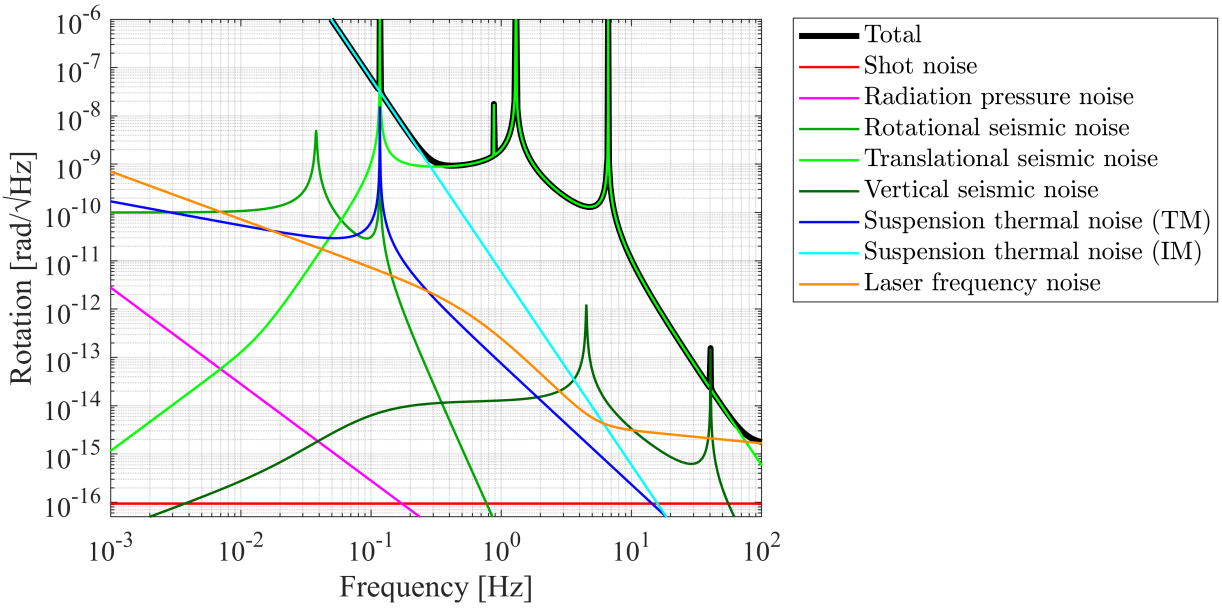

Figure 4.15: The estimated sensitivity assuming the parameters of this work and detection with the differential Fabry-Pérot cavity. The black line represents the total sensitivity, and other colored lines show the noise budget.

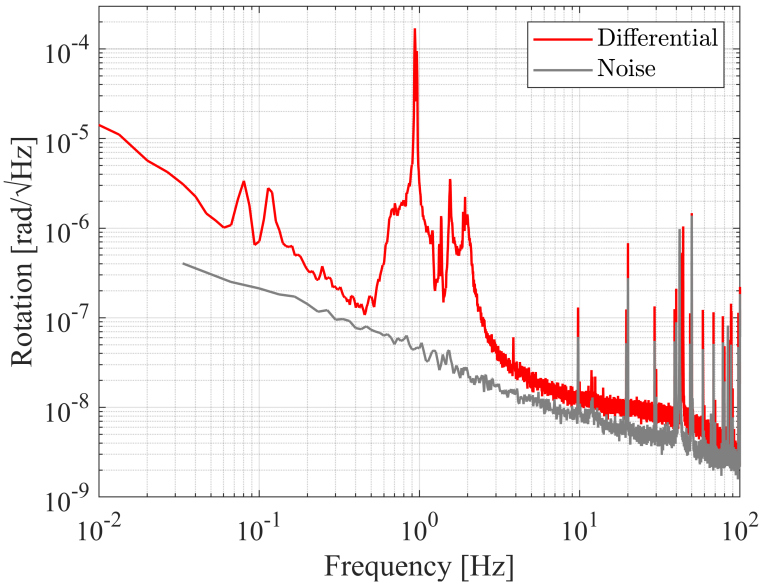

Figure 4.16: Contribution of dark noise of optical levers (gray line). The dark noise limits the sensitivity above 4 Hz.

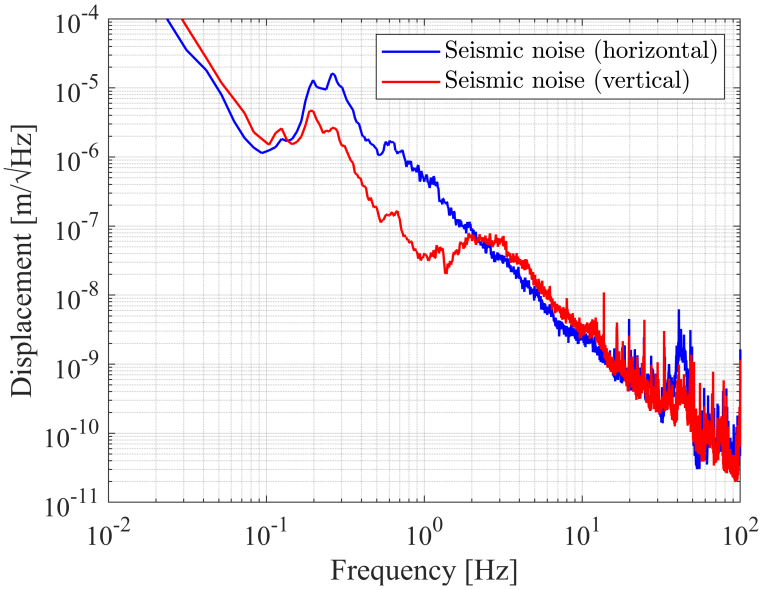

Figure 4.17: Displacement sensitivity of horizontal (blue) and vertical (red) seismic noise.

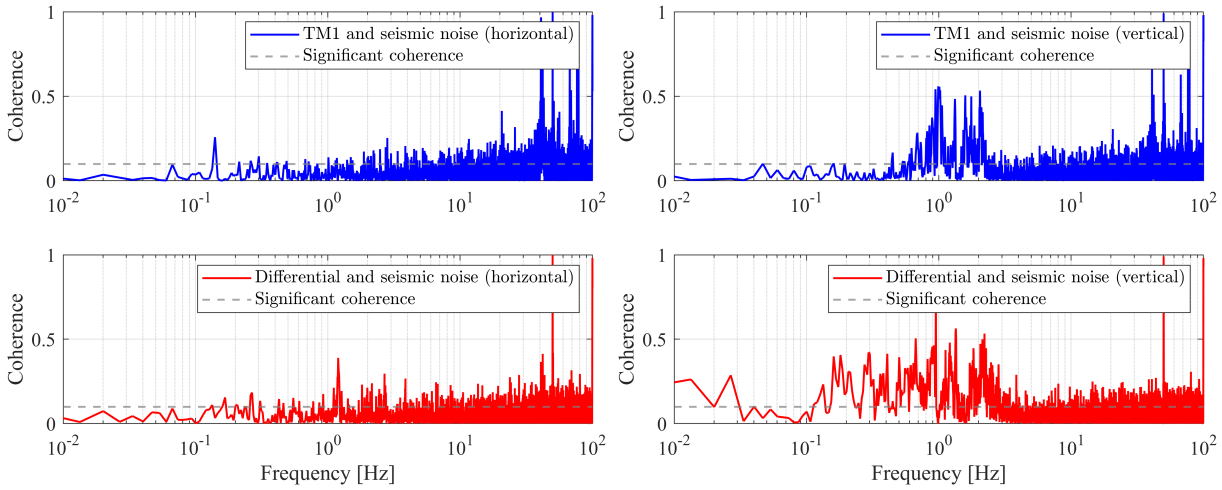

Figure 4.18: Coherence between the rotation signal and seismic noise. Left: coherence with horizontal seismic noise. Right: coherence with vertical seismic noise. The coherence with TM1 is shown in the upper panel and the coherence with the differential signal is shown in the lower panel, respectively. The gray dashed line represents the significance coherence [118].

5 Conclusion

This work successfully designed and developed the optical and suspension system for Phase-III TOBA. In Section 5.1 we briefly summarize the achievement in this thesis. Next in Section 5.2 we discuss the future plan for the improvement of the sensitivity, and this thesis is concluded in Section 5.3.

5.1 Summary

This study focuses on the design and development of the optical and suspension systems for Phase-III TOBA. By improving the previous design, we aim to construct the experimental setup to achieve the target sensitivity of 6.6×10^{-9} rad/$\sqrt{\text{Hz}}$ at 0.1 Hz and 4.6×10^{-9} rad/$\sqrt{\text{Hz}}$ at 0.5 Hz and it is limited by suspension thermal noise and translational seismic noise.

Specifically, for the optical system, we installed a differential Fabry-Pérot cavity for highly sensitive measurements. Optical levers were also included as auxiliary sensors.

For the suspension system, we designed the torsion pendulum with silicon specifications, which has excellent low-temperature characteristics. The design allows the TM to be replaced with silicon coated with mirror coatings. To reduce translational seismic noise, two torsion pendulums were employed, with their centers of mass aligned and the distance between the two suspension points shortened. This configuration can achieve a good CMRR between the two torsion pendulums. A passive vertical vibration isolation mechanism, GAS filter, was installed in the suspension chain for the first time in TOBA to reduce coupling from vertical seismic noise. The GAS filter blades were made of inexpensive, readily available spring stainless steel. To prevent vibrations of the OB from contributing as noise, the OB and the TMs were suspended on the same suspension chain. This design enables direct detection of the differential rotation between the two TMs without relying on the OB. Furthermore, the suspension chain was specifically designed for easy installation into the vacuum chamber and cryocooler of Phase-III TOBA, toward future cryogenic implementation.

We successfully constructed and evaluated the device that combines the optical and suspension systems. The important results are summarized in Table 5.1.

The mode-matching ratios and finesses of the Fabry-Pérot cavities were evaluated, and sufficiently large values $> 99.0\%$ were obtained for the mode-matching ratios within the OB constraints. The measured finesses for Caivity1 and 2 were significantly smaller than the designed finesse due to light loss, but in terms of shot noise levels, these values are acceptable.

The suspension system was also evaluated. The resonant frequency and Q factor of the torsional mode were measured under atmospheric pressure and vacuum using the ringdown method. The resonant frequencies were about three times higher than the design value. This is thought to be due to the increased restoring force caused by the wires of the coil-coil actuators, and two candidates for future actuating methods were presented. The Q factors were almost the same under atmospheric pressure and vacuum, indicating that eddy current damping is working well. Measurements were also taken for the frequencies of other resonant modes. The horizontal resonant frequency was slightly lower than the designed value due to the lowered center of mass caused by the many components attached to the TM. The measured resonant frequency in the vertical direction agreed with the designed value with good accuracy.

For the GAS filters, stainless steel for springs, SUS304-CSP, which has never been used before, was used in this work. In addition, the load was smaller than in previous studies, so monolithic GAS blades with various widths and thicknesses were fabricated, starting with the selection of them. The main chain and damping magnet chain were successfully suspended, and a vertical resonant frequencies of 3 Hz–4.5 Hz were achieved. The GAS filter was fixed with screws to deactivate it, and the effect of the GAS filter was significantly confirmed. Fine tuning of the load is necessary to further decrease the resonant frequency and improve the sensitivity.

The rotational sensitivity was measured using optical levers. By subtracting the signals of Oplev1 and 2 for common-mode rejection, we succeeded in improving the sensitivity by about one order of magnitude at DC–0.6 Hz and 2 Hz–5 Hz by common-mode rejection analysis. The obtained sensitivity was 1.1×10^{-7} rad/$\sqrt{\text{Hz}}$ at 0.4 Hz. Reduction of seismic noise by tuning of the balance weights and actuating in the Pitch and Roll directions are needed to improve the sensitivity.

To measure the efficiency of coil-coil actuators, rotation of the TMs was actively damped by using coil-coil actuators. We discussed the path to lock Fabry-Pérot cavities on one shoulder of the transmitted light by improving sensing efficiency and actuator efficiency. This improvement will lead to lock the Fabry-Pérot cavity and detect rotation.

Table 5.1: Summary of the results.

Parameter	Result of this work	Target of this work	Target of Phase-III TOBA
TM			
Length	30 cm	30 cm	35 cm
Material	Aluminum (silicon specification design)	Aluminum (silicon specification design)	Silicon
Optical system			
Finesse of Fabry-Pérot cavity	~ 300	300	50
Fabry-Pérot cavity locking	Evaluated but unlocked, detection with optical levers	Lock	Lock
Suspension system			
Torsional resonant frequency	117 mHz	39.2 mHz	7.7 mHz
Q factor	~ 50	1×10^3	1×10^8
Tilt angle of TM	$\sim 2 \times 10^{-3}$ rad	1×10^{-5} rad	1×10^{-8} rad
Resonant frequency of GAS filter	3 Hz–4.5 Hz	< 3 Hz	< 3 Hz
Cryogenic system			
Temperature	300 K	300 K	4 K
Sensitivity			
Strain sensitivity at 0.1 Hz	3×10^{-7} $/\sqrt{\text{Hz}}$	1×10^{-8} $/\sqrt{\text{Hz}}$	4×10^{-15} $/\sqrt{\text{Hz}}$

5.2 Future prospects

5.2.1 Cryogenic torsion pendulums made of silicon

Aluminum was used as the material for TMs in this work, but silicon will be used as the material for TMs in the next step because silicon has good properties at low temperatures. Furthermore, to minimize coupling from translational seismic noise, TMs are directly coated and used as mirrors. Silicon TMs and half-inch mirrors have already been obtained (Fig. 5.1), and mode-match calculations of laser beam width for Fabry-Pérot cavity using silicon mirrors have been completed (Fig. 5.2). The other necessary step toward cooling is to change PDs to cryogenic compatible ones. Since it is difficult to acquire the RF signal of the reflected light for the Pound-Drever-Hall (PDH) method at low temperatures, it would be better to detect the reflected light outside the vacuum chamber with an optical fiber.

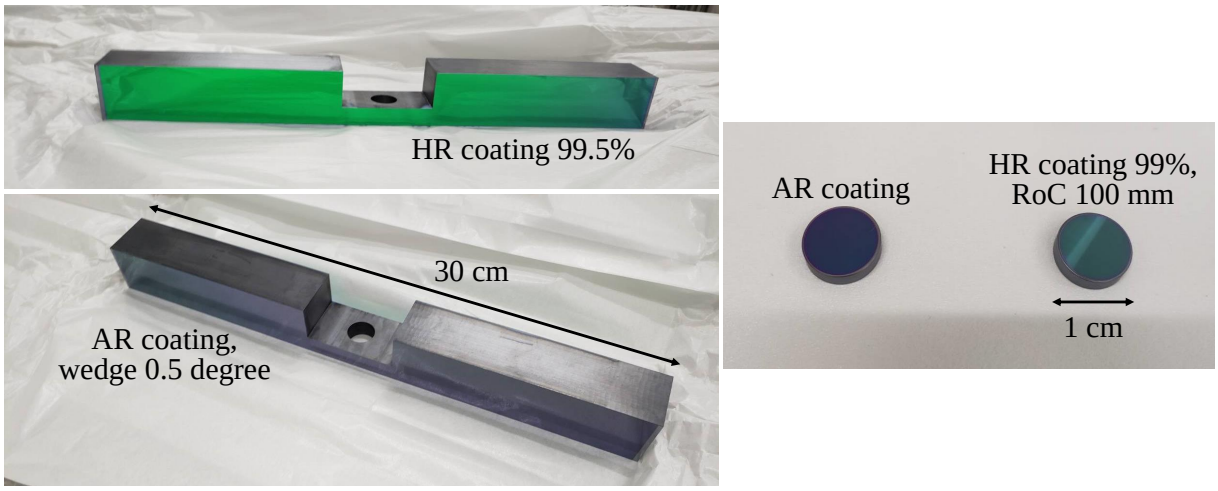

Figure 5.1: Pictures of the TMs (left) and half-inch mirrors (right) made of silicon.

5.2.2 Sensitivity improvement toward realization of Phase-III TOBA

The sensitivity estimated using the parameters obtained from this experiment is shown in the upper-left panel of Fig. 5.3. First, we aim to achieve the design sensitivity of this experiment, shown in the upper-right panel, by locking the Fabry-Perot cavity and performing rotational measurement of the torsion pendulums. Additionally, improvements will be made to the resonant frequency of the torsion pendulums and the tilt of the TMs. To achieve the target sensitivity for Phase-III TOBA, as shown in the lower-left panel, it will be necessary to further reduce suspension wire thermal noise, seismic noise, and laser frequency noise. The key improvements required are summarized in Table 5.2.

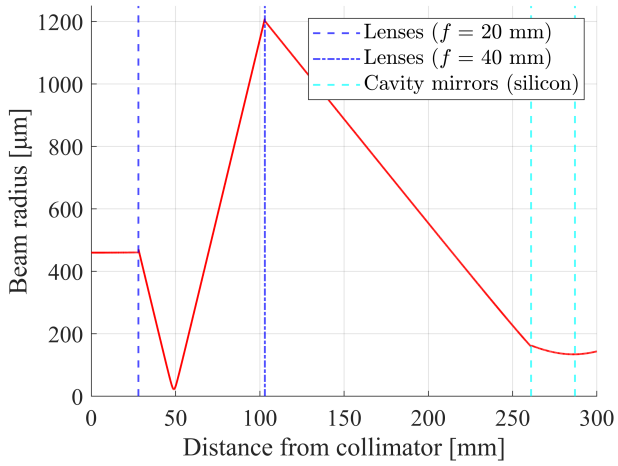

Figure 5.2: Design spatial profile of the beam radius for the Fabry-Pérot cavity with silicon mirrors. The red line indicates the spatial profile of the beam radius. The blue dashed (dash-dotted) line represent the locations of the mode-matching lens with a focal length of 20 mm (40 mm). The cyan dashed lines represent the locations of cavity mirrors made of silicon with a thickness of 3 mm.

5.3 Conclusion

Observations of low-frequency gravity gradients provide us with various important scientific outcomes, such as the detection of GWs from IMBH binary mergers, the modeling of NN by direct detection, and EEW utilizing gravity gradients caused by fault ruptures.

Toward the detection of low-frequency gravity gradients, TOBA has been proposed. TOBA measures the rotational motion of torsion pendulums induced by gravity gradients. By using torsion pendulums with low resonant frequencies, TOBA can observe gravity gradients from 0.1 Hz to 10 Hz. The ultimate goal is a 10 m-scale detector, Final TOBA, with a target sensitivity of 1×10^{-19} $/\sqrt{\mathrm{Hz}}$ at 0.1 Hz. To achieve Final TOBA, a 35 cm-scale prototype Phase-III TOBA is currently under development. The target sensitivity of Phase-III TOBA is set to 1×10^{-15} $/\sqrt{\mathrm{Hz}}$ at 0.1 Hz. Achieving this sensitivity requires reducing quantum noise, seismic noise, and thermal noise. Quantum noise reduction requires a highly sensitive optical system for torsional rotation measurement. Seismic noise reduction requires a suspension system with excellent vibration isolation performance. Thermal noise reduction requires cooling the torsion pendulum.

Previous studies have established the basics for the cooling of torsion pendulums. Additionally, the development of elements for the optical system and suspension system has been conducted. It has been shown that vertical vibration isolation is necessary to reduce seismic noise, and that reducing the vibration of the OB is essential. However, a combined configuration of the optical system for torsional rotation measurement and the suspension system including the torsion pendulum has not yet been established and requires design and development. Therefore, this work focuses on the design and development of the optical and suspension systems for TOBA.

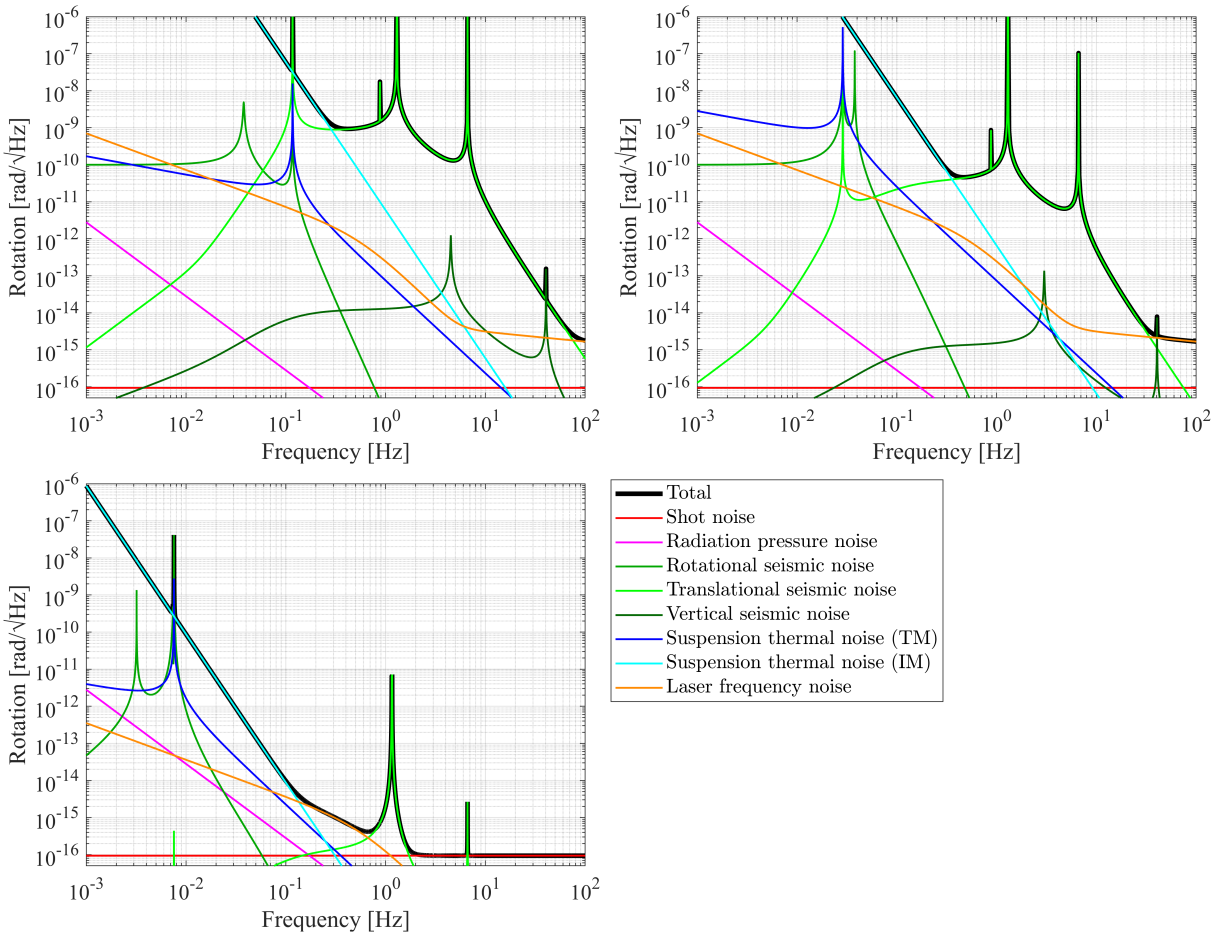

Figure 5.3: Step to improve sensitivity toward Phase-III TOBA. Left upper panel: the estimated sensitivity assuming the parameters of this experimental setup and rotational detection with the differential Fabry-Pérot cavity. Right upper panel: the design sensitivity of this work. Left lower panel: the target sensitivity of Phase-III TOBA. The black line represents the total sensitivity, and other colored lines show the noise budget.

The optical system was designed to include a differential Fabry-Pérot cavity for highly sensitive measurements. This is the first configuration to install a differential Fabry-Pérot cavity into TOBA's torsional rotation measurement. Optical levers were also included as auxiliary sensors.

In the suspension system, this study was conducted with the foresight of using silicon test masses with good properties at low temperatures as the base material for the torsion pendulum in the future. The design was made such that the silicon would not crack when cooled. Additionally, to reduce translational seismic noise, a configuration was proposed where the vibrations of the optical bench do not contribute to the noise. For the first time in TOBA, a GAS filter for passive vertical vibration isolation was introduced, along with the suspension of damping magnets.

We successfully constructed and evaluated the device that combines the optical and

Table 5.2: Parameters to be improved to achieve the target sensitivity of Phase-III TOBA.

Parameter	Value
Suspension thermal noise	
Temperature	4 K
Material of wire	Silicon
Torsional resonant frequency of TM	7.7 mHz
Torsional resonant frequency of TM	3.2 mHz
Q factor	10^8
Translational seismic noise	
Active vibration isolation	1/100
Tilt angle of TM	1×10^{-8} rad
Tilt angle of end mirrors of cavities	1×10^{-6} rad
Laser frequency noise	
Stabilization	1/1000

suspension systems. The measured values were: cavity finesse of 300, torsional resonant frequency of 117 mHz, Q factor of 50, tilt of the TM of 2×10^{-3} rad, and resonant frequency of GAS filter from 3 Hz to 4.5 Hz. Using optical levers, the rotational motion of the torsion pendulums was measured, and the common-mode rejection between the two torsion pendulums was analyzed, achieving a sensitivity of 1.1×10^{-7} rad/$\sqrt{\text{Hz}}$ at 0.4 Hz. This established the fundamental configuration for Phase-III TOBA's optical and suspension systems. Furthermore, the sensitivity estimated by assuming the parameters obtained from the setup and rotational detection with the differential Fabry-Pérot cavity is 1×10^{-9} rad/$\sqrt{\text{Hz}}$ in the range of 0.1 Hz to 1 Hz, making it the world's best sensitivity for a torsion pendulum-type gravity gradiometer.

The abovementioned achievement in the dissertation has opened the path toward achieving the target sensitivity of TOBA and further facilitate the observation of low-frequency gravity gradients using TOBA.

A Development of GAS Filter

In this chapter we describe details of the development of the geometric anti-spring (GAS) filter. In Section A.1 we show the drawings of the monolithic GAS blades, and in Section A.2 the process of constructing the GAS filter is summarized.

A.1 Drawings of monolithic GAS blades

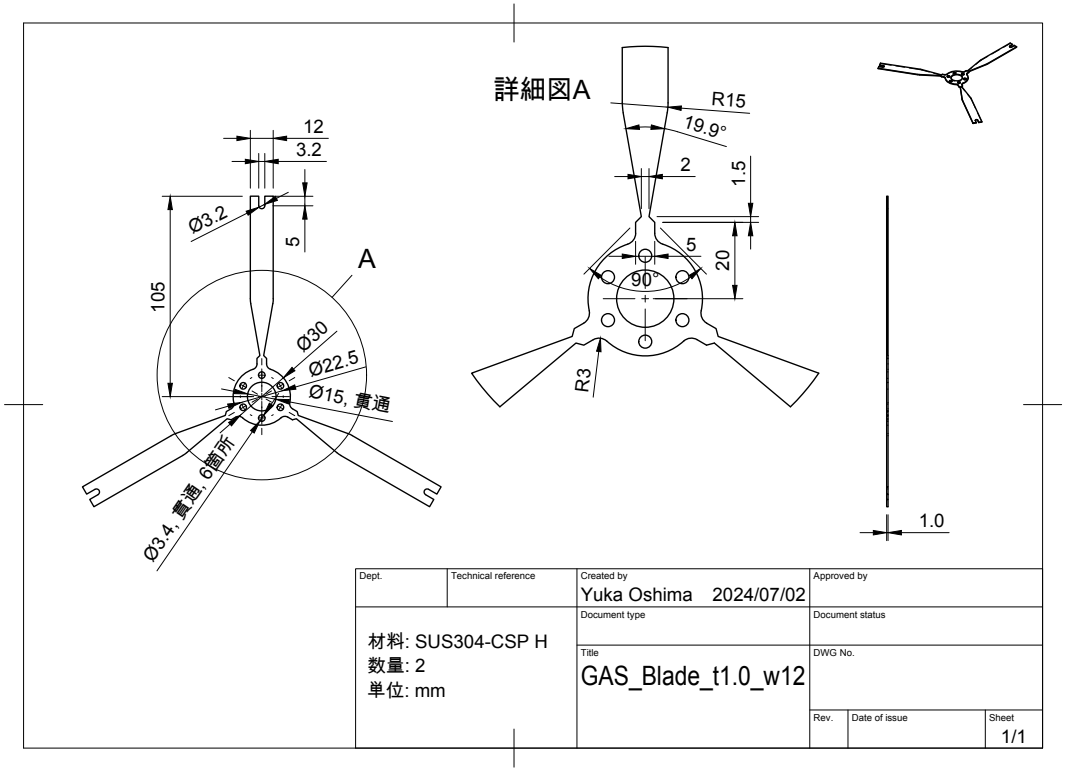

Figure A.1: 2D CAD drawing of the monolithic GAS blades (width = 12 mm, thickness = 1.0 mm).

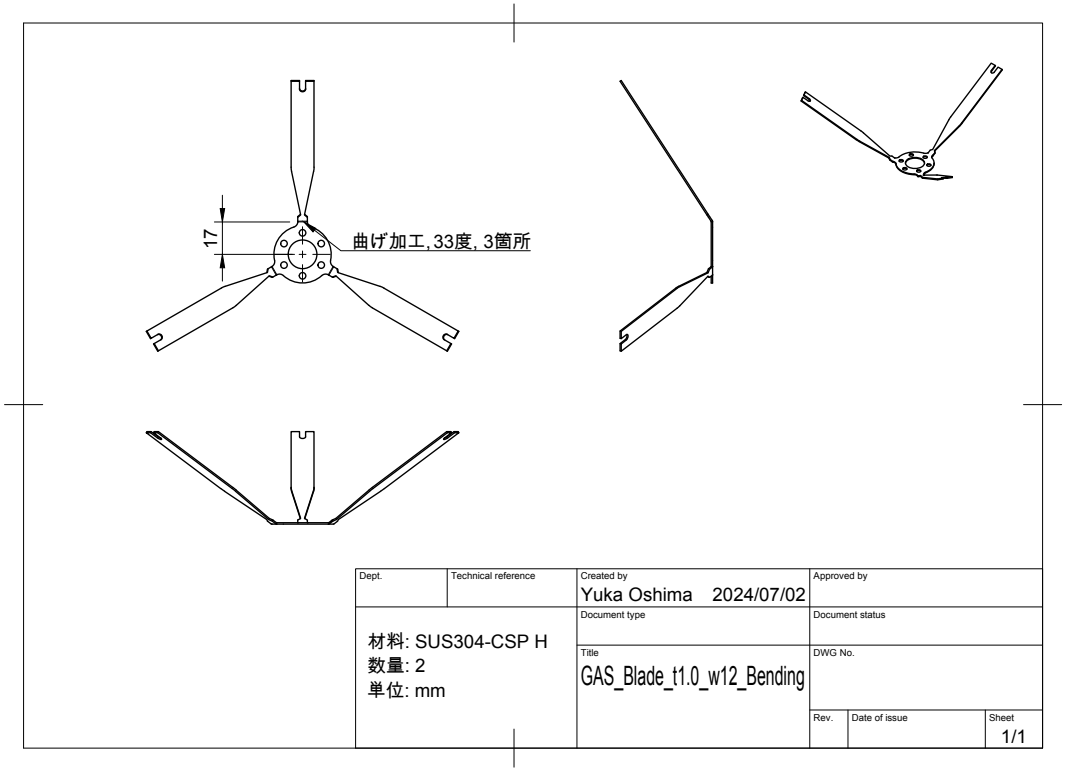

Figure A.2: 2D CAD drawing of bending the monolithic GAS blades.

A.2 Construction of GAS filter

The process of constructing the GAS filter is summarized step-by-step.

1. Fix the monolithic GAS blades to the stopper by sandwiching with screws and nuts from above and below (Fig. A.3). It is important to fix the blades to the stopper at approximately the same height as the optimal working point. When the distance from the center ring of the blades to the clamp at the edge of the blades is defined as 1, the height as the optimal working point is approximately 0.06 above the clamp point [114].

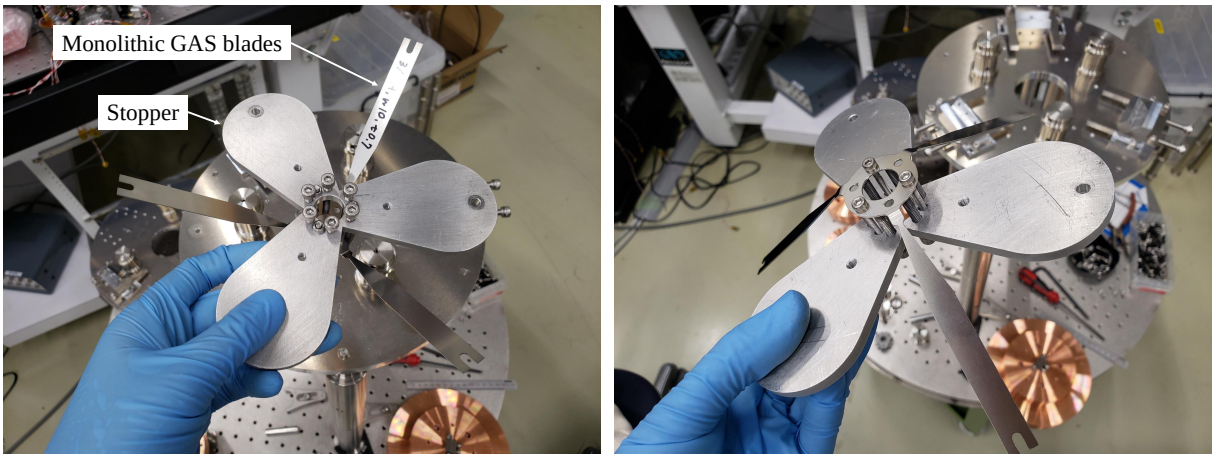

Figure A.3: Pictures of fixing the monolithic GAS blades to the stopper.

2. Bend the monolithic GAS blades and tighten clamps with screws (Fig. A.4). Tighten the three clamps evenly and slightly.

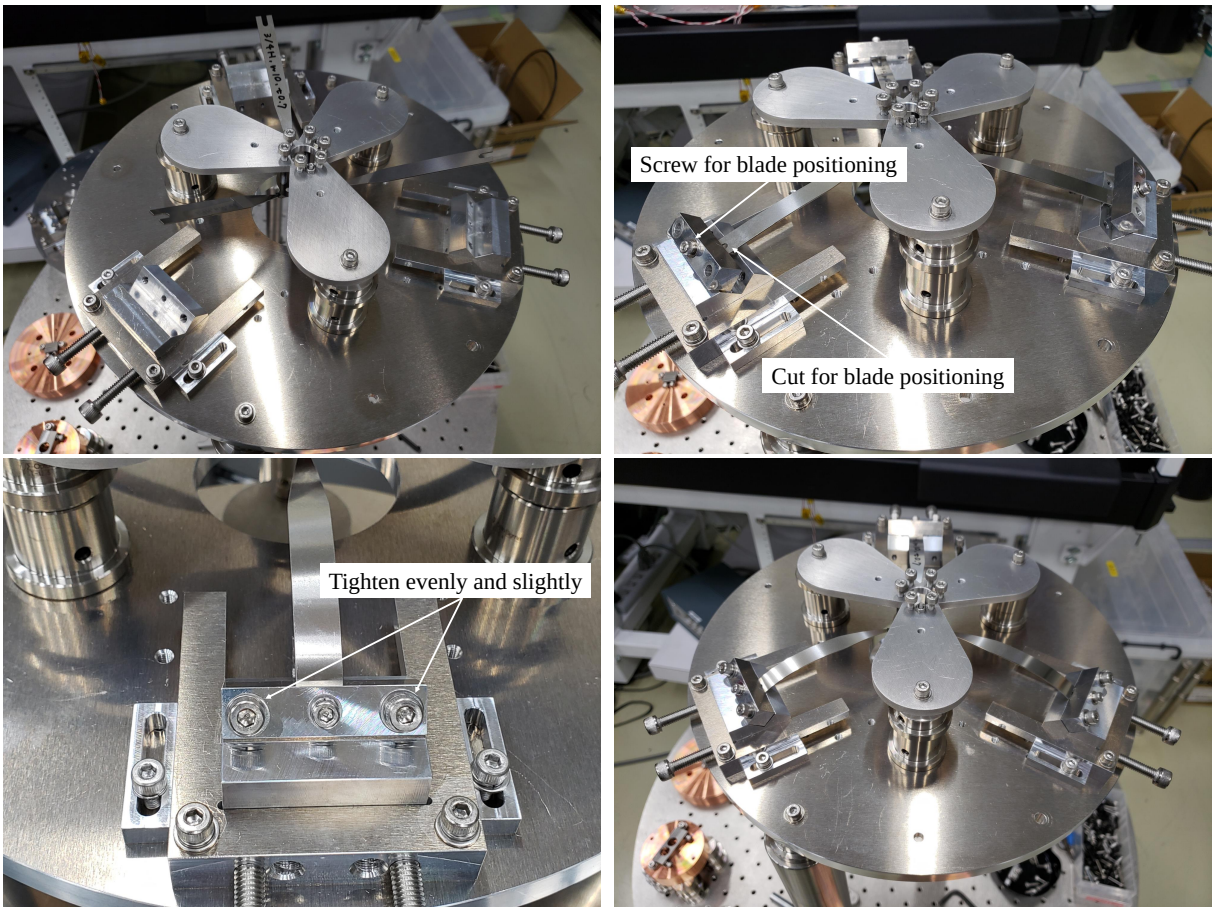

Figure A.4: Pictures of bending the monolithic GAS blades and tightening clamps.

3. Disconnect the monolithic GAS blades from the stopper (Fig. A.5).

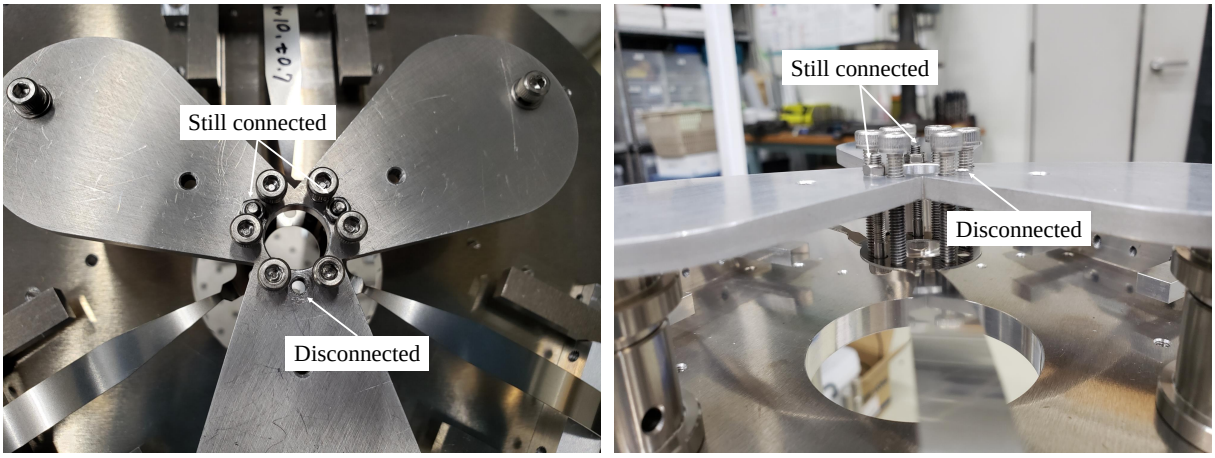

Figure A.5: Pictures of disconnecting the monolithic GAS blades from the stopper.

4. Put the clamp of suspension chain on the monolithic GAS blades (Fig. A.6).

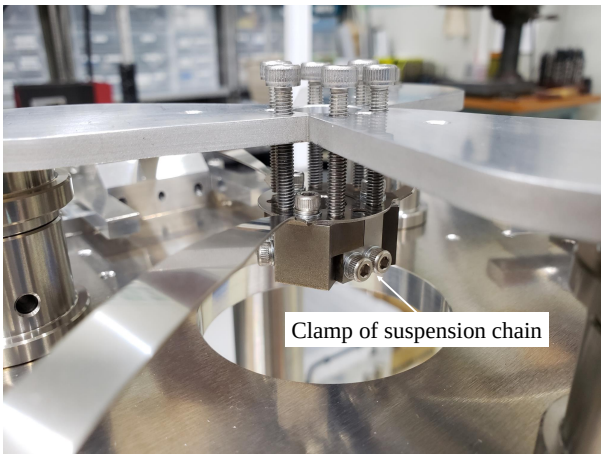

Figure A.6: Picture of putting the clamp of the suspension chain on the monolithic GAS blades.

5. Apply load until the monolithic GAS blades do not touch the stopper screws (Fig. A.7).

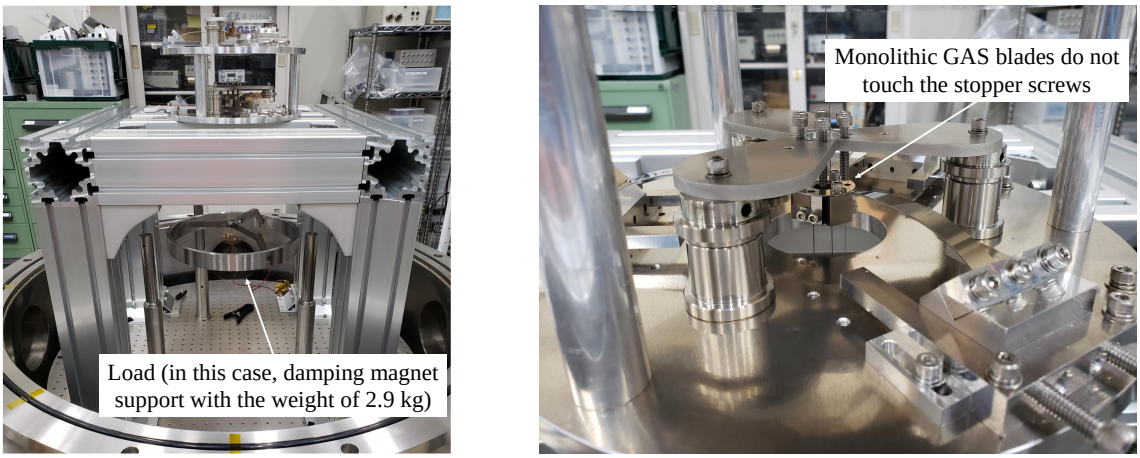

Figure A.7: Pictures of applying load for the monolithic GAS blades.

6. Push the GAS clamps with tuning screws until the vertical resonant frequency minimizes (Fig. A.8).

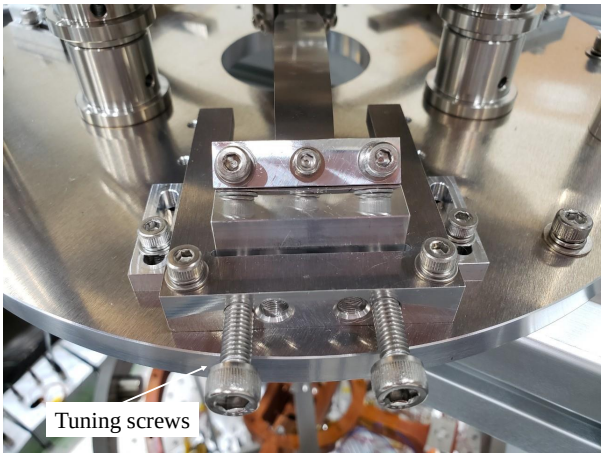

Figure A.8: Picture of pushing the GAS clamps with tuning screws.

B List of Devices

In this chapter, the lists of devices used in the experiment are summarized.

Table B.1: List of Laser and optics.

Device	Manufacturer	Model number
Laser (1550 nm)	NKT Photonics	Koheras AdjustiK E15
Laser (1064 nm)	COHERENT	Mephisto 500NE
Fiber isolator	HaphiT	FPIS-1550-DS-2L10-FC/APC
Fiber EOM	EOSPACE	PM-0K5-00-PFA-PFA-UL-S
Fiber polarizer	Thorlabs	ILP1550PM-APC
Optical fiber (1064 nm)	Thorlabs	P3-1064PMY-1
Fiber coupler (1550 nm)	Thorlabs	PN1550R5A1
Fiber coupler (1064 nm)	Thorlabs	PN1064R5A1
Fiber collimator (1550 nm)	Thorlabs	CFP5-1550A
Fiber collimator (1064 nm)	Thorlabs	CFP5-1064A

Table B.2: List of optics on the OB.

Device	Manufacturer	Model number
Mirror (1550 nm)	Thorlabs	BB05-E04
Mirror (1064 nm)	Thorlabs	BB05-E03
Beam splitter (1550 nm)	Thorlabs	BS012
Beam splitter (1064 nm)	Thorlabs	BS011
Lens	Thorlabs	LB1014-C
Cavity mirror	Lattice Electro Optics	Custom order
Single PD	Hamamatsu Photonics	G10899-003K
QPD	Hamamatsu Photonics	G6849
Beam dump	ANSOKEN	DIC8616UJ
PZT drive motor	Newport	8301NF
Coil	Serco	Custom order
TM made of silicon	SIGMAKOKI	Custom order
Mirror made of silicon	SIGMAKOKI	Custom order

Table B.3: List of vacuum-related components.

Device	Manufacturer	Model number
Vacuum pump	Kashiyama Industries	NeoDry30E
Vacuum gauge	Canon Anelva	M-336MX
Vacuum gauge controller	Canon Anelva	M-601GC
Fiber feedthrough (1550 nm)	SQS Vláknová optika	Custom order
Fiber feedthrough (1064 nm)	SQS Vláknová optika	Custom order
Vacuum socket contact	Cosmotec	SAC16
Atmospheric socket contacts	Cosmotec	SVC16
Vacuum insulation insert	Cosmotec	VSPI22GA
Flange with LEMO terminals	Cosmotec	Custom order
Conversion flange	Cosmo Science	Custom order (JIS150VF/NW40×2)

Table B.4: List of vacuum-related components.

Device	Manufacturer	Model number
TM, IM, OB, clamp, etc.	Ono-Denki Seisakusho	Custom order
Holder for optics	Ono-Denki Seisakusho	Custom order
Monolithic GAS blades	Ono-Denki Seisakusho	Custom order
Wire	Nilaco	Seisakusho order
Handle for IM	MiSUMi	A-1080-4
Frame	MiSUMi	GNFS8-100100-400/465/600
Low-head screw	MiSUMi	CBSTSR3-10
Stepped screw	MiSUMi	DBS4-8-6
Stepped screw	MiSUMi	DBS4-8-8
Stepped screw	MiSUMi	DBS4-10-8

Table B.5: List of electronics and other components.

Device	Manufacturer	Model number
Beam profiler	Thorlabs	BP209-VIS
Power meter	Thorlabs	S132C
Scope coder	Yokogawa	DL850E
Spectrum analyzer	Onosokki	DS2000
CCD camera	Scintacor	56-567
Display for CCD camera	TOHOTAIYO	TH-TV16TW01
Function generator	Tektronix	AFG3052C
Function generator	Tektronix	AFG3102C
Function generator	Tektronix	AFG31000
Filtered preamplifier	Stanford Research Systems	SR560
PZT motor driver	Newport	8742
PZT motor driver handpad	Newport	8758
Geophone (horizontal)	Sercel	L-22E
Geophone (vertical)	Sercel	L-4C

Bibliography

[1] A. Einstein, "Näherungsweise Integration der Feldgleichungen der Gravitation", Sitzungsberichte der Königlich Preußischen Akademie der Wissenschaften, 688–696 (1916) (cit. on p. 22).

[2] A. Einstein, "Über Gravitationswellen", Sitzungsberichte der Königlich Preußischen Akademie der Wissenschaften, 154–167 (1918) (cit. on p. 22).

[3] B. P. Abbott et al., "Observation of Gravitational Waves from a Binary Black Hole Merger", Phys. Rev. Lett. **116**, 061102 (2016) (cit. on p. 22).

[4] The LIGO Scientific Collaboration et al., "Advanced LIGO", Classical and Quantum Gravity **32**, 074001 (2015) (cit. on pp. 22, 38, 39).

[5] R. Abbott et al., "GWTC-3: Compact Binary Coalescences Observed by LIGO and Virgo during the Second Part of the Third Observing Run", Phys. Rev. X **13**, 041039 (2023) (cit. on p. 22).

[6] R. Abbott et al., "Population of Merging Compact Binaries Inferred Using Gravitational Waves through GWTC-3", Phys. Rev. X **13**, 011048 (2023) (cit. on p. 22).

[7] B. P. Abbott et al., "Gravitational waves and gamma-rays from a binary neutron star merger: gw170817 and grb 170817a", The Astrophysical Journal Letters **848**, L13 (2017) (cit. on p. 22).

[8] B. P. Abbott et al., "Tests of General Relativity with GW150914", Phys. Rev. Lett. **116**, 221101 (2016) (cit. on p. 22).

[9] B. P. Abbott et al., "Tests of General Relativity with GW170817", Phys. Rev. Lett. **123**, 011102 (2019) (cit. on p. 22).

[10] B. P. Abbott et al., "GW170817: Observation of Gravitational Waves from a Binary Neutron Star Inspiral", Phys. Rev. Lett. **119**, 161101 (2017) (cit. on p. 22).

[11] B. P. Abbott et al., "Multi-messenger Observations of a Binary Neutron Star Merger*", The Astrophysical Journal Letters **848**, L12 (2017) (cit. on p. 22).

[12] T. Matsubayashi, H. Shinkai, and T. Ebisuzaki, "Gravitational Waves from Merging Intermediate-Mass Black Holes", The Astrophysical Journal **614**, 864 (2004) (cit. on pp. 22, 30).

[13] B. Allen and J. D. Romano, "Detecting a stochastic background of gravitational radiation: Signal processing strategies and sensitivities", Phys. Rev. D **59**, 102001 (1999) (cit. on p. 22).

[14] T. L. Smith, M. Kamionkowski, and A. Cooray, "Direct detection of the inflationary gravitational-wave background", Phys. Rev. D **73**, 023504 (2006) (cit. on p. 22).

[15] R. A. Hulse and J. H. Taylor, "Discovery of a pulsar in a binary system.", The Astrophysical Journal Letters **195**, L51–L53 (1975) (cit. on p. 29).

[16] K. Jani, D. Shoemaker, and C. Cutler, "Detectability of intermediate-mass black holes in multiband gravitational wave astronomy", Nature Astronomy **4**, 260–265 (2020) (cit. on p. 30).

[17] M. Coleman Miller and E. J. M. Colbert, "INTERMEDIATE-MASS BLACK HOLES", International Journal of Modern Physics D **13**, 1–64 (2004) (cit. on p. 30).

[18] M. S. Fujii, L. Wang, A. Tanikawa, Y. Hirai, and T. R. Saitoh, "Simulations predict intermediate-mass black hole formation in globular clusters", Science **384**, 1488–1492 (2024) (cit. on p. 30).

[19] T. Ebisuzaki et al., "Missing Link Found? The "Runaway" Path to Supermassive Black Holes", The Astrophysical Journal **562**, L19 (2001) (cit. on p. 30).

[20] C. Reisswig, C. D. Ott, E. Abdikamalov, R. Haas, P. Mösta, and E. Schnetter, "Formation and Coalescence of Cosmological Supermassive-Black-Hole Binaries in Supermassive-Star Collapse", Phys. Rev. Lett. **111**, 151101 (2013) (cit. on p. 30).

[21] R. Abbott et al., "Properties and Astrophysical Implications of the 150 $M_\odot$ Binary Black Hole Merger GW190521", The Astrophysical Journal Letters **900**, L13 (2020) (cit. on p. 30).

[22] R. Abbott et al., "GW190521: A Binary Black Hole Merger with a Total Mass of 150 $M_\odot$", Phys. Rev. Lett. **125**, 101102 (2020) (cit. on p. 30).

[23] D. R. Pasham, T. E. Strohmayer, and R. F. Mushotzky, "A 400-solar-mass black hole in the galaxy M82", Nature **513**, 74–76 (2014) (cit. on p. 30).

[24] B. Kızıltan, H. Baumgardt, and A. Loeb, "An intermediate-mass black hole in the centre of the globular cluster 47 Tucanae", Nature **542**, 203–205 (2017) (cit. on p. 30).

[25] S. Takekawa, T. Oka, Y. Iwata, S. Tsujimoto, and M. Nomura, "Indication of Another Intermediate-mass Black Hole in the Galactic Center", The Astrophysical Journal Letters **871**, L1 (2019) (cit. on p. 30).

[26] P. R. Saulson, "Terrestrial gravitational noise on a gravitational wave antenna", Phys. Rev. D **30**, 732–736 (1984) (cit. on pp. 31, 34).

[27] S. A. Hughes and K. S. Thorne, "Seismic gravity-gradient noise in interferometric gravitational-wave detectors", Phys. Rev. D **58**, 122002 (1998) (cit. on p. 34).

[28] K. Somiya and (for the KAGRA Collaboration), "Detector configuration of KAGRA – the Japanese cryogenic gravitational-wave detector", Classical and Quantum Gravity **29**, 124007 (2012) (cit. on pp. 34, 35, 38, 49).

[29] T. Creighton, "Tumbleweeds and airborne gravitational noise sources for LIGO", Classical and Quantum Gravity **25**, 125011 (2008) (cit. on p. 34).

[30] D. Fiorucci, J. Harms, M. Barsuglia, I. Fiori, and F. Paoletti, "Impact of infrasound atmospheric noise on gravity detectors used for astrophysical and geophysical applications", Phys. Rev. D **97**, 062003 (2018) (cit. on pp. 34, 35, 49).

[31] R. Bajpai, T. Tomaru, T. Suzuki, K. Yamamoto, T. Ushiba, and T. Honda, "Estimation of Newtonian noise from the KAGRA cooling system", Phys. Rev. D **107**, 042001 (2023) (cit. on p. 34).

[32] S. Hild et al., "Sensitivity studies for third-generation gravitational wave observatories", Classical and Quantum Gravity **28**, 094013 (2011) (cit. on pp. 34, 35).

[33] B. P. Abbott et al., "Exploring the sensitivity of next generation gravitational wave detectors", Classical and Quantum Gravity **34**, 044001 (2017) (cit. on p. 34).

[34] E. D. Hall, "Cosmic Explorer: A Next-Generation Ground-Based Gravitational-Wave Observatory", Galaxies **10**, 90 (2022) (cit. on pp. 34, 35).

[35] E. D. Hall et al., "Gravitational-wave physics with Cosmic Explorer: Limits to low-frequency sensitivity", Phys. Rev. D **103**, 122004 (2021) (cit. on p. 34).

[36] J. Harms, L. Naticchioni, E. Calloni, R. De Rosa, F. Ricci, and D. D'Urso, "A lower limit for Newtonian-noise models of the Einstein Telescope", The European Physical Journal Plus **137**, 687 (2022) (cit. on p. 34).

[37] J. C. Driggers, J. Harms, and R. X. Adhikari, "Subtraction of Newtonian noise using optimized sensor arrays", Phys. Rev. D **86**, 102001 (2012) (cit. on p. 34).

[38] J. Harms and K. Venkateswara, "Newtonian-noise cancellation in large-scale interferometric GW detectors using seismic tiltmeters", Classical and Quantum Gravity **33**, 234001 (2016) (cit. on p. 34).

[39] J. Harms and S. Hild, "Passive Newtonian noise suppression for gravitational-wave observatories based on shaping of the local topography", Classical and Quantum Gravity **31**, 185011 (2014) (cit. on p. 34).

[40] L. Trozzo and F. Badaracco, "Seismic and Newtonian Noise in the GW Detectors", Galaxies **10**, 20 (2022) (cit. on p. 35).

[41] Y. Imanishi, T. Sato, T. Higashi, W. Sun, and S. Okubo, "A Network of Superconducting Gravimeters Detects Submicrogal Coseismic Gravity Changes", Science **306**, 476–478 (2004) (cit. on p. 34).

[42] S.-C. Han, C. K. Shum, M. Bevis, C. Ji, and C.-Y. Kuo, "Crustal Dilatation Observed by GRACE After the 2004 Sumatra-Andaman Earthquake", Science **313**, 658–662 (2006) (cit. on p. 34).

[43] K. Heki and K. Matsuo, "Coseismic gravity changes of the 2010 earthquake in central Chile from satellite gravimetry", Geophysical Research Letters **37**, L24306 (2010) (cit. on p. 34).

[44] K. Matsuo and K. Heki, "Coseismic gravity changes of the 2011 Tohoku-Oki earthquake from satellite gravimetry", Geophysical Research Letters **38**, L00G12 (2011) (cit. on p. 34).

[45] J. Harms et al., "Transient gravity perturbations induced by earthquake rupture", Geophysical Journal International **201**, 1416–1425 (2015) (cit. on p. 35).

[46] J.-P. Montagner et al., "Prompt gravity signal induced by the 2011 Tohoku-Oki earthquake", Nature Communications **7**, 13349 (2016) (cit. on p. 35).

[47] M. Vallée, J. P. Ampuero, K. Juhel, P. Bernard, J.-P. Montagner, and M. Barsuglia, "Observations and modeling of the elastogravity signals preceding direct seismic waves", Science **358**, 1164–1168 (2017) (cit. on pp. 35–37).

[48] M. Kimura et al., "Earthquake-induced prompt gravity signals identified in dense array data in Japan", Earth, Planets and Space **71**, 27 (2019) (cit. on p. 35).

[49] M. Kimura, N. Kame, S. Watada, A. Araya, T. Kunugi, and R. Wang, "Determination of the source parameters of the 2011 Tohoku-Oki earthquake from three-component pre-P gravity signals recorded by dense arrays in Japan", Earth, Planets and Space **73**, 223 (2021) (cit. on p. 35).

[50] M. Vallée and K. Juhel, "Multiple Observations of the Prompt Elastogravity Signals Heralding Direct Seismic Waves", Journal of Geophysical Research: Solid Earth **124**, 2970–2989 (2019) (cit. on p. 36).

[51] N. Kame and M. Kimura, "The fundamental nature of a transient elastic response to prompt gravity perturbations", Geophysical Journal International **218**, 1136–1142 (2019) (cit. on p. 36).

[52] N. Kame, "Pre-P gravity signals from dynamic earthquake rupture: modelling and observations", Philosophical Transactions of the Royal Society A: Mathematical, Physical and Engineering Sciences **379**, 20200136 (2021) (cit. on p. 36).

[53] K. Juhel et al., "Earthquake Early Warning Using Future Generation Gravity Strainmeters", Journal of Geophysical Research: Solid Earth **123**, 10,889–10,902 (2018) (cit. on pp. 36, 38, 49).

[54] T. Shimoda, K. Juhel, J.-P. Ampuero, J.-P. Montagner, and M. Barsuglia, "Early earthquake detection capabilities of different types of future-generation gravity gradiometers", Geophysical Journal International **224**, 533–542 (2020) (cit. on pp. 36, 49).

[55] F. Acernese et al., "Advanced Virgo: a second-generation interferometric gravitational wave detector", Classical and Quantum Gravity **32**, 024001 (2014) (cit. on p. 38).

[56] H. Grote and (for the LIGO Scientific Collaboration), "The status of GEO 600", Classical and Quantum Gravity **25**, 114043 (2008) (cit. on p. 38).

[57] K. Danzmann and the LISA study team, "LISA: laser interferometer space antenna for gravitational wave measurements", Classical and Quantum Gravity **13**, A247 (1996) (cit. on pp. 39, 42).

[58] S. Sato et al., "The status of DECIGO", Journal of Physics: Conference Series **840**, 012010 (2017) (cit. on pp. 39, 43).

[59] M. Armano et al., "Sub-Femto-g Free Fall for Space-Based Gravitational Wave Observatories: LISA Pathfinder Results", Phys. Rev. Lett. **116**, 231101 (2016) (cit. on pp. 39, 43).

[60] T. Nakamura et al., "Pre-DECIGO can get the smoking gun to decide the astrophysical or cosmological origin of GW150914-like binary black holes", Progress of Theoretical and Experimental Physics **2016**, 093E01 (2016) (cit. on pp. 39, 43).

[61] M. Ando et al., "Torsion-Bar Antenna for Low-Frequency Gravitational-Wave Observations", Phys. Rev. Lett. **105**, 161101 (2010) (cit. on pp. 39, 40, 45, 49–51, 70).

[62] A. Shoda et al., "Ground-based low-frequency gravitational-wave detector with multiple outputs", Phys. Rev. D **95**, 082004 (2017) (cit. on pp. 39, 40, 61, 70).

[63] D. J. McManus et al., "Mechanical characterisation of the TorPeDO: a low frequency gravitational force sensor", Classical and Quantum Gravity **34**, 135002 (2017) (cit. on pp. 39, 40).

[64] S. S. Y. Chua et al., "The torsion pendulum dual oscillator for low-frequency Newtonian noise detection", Applied Physics Letters **122**, 201102 (2023) (cit. on pp. 39, 40, 110).

[65] H. J. Paik et al., "Low-frequency terrestrial tensor gravitational-wave detector", Classical and Quantum Gravity **33**, 075003 (2016) (cit. on pp. 39, 41).

[66] B. Canuel et al., "Exploring gravity with the MIGA large scale atom interferometer", Scientific Reports **8**, 14064 (2018) (cit. on pp. 39, 42).

[67] M.-S. Zhan et al., "ZAIGA: Zhaoshan long-baseline atom interferometer gravitation antenna", International Journal of Modern Physics D **29**, 1940005 (2020) (cit. on pp. 39, 42).

[68] C. Cahillane and G. Mansell, "Review of the Advanced LIGO Gravitational Wave Observatories Leading to Observing Run Four", Galaxies **10**, 36 (2022) (cit. on p. 39).

[69] K. Ishidoshiro et al., "Upper Limit on Gravitational Wave Backgrounds at 0.2 Hz with a Torsion-Bar Antenna", Phys. Rev. Lett. **106**, 161101 (2011) (cit. on pp. 40, 49, 60, 61, 70).

[70] W. Kokuyama, "Spaceborne Rotating Torsion-Bar Antenna for Low-Frequency Gravitational-Wave Observations", https://granite.phys.s.u-tokyo.ac.jp/theses/kokuyama_d.pdf, Ph.D. thesis (The University of Tokyo, 2012) (cit. on pp. 40, 62).

[71] S. Takano et al., "TOrsion-Bar Antenna: A Ground-Based Detector for Low-Frequency Gravity Gradient Measurement", Galaxies **12**, 78 (2024) (cit. on pp. 40, 63, 69).

[72] D. J. McManus, M. J. Yap, R. L. Ward, D. A. Shaddock, D. E. McClelland, and B. J. J. Slagmolen, "TorPeDO: A Low Frequency Gravitational Force Sensor", Journal of Physics: Conference Series **716**, 012027 (2016) (cit. on pp. 40, 41).

[73] A. K. Ramamohan et al., "Characterization of heterodyne optical phase locking for relative laser frequency noise suppression in differential measurement", Opt. Express **32**, 39793–39803 (2024) (cit. on p. 40).

[74] D. J. McManus et al., *Early Earthquake Detection with a Dual Torsion-Beam Gravimeter*, 2018, arXiv:1809.04787 [physics.ins-det] (cit. on p. 40).

[75] H. A. Chan and H. J. Paik, "Superconducting gravity gradiometer for sensitive gravity measurements. I. Theory", Phys. Rev. D **35**, 3551–3571 (1987) (cit. on p. 41).

[76] M. V. Moody, H. J. Paik, and E. R. Canavan, "Three-axis superconducting gravity gradiometer for sensitive gravity experiments", Review of Scientific Instruments **73**, 3957–3974 (2002) (cit. on p. 41).

[77] H. J. Paik, M. Vol Moody, and R. S. Norton, "SOGRO — Terrestrial full-tensor detector for mid-frequency gravitational waves", International Journal of Modern Physics D **29**, 1940001 (2020) (cit. on p. 41).

[78] D. W. Keith, C. R. Ekstrom, Q. A. Turchette, and D. E. Pritchard, "An interferometer for atoms", Phys. Rev. Lett. **66**, 2693–2696 (1991) (cit. on p. 41).

[79] M. Kasevich and S. Chu, "Measurement of the gravitational acceleration of an atom with a light-pulse atom interferometer", Applied Physics B **54**, 321–332 (1992) (cit. on p. 42).

[80] T. L. Gustavson, P. Bouyer, and M. A. Kasevich, "Precision Rotation Measurements with an Atom Interferometer Gyroscope", Phys. Rev. Lett. **78**, 2046–2049 (1997) (cit. on p. 42).

[81] M. J. Snadden, J. M. McGuirk, P. Bouyer, K. G. Haritos, and M. A. Kasevich, "Measurement of the Earth's Gravity Gradient with an Atom Interferometer-Based Gravity Gradiometer", Phys. Rev. Lett. **81**, 971–974 (1998) (cit. on p. 42).

[82] S. Dimopoulos, P. W. Graham, J. M. Hogan, M. A. Kasevich, and S. Rajendran, "Atomic gravitational wave interferometric sensor", Phys. Rev. D **78**, 122002 (2008) (cit. on p. 42).

[83] S. Kawamura et al., "The Japanese space gravitational wave antenna - DECIGO", Journal of Physics: Conference Series **122**, 012006 (2008) (cit. on p. 43).

[84] S. Kawamura et al., "Current status of space gravitational wave antenna DECIGO and B-DECIGO", Progress of Theoretical and Experimental Physics **2021**, 05A105 (2021) (cit. on p. 43).

[85] J. Harms et al., "Low-frequency terrestrial gravitational-wave detectors", Phys. Rev. D **88**, 122003 (2013) (cit. on p. 49).

[86] H. B. Callen and T. A. Welton, "Irreversibility and Generalized Noise", Phys. Rev. **83**, 34–40 (1951) (cit. on p. 51).

[87] Y. Levin, "Internal thermal noise in the LIGO test masses: A direct approach", Phys. Rev. D **57**, 659–663 (1998) (cit. on p. 53).

[88] G. M. Harry et al., "Thermal noise in interferometric gravitational wave detectors due to dielectric optical coatings", Classical and Quantum Gravity **19**, 897 (2002) (cit. on p. 53).

[89] H. J. Kimble, Y. Levin, A. B. Matsko, K. S. Thorne, and S. P. Vyatchanin, "Conversion of conventional gravitational-wave interferometers into quantum nondemolition interferometers by modifying their input and/or output optics", Phys. Rev. D **65**, 022002 (2001) (cit. on p. 53).

[90] T. Shimoda, N. Aritomi, A. Shoda, Y. Michimura, and M. Ando, "Seismic cross-coupling noise in torsion pendulums", Phys. Rev. D **97**, 104003 (2018) (cit. on pp. 55, 62).

[91] T. Shimoda and M. Ando, "Nonlinear vibration transfer in torsion pendulums", Classical and Quantum Gravity **36**, 125001 (2019) (cit. on p. 56).

[92] H. Ohta et al., "Neuromagnetic SQUID measurements in a helmet-type superconducting magnetic shield of BSCCO", IEEE Transactions on Applied Superconductivity **3**, 1953–1956 (1993) (cit. on p. 59).

[93] L. Weber and E. Gmelin, "Transport properties of silicon", Applied Physics A **53**, 136–140 (1991) (cit. on p. 59).

[94] A. Shoda et al., "Search for a stochastic gravitational-wave background using a pair of torsion-bar antennas", Phys. Rev. D **89**, 027101 (2014) (cit. on p. 60).

[95] 下田 智文, "ねじれ型重力波望遠鏡 TOBA のための地面振動雑音低減法の研究", https://granite.phys.s.u-tokyo.ac.jp/theses/shimoda_m.pdf, 修士論文 (東京大学, 2017) (cit. on pp. 61, 62, 70).

[96] K. Eda, A. Shoda, Y. Itoh, and M. Ando, "Improving parameter estimation accuracy with torsion-bar antennas", Phys. Rev. D **90**, 064039 (2014) (cit. on p. 61).

[97] Y. Kuwahara, A. Shoda, K. Eda, and M. Ando, "Search for a stochastic gravitational wave background at 1–5 Hz with a torsion-bar antenna", Phys. Rev. D **94**, 042003 (2016) (cit. on p. 61).

[98] A. Shoda, "Development of a High-Angular-Resolution Antenna for Low-Frequency Gravitational-Wave Observation", http://granite.phys.s.u-tokyo.ac.jp/shoda/Thesis_shoda.pdf, Ph.D. thesis (The University of Tokyo, 2014) (cit. on p. 61).

[99] S. Takano, "Cryogenic Monolithic Interferometer for Low-frequency Gravitational Wave Observation", https://granite.phys.s.u-tokyo.ac.jp/theses/takano_d.pdf, Ph.D. thesis (The University of Tokyo, 2024) (cit. on p. 69).

[100] T. Shimoda, Y. Miyazaki, Y. Enomoto, K. Nagano, and M. Ando, "Coherent angular signal amplification using an optical cavity", Appl. Opt. **61**, 3901–3911 (2022) (cit. on p. 69).

[101] 宮崎 祐樹, "ねじれ型重力波望遠鏡 TOBA のための高感度角度センサの開発", https://granite.phys.s.u-tokyo.ac.jp/theses/miyazaki_m.pdf, 修士論文 (東京大学, 2020) (cit. on p. 69).

[102] 大島 由佳, "重力波望遠鏡 TOBA のための結合光共振器を用いた角度信号増幅の実証", https://granite.phys.s.u-tokyo.ac.jp/theses/oshima_m.pdf, 修士論文 (東京大学, 2022) (cit. on p. 69).

[103] Y. Oshima, S. Takano, C. P. Ooi, Y. Michimura, and M. Ando, "Wavefront Sensing with a Coupled Cavity for Torsion-Bar Antenna", 10.5281/ZENODO.6917356 (2022) (cit. on p. 69).

[104] C. P. Ooi, "Mechanical Loss of Crystal Fibres for Torsion Pendulum Experiments", https://granite.phys.s.u-tokyo.ac.jp/theses/ooi_m.pdf, Master's thesis (The University of Tokyo, 2018) (cit. on p. 69).

[105] T. Shimoda, "Cryogenic Torsion Pendulum for Observing Low-frequency Gravity Gradient Fluctuation", https://granite.phys.s.u-tokyo.ac.jp/theses/shimoda_d.pdf, Ph.D. thesis (The University of Tokyo, 2019) (cit. on pp. 69–71, 73, 74, 110).

[106] 高野 哲, "ねじれ型重力波望遠鏡 TOBA のための能動防振系の開発", https://granite.phys.s.u-tokyo.ac.jp/theses/takano_m.pdf, 修士論文 (東京大学, 2019) (cit. on p. 69).

[107] F. Matichard and M. Evans, "Review: Tilt - Free Low - Noise Seismometry", Bulletin of the Seismological Society of America **105**, 497–510 (2015) (cit. on p. 69).

[108] 山元 一広, "TAMA300 の Suspension system 及び鏡の熱雑音の推定", https://granite.phys.s.u-tokyo.ac.jp/theses/yamamoto_m.pdf, 修士論文 (東京大学, 1996) (cit. on p. 74).

[109] J. Winterflood and D. G. Blair, "A long-period vertical vibration isolator for gravitational wave detection", Physics Letters A **243**, 1–6 (1998) (cit. on p. 88).

[110] A. Bertolini, G. Cella, R. DeSalvo, and V. Sannibale, "Seismic noise filters, vertical resonance frequency reduction with geometric anti-springs: a feasibility study", Nuclear Instruments and Methods in Physics Research Section A: Accelerators, Spectrometers, Detectors and Associated Equipment **435**, 475–483 (1999) (cit. on p. 88).

[111] G. Cella, R. DeSalvo, V. Sannibale, H. Tariq, N. Viboud, and A. Takamori, "Seismic attenuation performance of the first prototype of a geometric anti-spring filter", Nuclear Instruments and Methods in Physics Research Section A: Accelerators, Spectrometers, Detectors and Associated Equipment **487**, 652–660 (2002) (cit. on p. 88).

[112] G. Cella, V. Sannibale, R. DeSalvo, S. Márka, and A. Takamori, "Monolithic geometric anti-spring blades", Nuclear Instruments and Methods in Physics Research Section A: Accelerators, Spectrometers, Detectors and Associated Equipment **540**, 502–519 (2005) (cit. on p. 88).

[113] T. Akutsu et al., "Vibration isolation systems for the beam splitter and signal recycling mirrors of the KAGRA gravitational wave detector", Classical and Quantum Gravity **38**, 065011 (2021) (cit. on p. 89).

[114] Y. Aso, "Active Vibration Isolation for a Laser Interferometric Gravitational Wave Detector using a Suspension Point Interferometer", https://granite.phys.s.u-tokyo.ac.jp/theses/aso_d.pdf, Ph.D. thesis (The University of Tokyo, 2005) (cit. on pp. 89, 101, 102, 122).

[115] 正田 亜八香, "ねじれ型重力波検出器 TOBA の開発及び背景重力波探査", https://granite.phys.s.u-tokyo.ac.jp/theses/shoda_m.pdf, 修士論文 (東京大学, 2012) (cit. on p. 90).

[116] 有冨 尚紀, "ねじれ型重力波望遠鏡 TOBA のためのモノリシック干渉計の開発", https://granite.phys.s.u-tokyo.ac.jp/theses/aritomi_m.pdf, 修士論文 (東京大学, 2017) (cit. on p. 90).

[117] 中村 卓史, 三尾 典克, 大橋 正健, **重力波をとらえる: 存在の証明から検出へ** (京都大学学術出版会, 1998) (cit. on p. 96).

[118] R. O. R. Y. Thompson, "Coherence Significance Levels", Journal of Atmospheric Sciences **36**, 2020 –2021 (1979) (cit. on pp. 106, 109, 112).

Acknowledgments

I received invaluable support from many people. I would like to express my gratitude to each of them here.

First, I wish to extend my sincere gratitude to my supervisor, Professor Masaki Ando. He always gave me appropriate advice and new ideas whenever I asked questions in weekly meetings, TOBA design meetings, and midterm seminars. During practices for conference presentations, he patiently reviewed each slide and gave me detailed instruction. The calm, open atmosphere in Ando Lab for active discussions reflects his personality. I am also thankful to have been able to conduct my research in such a well-equipped experimental environment. I feel fortunate to have been able to join Ando Lab.

Our Assistant Professor Kentaro Komori has always been attentive to the progress of my experiments. He frequently visited the experimental room and offered me thoughtful advice. While keeping track of the experiments for all the students in Ando Lab, he also advanced research on KAGRA, SILVIA, optomechanical experiments, and Long SRC. His conference presentations were excellent, serving as a model for students. I greatly respect his diligent attitude and gentle character.

I am also deeply grateful to our former Assistant Professor, Yuta Michimura. He regularly provided me with advice on my experiments when I was in my master's course. He always reviewed and edited my papers and conference slides. His presentation slides and notes summarizing basic knowledge have been a great resource that I have referred to countless times. I admire his leadership in guiding research groups such as dark matter search.

I would like to thank my secondary supervisor for JSR Fellowship, Senior Professor Junji Yumoto. He regularly held individual meetings, listened to my concerns about research and job hunting, and encouraged me.

I am also thankful to the screening committee of my dissertation. Prof. Aya Bamba, the chair of the committee, guided me during my undergraduate experiments and she is one of the female researchers I respect the most. She provided meticulous advice on revising my dissertation, and I feel fortunate to have had her as the chair. Prof. Yoichi Aso offered invaluable advice during the development of the GAS filter. His profound understanding of gravitational wave detectors enabled him to provide many insightful

comments on my dissertation. Prof. Hideyuki Tagoshi greatly encouraged me to pursue the field of gravitational waves during the Spring School at the Institute for Cosmic Ray Research in my undergraduate years. He provided valuable feedback on my work from the perspective of gravitational wave theory. Professors Masayuki Nakahata and Takanori Yoshikoshi contributed sharp and insightful feedback from the perspectives of their respective fields.

My excellent colleagues in Ando Lab are always exciting me.

Ryosuke Sugimoto has a broad range of knowledge from his experience with KAGRA and JAXA/ISAS, and he has generously shared them with me.

I really appreciate Hiroki Fujimoto. I can easily consult with him, and we often chat not only about research but also about many other topics. I admire his dedication to fully understand things, his steady approach to solving problems in experiments, and his excellent theoretical calculation skills. I am so lucky to have such a talented peer who has taught a lot and inspired me.

Masaya Ono has left many contributions to Ando Lab, including work on pendulums and electronic circuits, which have greatly helped my research. Since his first year of doctoral course, he has been studying abroad at MIT and Caltech, and I am always surprised by his motivation and drive.

Hinata Takidera is making great progress on the DANCE project. I am thankful to him for carefully reading my paper and finding calculation errors. He also kindly read through my thesis and gave me many helpful comments.

I am glad that Tatsuya Sugioka is interested in TOBA and is taking over my experiment. I eagerly await the results of his thesis.

I was very happy when Yuki Yamaguchi enrolled because the number of female students increased. I look forward to her progress on the experiment.

Additionally, I am deeply grateful to Ando Lab alumni.

Haoyu Wang is a specialist in simulations using FINESSE software, and he taught me how to use it.

Perry William Fox Forsyth provided many valuable insights during the TOBA design meetings, based on his experience with the TorPeDO experiment.

Takuya Kawasaki answered my questions about experimental techniques. His consistent progress in writing papers is inspiring, and I have referred to his master's thesis many times.

Ching Pin Ooi often proofread the English in my papers. As a native English speaker fluent in Japanese, he explained English nuances to me clearly in Japanese, which was very helpful.

Satoru Takano always supported juniors and spent long hours discussing questions with me and offering advice. He taught me the importance of identifying the cause of failures quantitatively. I am thankful for his kindness. The reason I chose TOBA as my research topic is that I heard about its interesting aspects from him and wanted to continue his work. If he hadn't been my senior, I might have chosen a different topic.

Mengdi Cao was a visiting student from China. Since we had been communicating via email before she came to Japan, I was delighted to finally meet her. I am grateful to

have worked with her on the TOBA project.

Koji Nagano is a DANCE collaborator, and he provided advice on my conference slides and papers. In addition, he held weekly foundational lectures during my second-year master's course, where I learned the basics of optical cavities and feedback control. I am grateful for his patience with my less-than-clear questions and respect his willingness to share his extensive knowledge with juniors.

Tomofumi Shimoda and Yuki Miyazaki conducted research on TOBA. The topics of my master's and doctoral theses involve improvements to their setup, and my work would not have been possible without their contributions. Even after their graduation, they have kindly responded to my questions via email, and I appreciate for their help.

I also thank the collaborators of DANCE project, which is my first research topic in Ando Lab. I had a great time working on DANCE with Taihei Watanabe in my undergraduate course, and I decided to join Ando Lab. Jun'ya Kume and Soichiro Morisaki provided data analysis code and thoroughly explained the principles and usage. Ippei Obata, Tomohiro Fujita, and Atsushi Nishizawa gave me a lot of advice on my presentation slides and papers.

I appreciate Togo Shimozawa and Shigemi Otsuka for manufacturing the mechanical parts. I also thank to many companies such as Ono-Denki Seisakusho and SIGMAKOKI. My sincere thanks extend to all company I could not mention here.

I extend my thanks to Mayuko Niwata and Kyoko Tanaka from the department office and to Mai Yamashita, Natsuko Chino, and Chiharu Yoshioka from CURIE office for the office work. Their support allowed me to conduct my research smoothly.

I have been financially supported by Grant-in-Aid for JSPS Fellows No. JP22J21087 and by JSR Fellowship, the University of Tokyo. The work about TOBA was supported by JSPS KAKENHI Grants Number JP16H03972, JP24244031, JP18684005 and JP22H01246. This work was also supported by MEXT Quantum Leap Flagship Program (MEXT Q-LEAP) Grant Number JPMXS0118070351.

I would like to extend my heartfelt gratitude to my friends and family. In particular, I appreciate my husband-to-be for studying together in our class at Komaba Campus and in the Department of Physics. I hope we will always continue to support each other. Finally, I want to show my deepest appreciation to my mother and father for their support and understanding me better than anyone else. I respect them both as individuals and as researchers. They are my lifelong role models, and I strive to catch up with and surpass them.